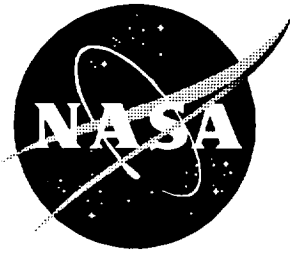NASA Contractor Report 4710

Euler Technology Assessment for Preliminary Aircraft Design—Compressibility Predictions by Employing the Cartesian Unstructured Grid SPLITFLOW Code

Dennis B. Finley and Steve L. Karman, Jr.

March 1996

Euler Technology Assessment for Preliminary Aircraft Design—Compressibility Predictions by Employing the Cartesian Unstructured Grid SPLITFLOW Code

Dennis B. Finley and Steve L. Karman, Jr.
Lockheed Martin Tactical Aircraft Systems • Forth Worth, Texas

Table of Contents

List of Tables

List of Figures

Euler Technology Assessment for Preliminary Aircraft Design - Compressibility Predictions by Employing the Cartesian Unstructured Grid SPLITFLOW Code

Dennis B. Finley
Steve L. Karman, Jr.
Lockheed Martin Tactical Aircraft Systems

Summary

This report documents results from the second phase of the Euler Technology Assessment program. The objective of this phase was to evaluate the ability of Euler computational-fluid dynamics codes to predict compressible flow effects over a generic fighter wind tunnel model. This portion of the study was conducted by Lockheed Martin Tactical Aircraft Systems, using an in-house Cartesian-grid code called SPLITFLOW (Ref. 1). The Cartesian grid technique provides ease of volume grid generation and a reduction in the required number of cells compared to other grid schemes. SPLITFLOW also includes grid adaption of the volume grid during the solution to resolve high-gradient regions. The SPLITFLOW code predictions of compressibility effects on pressures and integrated forces are shown to be suitable for preliminary design, including predictions of sideslip effects and the effects of geometry variations at low and high angles-of-attack. The transonic pressure prediction capabilities of SPLITFLOW are shown to be improved over subsonic comparisons. The time required to generate the results from initial surface data is on the order of several hours, including grid generation, which is compatible with the needs of the design environment.

1. Introduction

This study is a follow-on to a research program for Euler code predictions developed in 1994 (Ref. 2). The current study concentrates on compressibility effects on Euler predictions. The onset of transonic flow induces fundamental changes in the character of Euler predictions, including substantial regions of supersonic flow and shock formation (Ref. 3). The resultant generation of entropy within the Euler solution, which has been shown to induce large-scale vortical structures (Ref. 4), provides a distinct difference from low-Mach number predictions in which vortical effects are created only through numerical dissipation. Also, the substantial overprediction of peak suction pressure coefficient in subsonic Euler predictions tends to be diminished at transonic conditions (Ref. 3). The current program provides a systematic comparison of Euler prediction capability at subsonic and transonic freestream conditions for a configuration which generates significant vortical flow. The configuration is the Modular Transonic Vortex Interaction (MTVI) test model, which has been extensively tested at NASA Langley Research Center (Ref. 5). The MTVI configuration has been utilized for previous studies of the predictive capability of Euler solvers on forebody flows (Ref. 6) and for initial

8

wing-body-tail Euler code investigation of this study (Ref. 2). Features of the test vehicle include sharp leading edges and a chine forebody. Test data are available for the MTVI configuration with two vertical tail arrangements. Angle-of-attack and sideslip conditions are used for comparison with code predictions.

2. General Algorithm Attributes

Code formulation

SPLITFLOW is a finite-volume Euler/Navier-Stokes code which utilizes a hybrid grid system. A Cartesian grid, composed of cubical cells, is used to discretize the computational domain and is efficient for computing inviscid solutions about extremely complex geometries. A prismatic grid may be used near solid surfaces for viscous analyses to allow accurate resolution of the boundary layer region. The code uses upwind flux difference splitting for the inviscid fluxes, with flux limiters available to reduce oscillations near shocks. The Cartesian grid method produces rapid subdivision of root cells, and a fixed cell aspect ratio for ease of reconstruction of face information. Solution grid adaption is included within SPLITFLOW, offering several user-selectable adaption functions. The code also provides extremely fast user setup times.

Surface Representation

The surface geometry is input as a triangulated surface mesh. This mesh is provided by the engineering CAD package used to define the configuration. By interfacing with the CAD package directly, conversion of geometry to CFD surface definitions is eliminated. The surface in the CAD file is defined as a list of X, Y, and Z coordinates and a connectivity in the form of three node numbers. The node numbers correspond to the indices of the forming points of each triangle making up the surface. The geometry facets are oriented such that the surface normals point into the computational domain. Subsets of the facets can be grouped together and associated with a particular boundary condition type such as no-slip, symmetry, characteristic slip wall, etc.

Numerical Formulation

The governing equations are the Reynold's averaged, compressible Navier-Stokes equations. The discrete-integral form of the equations for an arbitrarily-shaped cell is:

$$\frac{\Omega}{\Delta t}\Delta Q + \sum_{m}^{ns} (F_i - F_v)_m \bullet (n_m \sigma_m) = 0$$

where ns is the number of sides of the cell (to accommodate boundary cut cells). The inviscid flux vector is given by F_i. The viscous flux vector is F_v. The conservative variables are repre-

9

sented by the vector Q. The cell volume is represented by Ω and Δt is the time step. The outward-pointing unit normal vector for face m is n_m and the surface area is given by σ_m.

A steady-state solution to the governing equations is obtained by using an implicit time-marching scheme. Upwind fluxes are used for the inviscid terms, and central-differences are used for the viscous terms. A consistent set of flux functions are used in the solution procedure on both the Cartesian grid and the prismatic grid. A point-wise implicit time-integration scheme with sub-iterations is used to advance the solution. The numerical form of the implicit scheme is:

$$\left[\frac{\Omega}{\Delta t}I + \sum_{m}^{ns}\left(\frac{\delta F}{\delta Q_c}\right)_m \right](\Delta Q^s{}_c) = \left(-\left[\sum_{m}^{ns}\left(\frac{\delta F}{\delta Q_i}\right)_m\right]\right)\Delta (Q_i)^{s-1} - (Res)^{n-1}$$

The current cell is given by c. The neighboring cells are given by i. Res is the residual vector computed as the sum of the fluxes over the cell. I is the identity matrix. The sub-iterations are indicated by s.

The flux Jacobians are first order inviscid Jacobians consistent with Roe's scheme plus face normal viscous Jacobians. The equations requires a block inversion of a 5X5 matrix for each cell. The inverted matrix is computed during the first sub-iteration and stored for use in subsequent sub-iterations. Typically, 10 to 20 sub-iterations are used to converge the implicit equation at each time level.

The Courant-Friedrich-Lewy (CFL) number is automatically adjusted by the code, depending on the sub-iteration convergence characteristics. CFL numbers on the order of 5 or more are possible for most inviscid problems. Viscous problems sometimes require smaller values of the CFL number for stability.

The inviscid fluxes are computed using Roe's approximate Riemann solver. Primitive variables are extrapolated to the cell faces using a second-order accurate difference stencil. A superbee limiter (Ref. 7) is used to reduce the order of accuracy near discontinuities and prevent overshoots. This limiter features a compression parameter that reduces the dissipative nature of the limiter away from the discontinuity. The use of a less dissipative limiter improves the resolution of the upper-surface 'vortices' in test cases, and improved the agreement between the computed and experimental surface pressures. The entropy fix of Harten (Ref. 8) is used to prevent non-physical expansion shocks.

A third-order accurate scheme was implemented, during the viscous analysis that is discussed in Section 5. The limiter used for the viscous run was a minmod limiter with a variable compression parameter. The third-order scheme produces results which are, as a minimum, as accurate as the second-order scheme with the superbee limiter. The third-order

10

scheme was used for all of the viscous analyses performed in this study.

Grid Generation

The initial Cartesian grid is generated based on the resolution of the surface triangulation of the boundary facet file. Generally, the surface of the vehicle of interest will contain a much denser mesh of triangular facets than the outer boundary face regions. The root cell encompassing the entire geometry is termed grid level 1, and is subdivided in the X, Y, and Z directions resulting in eight offspring cells at grid level 2. Each offspring cell is recursively subdivided based on a cell length-scale criterion. The length scale of each cell is compared with the length scale of all the geometry facets that are contained within the cell or are touched by the cell. The cell length scale is defined as the length of the sides of the cell. The length scale of the geometry facet is usually defined as the average length of the three sides of the facet. If a particular cell length scale is larger than the facet length scale multiplied by a user-specified scale factor, the cell is subdivided. This process continues down each branch of the octree data structure until all cells without offspring satisfy the length scale criterion.

For viscous analysis the prismatic grid generator is employed (Ref. 9) to build a grid suitable for resolving boundary layers. The thickness of the prismatic grid is dictated by an estimate of the boundary layer thickness. Flowfield features outside the prismatic grid will be resolved using grid adaption of the Cartesian grid. SPLITFLOW will treat the outer layer of the prismatic grid as another triangulated surface when constructing the Cartesian grid.

During the subdivision process, grid smoothing constraints are enforced. No cell can have more than four neighbors on any side. This is equivalent to limiting the differences in grid levels between adjacent cells to one. This constraint is enforced so that the octree data structure can be used to rapidly determine the neighbor information of the cells on all grid levels. Any refinement resulting from this constraint quickly propagates through the grid. The resulting grid has fine resolution cells near bodies, and coarse resolution cells in the far-field.

Cartesian grid generation may result in cells that are divided into multiple distinct volumes near thin sharp-edged regions. These cells are invalid since storage exists for only one set of flowfield variables. SPLITFLOW uses an area summing approach to sum the X, Y, and Z area components of the boundary facets in each cell that lies along the boundary. If any of the area components sum to zero while large negative and positive summations occur, then the cell may be invalid. Invalid cells are marked for additional cell subdivision and the grid validity is rechecked. The process is repeated until all invalid cells are eliminated or the minimum cell size is reached which prohibits further cell subdivision.

An octree data-structure is used to store information for each Cartesian cell during the recursive grid generation process. A subdivided cell produces eight new offspring cells. The parent is retained in the grid after the subdivision. The information stored for each cell consists of the global index of the parent cell, the global indices of the eight children that may exist

and the grid level of the cell. The grid level refers to the number of times the root cell has been recursively subdivided to create this particular child. Since the position of each offspring cell (in relation to its parent) is predetermined in the subdivision process (due to the Cartesian topology) the neighboring cell indices can quickly be determined. In addition, many of the search procedures are made efficient using the octree data structure.

Grid Adaption

During the solution process, additional grid refinement and coarsening occurs based on the local flowfield gradients. SPLITFLOW offers several grid adaption functions such as static pressure or Mach number. These functions are selected by the user, and are used to refine or derefine the grid. The gradient of each chosen adaption function is computed across the cell and multiplied by a cell length scale. This cell length scale is adjusted by an exponent based on a user selected term. This gives some control for supersonic flows in which the adaption function gradient across shocks is so high that the cells near the shock tend to dominate the adaption function statistics. Properly selecting these exponents ensure the refinement procedure achieves true grid convergence in the numerical sense. A statistical approach is used for assessing the need for grid adaption in each cell. This approach dramatically reduces the requirement for user decisions about grid adaption. The user simply defines the thresholds of the values on the adaption function at which cells will be marked for refinement or derefinement. Refinement occurs automatically for cells which exceed the maximum threshold. Cells which fall below the minimum threshold of the adaption function are marked for derefinement. Derefinement occurs for cells in which all 8 children of a common parent have been marked.

Deleted cells are removed from the grid causing the parent cell to become the active cell. Cells marked for refinement are subdivided. Grid smoothing is employed during the adaption process to assure that only one level changes between adjacent cells and that a smooth mesh is generated.

As the solution proceeds, refinement events occur periodically, typically every 50 iterations. Cells are added or deleted, and the residual initially spikes then resumes its downward trend. For the MTVI cases, generally 2-3 orders-of-magnitude of convergence of the L2 norm of the residual were achieved.

User Work-load and SPLITFLOW Domain Definition

The creation of a SPLITFLOW grid requires only definition of the surface mesh. The user determines the level of surface resolution using the CAD system, creating a triangulated point set that is clustered to areas of geometric complexity. The other boundaries of the domain such as a symmetry plane are also constructed by using the CAD system. All of the boundaries are combined in one boundary file, where each boundary condition type is specified. This boundary file is the input to SPLITFLOW, along with a namelist file containing

flow conditions, grid adaption parameters, surface integration terms and requested print data such as surface pressures. The time required to set up a problem is generally 20 to 40 minutes.

3. Grid Convergence for Euler Technology Assessment

Specific results of the surface and volume grid generation for the Euler Technology Assessment study are shown in this section. The configuration used for the computations was the NASA-Langley Modular Transonic Vortex Interaction (MTVI) model (Ref. 5). The MTVI configuration features a 60-degree clipped delta wing and a large fuselage which extends ahead of the wing. The baseline centerline tail geometry is shown in Figure 3.1. A significant feature of this configuration is the sharp leading and trailing edges on the wing, fuselage and tail. This promotes flow separation and roll-up into upper-surface vortices, and reduces the sensitivity of test and predicted results to Reynolds number effects associated with the onset of vortical flow. The geometry variation used in the study was the position of the vertical tails (centerline vs. wing-mounted). The fuselage geometry incorporated a 30-degree chine, and the wing leading-edge flap was un-deflected. A wind tunnel sting representation was added to the base of the fuselage, consisting of a reduced-area cross-section extending approximately one body length aft of the body. A tapered region closed the gap between the end of the model and the beginning of the sting. The number of surface facets for the triangulated surface grid of the centerline tail configuration was 36,452.

The twin-tail version of the MTVI configuration is shown in Figure 3.2. The fuselage and wing geometry are unchanged from the centerline tail configuration. The overall triangulated surface grid of the twin tail configuration had 36,594 facets.

Preparation of the faceted grids for the vehicle, and outer boundaries, was conducted on a Silicon Graphics IRIS Indigo Extreme workstation. The construction of the Cartesian grids within SPLITFLOW begins with the boundary face file provided by the user. The maximum cell size for volume grid cells near the outer boundaries was selected to be approximately 12 inches. A target size for the smallest cells is selected by the user. The smallest element in each MTVI facet file had edges of approximately 0.000025 inches. The maximum number of grid levels possible using these parameters is 20. In general, this level of near-wall resolution has been adequate for Euler calculations. Figure 3.3 shows an example of the final adapted grid for one of the symmetric centerline tail solutions. The off-body grid adaption to flowfield gradients is indicated.

Solution timing

An example of a symmetric (no sideslip) solution sequence is used to show the solution characteristics. The convergence of forces is shown in Figure 3.4, and the moments are shown in Figure 3.5. The forces tend to converge in 400 steps. The initial Cartesian grid generation process required about 30 to 40 minutes of CPU time, and the subsequent grid refinement and

13

adaption during the course of the solution required an additional 20 to 40 minutes. These results depend on the number of refinement sweeps requested by the user. Generally the grid generation and refinement times add a small amount of overhead to the solution time (about 5 percent). The overall solution time for symmetric runs averaged 3 hours on the C-90. The grid generation took about 700 seconds, and the adaption and refinement was 500 seconds. The cell count, Figure 3.6, shows the developing number of cells which are added during the solution. Three lines are shown on the plot. The top line is the total number of cells. The middle line shows the number of 'active cells', or cells within the domain. The lower line indicates the number of active cells without children. In general, around 500K active cells without children were required for the final converged solutions for these cases, with force and moment as the measure of convergence. The memory requirements for the symmetric runs were 113 Cray megawords.

The solution sequence for a sideslip case is shown in Figure 3.7 - Figure 3.9. These solutions required 800-1100 steps, and approximately 14-18 C-90 cpu hours. From 800K to 1100K active cells without children were used for the asymmetric cases. The memory requirements for the sideslip runs were 192 Cray megawords.

4. Computational Results and Comparison with Test Data

The MTVI configurations used in this study were run in various settings of Mach number, angle-of-attack and angle-of-sideslip. The run matrix for this study is shown in Table 4.1. The matrix allows comparison of subsonic and transonic flow effects at angles-of-attack from 10 to 30 degrees, and sideslip angles to 7 degrees. The case number in the first column provides a convenient indexing of the configuration discussion in the next subsections.

Compressibility Effects for Centerline Tail vs. Angle-of-Attack, Case 1 and 2

The stability axis force results for Cases 1 and 2 are presented in Figure 4.1 to compare the predictive capability of the Euler code at subsonic versus transonic conditions. The pitching moment versus lift coefficient appears to capture the slope of the data for lift coefficients of less that 1.2 and angles-of-attack less than 20 degrees, with an over-prediction of the nose-down pitching moment. A zero-lift increment of 0.0200 has been extracted from experimental data and added to the predicted drag to account for estimated skin friction. Since the configuration is uncambered, this increment was also added to the axial force. The lift and nose-down pitching moment for the centerline tail are over-predicted at Mach 0.4 (Figure 4.1), since the static suction pressures on the aft portion of the wing are over-predicted (to be shown in following figures). At the highest predicted angle-of-attack, 30 degrees, the predicted lift remains high, and the pitching moment indicates a stable trend which is contradicted in the test results. The force and moment predictions show much better agreement with the experimental data at Mach 0.85. The pitching moment tends to have an unstable break at the highest angle-of-attack, similar in character to the test data. The drag polar at the

14

high angles-of-attack is better matched at the transonic condition (because the lift coefficient is also better predicted).

The body axis results are shown in Figure 4.2. The axial force (with the skin friction offset included) is over-predicted. However, the slope of axial force vs. angle-of-attack is reasonably well-predicted for both Mach numbers. This indicates that the Euler results capture the trend of a loss in effective 'thrust' as the vehicle moves from subsonic speed to transonic speed. The nose-down pitching moment at high angles-of-attack, and the stability of the configuration, were over-predicted in the Mach 0.4 results. At a Mach number of 0.85, the pitching moment is close to the test data, except for a sudden nose-up shift at 30 degrees angle-of-attack that corresponds to a lift loss, and loss in suction pressure at the aft part of the wing (to be shown in a following figure).

Pressure data for all of the angles-of-attack evaluated in the study are shown in Figure 4.3 to Figure 4.7. These data are shown for the centerline tail vehicle at subsonic conditions (Case 1) and transonic conditions (Case 2). The test and predicted pressure values for the six fuselage stations where data were measured are shown in the figures. The test data and predictions for Mach 0.4 are shown with closed symbols and solid lines, and the Mach 0.85 data are shown with open symbols and dashed lines. The three fuselage stations where forebody pressures were measured are shown in the three plots in the left-hand column (corresponding to model FS 6.1 inch, 10.4 inch, 14.5 inch). The progressive increase in peak suction pressure on the forebody with angle-of-attack is seen to be predicted by the code, although the peak value is shifted slightly outboard from the test results. This would be expected from previous studies (Ref. 6 and Ref. 10) where the inviscid predictions typically overpredict the suction peak at subsonic conditions, as well as produce an outboard shift of the suction peak due to the lack of simulating the secondary separation. In the current results, the subsonic overprediction of peak suction is not as apparent on the forebody as it is on the wing. The predictions indicate the outboard shift in the peak, typical of Euler results. The forebody pressure predictions at Mach 0.85 correctly show the transonic effect on static pressure, namely a reduction in upper surface suction on the forebody, as Mach number increases. The theoretical critical pressure coefficient for these conditions is -3.66 for the Mach 0.4 freestream case, and -0.30 for the Mach 0.85 case. Since the test pressure coefficients exceed the critical values only for the Mach 0.85 case, supersonic flow would be expected for the Mach 0.85 condition.

The three wing stations where pressures were measured (FS 19.06, 23.56, 28.06) are shown in the three plots on the right-hand column of the figures. At Mach 0.4 the peak vortex suction on the wing tends to be highly over-predicted, especially for the aft wing stations and at higher angles-of-attack. At 30 degrees (Figure 4.7), the maximum predicted value of suction pressure at Station 5 (outside the scale of the plot) is -7.5. This overexpansion effect is seen in other research studies (Ref. 3), as is the lack of the secondary vortex peak in the Euler predic-

15

tion. This overexpansion is much reduced at Mach 0.85, which is also consistent with other research (Ref. 3). Conceptually the reduction is explained by the large reduction in vacuum Cp from subsonic conditions to Mach 0.85 freestream conditions. The vacuum pressure is reduced from -8.93 to -1.98. The transonic comparison shows that SPLITFLOW predicts the surface pressure distribution quite adequately for most of the angle of attack conditions.

The over-prediction of lift and nose-down moment at higher angles-of-attack for the Mach 0.4 condition (Figure 4.1) correlate with the over-predicted suction from the aft portion of the wing. Grid refinement during the solution sequence resolves the high rotational gradients in the flow. The Euler prediction may therefore not emulate the viscous losses in the test data. It would not be expected to, as stated earlier. SPLITFLOW has a relatively low level of numerical dissipation, and grid refinement may reduce the dissipative nature of the solution still further. This is a desirable result for an Euler solver, and at subsonic conditions the use of Euler results is predicated on understanding the limitations of the inviscid equations.

The wing pressure comparisons at Mach 0.85 are also seen in Figure 4.3 to Figure 4.7. At transonic conditions, the physical reduction in allowable suction, as emulated in the code, reduces the discrepancy in peak suction dramatically. In almost every case the code predicts the transonic pressure distribution quite closely. The only disagreement is at 25 degrees angle-of-attack at the last wing station. Here the code predicts the shape of the pressure distribution. The degree of agreement with the transonic results reinforces the improvements in the force data comparisons at transonic conditions. It can be concluded that at transonic conditions, the over-expansion characteristics of low-numerical-dissipation codes such as SPLIT-FLOW are reduced, and accurate predictions of surface pressures can result.

Repeat test data is shown in Figure 4.5 at 20 degrees angle-of-attack. This indicates the measure of repeatability in the test pressure data. The pressures are very repeatable, with agreement within 2% for the test data for both Mach numbers.

The visualization of flow field characteristics at 30 degrees angle-of-attack are shown in Figure 4.8 and Figure 4.9 for the two Mach numbers. The visualization of the pressure coefficient is seen in Figure 4.8 at the six wing stations for which surface pressure data were taken. The grey scale on the left indicates local Cp values. An overlay of the volume grid shows the grid adaption to flowfield gradients. Comparing the effect of increased Mach number, the loss in suction Cp within the vortex core at a Mach number of 0.85 can be seen as a reduction in the dark core region, and a corresponding reduction in amount of grid adaption in the core.

The visualization of the local Mach number is shown in Figure 4.9. The grey scale indicates local Mach number. The six fuselage stations on the model are again shown as cut planes, along with the adapted grid. For the selected local Mach number range, the Mach 0.85 flow shows a much larger zone at each cutting plane. Also, the region encompassed by the rather light shading (locally supersonic) is apparent at the Mach 0.85 cuts. The predicted pressure

16

distributions shown in Figures 4.3 to 4.7 indicated that the critical pressure coefficient was exceeded on the surface for the Mach 0.85 condition. Detailed examination of the off-body flowfield results (not shown) indicate that the centerline tail configuration has some supersonic flow within the vortex core even at the Mach 0.4 condition, and a sizeable amount of locally supersonic flow at Mach 0.85. This is consistent with the Euler formulation.

<u>Compressibility Effects for Twin Tail vs. Angle-of-Attack, Cases 3 and 4</u>

The force and moment predictions capture the trends of the stability-axis test data at both subsonic and transonic conditions for the twin-tail configuration as seen in Figure 4.10. Referring to the lift versus pitching moment curve, the severe jog in this curve at both Mach numbers is somewhat over-predicted by the code at subsonic conditions, but is well predicted at Mach 0.85. The Euler code provides the nonlinear trends of the tail configuration change.

In the integrated body-axis data (Figure 4.11), from 12.5 degrees to 17.5 degrees angle-of-attack a 'flat' region appears in the normal force combined with a severe nose-up pitching moment. These effects (that result in the severe nonlinearities in the moment vs. lift plot of Figure 4.10) are generally predicted by the code, aside from some overprediction of the subsonic nonlinearities.

As was seen for the centerline tail data (Figure 4.2), the predicted axial force for the twin tail captures the trend of the test data at both Mach numbers. The Euler prediction picks up the general nature of the axial force characteristics for both configurations, as well as the effect of increasing Mach number.

Pressure data for the twin tail configuration at all angles-of-attack evaluated in the study are shown in Figure 4.12 to Figure 4.18 to illustrate the comparisons at both Mach numbers. The forebody results appear similar to the comparisons for the centerline tail. The forebody pressures are somewhat underpredicted by the code at low angle-of-attack (10 and 15 degrees) but are over-predicted at higher angles as would be expected, with some outward shift of the peak. At Mach 0.85, the peak values of pressure are predicted well. The SPLITFLOW Euler predictions of the wing pressures are very representative of the test results. The predicted subsonic suction peak is suppressed by the presence of the vertical tail (at a span station of 4.5 inches) and the overall pressure distribution for subsonic conditions is representative of the test data. At transonic speed, the predicted pressures are very close to the test results. In the region of the outboard wing panel, outside of the vertical tails, the degree of agreement is extremely good, considering the possibility of large-scale separated zones in this region.

The presence of the vertical tail on the outer wing tends to cause the predicted wing pressure peak to interact with the forebody suction peak as angle-of-attack increases. This causes a loss in lift and the nose-up moment that was apparent in the integrated results. These effects are predicted by the code as a loss in wing suction peak pressure at the two aft wing stations (FS 23.56 and 28.06) as seen in Figure 4.13 to Figure 4.16 for angles-of-attack from 12.5 to 20

17

degrees. The effect is apparent for the freestream Mach number of 0.4. A visualization of the pressure data for four angles-of-attack, Figure 4.19, shows the effect of the tail interaction with the forebody and wing vortices. The predicted rotational flow in the tail region tends to merge in a zone inboard of the tails. This change in character of the predicted flowfield can be associated with the change in surface pressure and force characteristics in this angle-of-attack region.

Compressibility Effects in Sideslip for Centerline Tail Configuration, Cases 5 and 6

The yawing moment, rolling moment and side force for the centerline tail sideslip cases are shown in Figure 4.20 for the 15-degree angle-of-attack and two Mach numbers. These cases required on the order of 900K to 1.1M cells. The results at both Mach numbers show good general prediction of the trends of the side force and moments. The test data show negative side force with positive sideslip (as expected) and stable yawing moments.

Pressure data at sideslip angles of 2 degrees and 7 degrees are shown in Figure 4.21 and Figure 4.22. Repeatability of the test pressures at the sideslip condition is seen in Figure 4.22. The pressure data is repeatable to within 2%. At Mach 0.4, the SPLITFLOW prediction is below the peak suction on the forebody. The grid refinement during the run was concentrated on the wing and the resolution of the forebody may not have been sufficient to identify the strength of the vortex. The wing peak suction is over-predicted, as expected for an inviscid analysis. The trends of the Mach 0.85 prediction are similar, but the peak suctions are much closer to the test data.

The force and moment results for the centerline tail configuration at an angle-of-attack of 25 degrees are shown in Figure 4.23. The SPLITFLOW results predict the trends in the test data from subsonic to transonic conditions, including the large change in side force. The yawing moment is over-predicted by the code. A small nonlinear bend in the side force and yawing moment at Mach 0.85, above +/- 4 degrees is predicted. The nonlinearities in the rolling moment are not predicted at the Mach 0.4 condition, but are predicted at Mach 0.85.

The over-prediction of rolling moment at Mach 0.4 may be due to the over-prediction of peak suction on the windward wing as seen in Figure 4.24 and Figure 4.25, for sideslip of 2 degrees and 7 degrees. The Mach 0.85 wing pressures are much better predicted by SPLITFLOW at both 2 degrees and 7 degrees of sideslip. Closer prediction of wing peak suction at Mach 0.85 may result in the observed better agreement in the rolling moment prediction.

To investigate the side force and yawing moment at Mach 0.4, visualization of the configuration for the 7 degree sideslip condition is shown in Figure 4.26 as the surface pressure coefficient multiplied by the Y component of the inward pointing unit normal. Large differences between the surface shading from one side to the other indicate large contributions to side force. The light shaded region on the windward forebody is much larger than the dark shaded region on the leeward forebody, resulting in a net negative side force. The centerline

18

tail appears to contribute little to the predicted side force. It can be inferred from the contours that the forebody is producing the majority of the predicted yawing moment at these conditions.

Compressibility Effects in Sideslip for Twin Tail Configuration, Cases 7 and 8

The yawing moment, rolling moment and side force for the twin tail sideslip cases are shown in Figure 4.27. The agreement is much better for the twin tail configuration at both Mach numbers. The side force is positive for the configuration at small sideslip angles, and this is predicted. The yawing moment is near neutral to slightly stable, and this is also predicted. The prediction provides good agreement up to +/- 4 degrees and predicts the nonlinearities at higher sideslip at Mach 0.85.

Pressure data at sideslip angles of 2 degrees and 7 degrees are shown in Figure 4.28 and Figure 4.29. The forebody suction Cp on the windward side is somewhat over-predicted at Mach 0.4 from inviscid analysis, but is better predicted at Mach 0.85. The Cp distribution over the wing outboard of the twin tail is very peaky at the subsonic condition, as expected, but is well-predicted at Mach 0.85. The compressibility effect is well predicted on the upper surfaces of the forebody and wing, as well as the lower surface of the forebody.

The surface pressure coefficient multiplied by the Y component of the inward pointing unit normal for Mach 0.4 is shown in Figure 4.30. The results indicate that the forebody is again producing substantial side force, but the pressures on the twin tails produce a compensating force. The yawing moment comparison in Figure 4.27 indicates that the twin tail vehicle has a reduced level of yawing moment, and that SPLITFLOW is predicting the level accurately.

Centerline Tail vs. Twin Tail

Flow visualization of the local Mach number at a span station of 3.5 inches is shown in Figure 4.31 through Figure 4.33 for angles-of-attack of 20, 25 and 30 degrees for the Mach 0.85 cases. This is a position inboard of the vertical tails for the twin tail configuration. These results show the effect of the twin tail in reducing the amount of flow acceleration.

It was found that the most effective way to view the data was by using local Mach number. The vehicle is shown as a grey shaded surface in the figures and the Mach contours are shown as black lines in order to see the airplane fuselage behind the data plane. This was deemed to be more informative than a solid plane of data with only a stub wing appearing. The data indicates that the centerline tail vehicle has a shock at about 80 percent chord, that intensifies from 20 to 25 degree cases, followed by a severe wake flow that appears at 30 degrees. The shock moves forward from 25 to 30 degree cases for the centerline tail configuration. The twin tail solution shows a minimal shock at an angle-of-attack of 20, a strong shock ahead of the vertical tail position at an angle-of-attack of 25, and a similar disorganized wake behind the shock at an angle-of-attack of 30. The shock on the twin tail vehicle does not

19

move from 25 to 30 degrees angle-of-attack.

The local CP contours are shown for the Mach 0.85 case at an angle-of-attack of 25 degrees in Figure 4.34. The contours look similar to the Mach contours. The crossflow Mach number is shown in constant fuselage station cuts in Figure 4.35. This shows the position of the vortex. The location of the shocks are indicated in the figure. A large expansion around the leading edge of the wing is also evident. As indicated earlier, the surface pressures at this condition exceed the critical Cp, providing a possibility of locally supersonic flow.

The comparisons of predicted and test pressure levels at six fuselage stations are shown in Figure 4.36 to Figure 4.38 for the sideslip angles of 2, 4, and 7 degrees and angle-of-attack of 25 degrees at a Mach number of 0.4. SPLITFLOW predicts small variations in forebody pressure levels for each case, particularly at low sideslip angles, and this is also indicated in the test data. This indicates the tail position has some influence on the forebody pressure data. At a sideslip of seven degrees, both the configurations were predicted to have more suction on the windward side than was evident in the test data. Overall the code predicted incremental effects due to different tail configurations in sideslip.

The prediction of pressure on the wing in Figure 4.36 to Figure 4.38 is much closer on the leeward side than the windward side for both configurations. For example, at 7 degrees of sideslip the pressure drop on the leeward wing FS 19.06 for the twin tail is predicted very well (Figure 4.38). The level of peak suction pressure on the windward wing is over-predicted for both configurations at the first two wing stations (FS 19.06 and 23.56). In the region of the twin tails (FS 28.06) the SPLITFLOW prediction captures the level of suction seen in the data. Since the centerline tail prediction contains a large overprediction of the peak suction pressure at this station, the incremental change in integrated rolling moment will be overestimated by the code. This is borne out in the force and moment data comparisons shown in previous sections where the rolling moment was much more closely matched by SPLIT-FLOW for the twin tail than for the centerline tail.

The comparison of code pressure predictions to test data for the twin tail configuration at Mach 0.85 is shown in Figure 4.39 to Figure 4.41. The predictions are much closer to the test pressure data, including estimates of the peak pressure levels for both tail positions. The trends of pressure levels generated by the change in tail position are predicted by the code and this is reflected in the force and moment comparisons shown earlier for a Mach number of 0.85. The degree of agreement between predicted and test pressure results at this Mach number on the wing is considered to be good. As an example, the sideslip of 7 degree case (Figure 4.41) shows that the code captures the extremely nonlinear breaks in the spanwise pressure distribution at FS 28.06. However, the forebody pressures are not predicted as well. The forebody geometry is the same for the two tail configurations, so the computed solution seems to indicate the forebody solution is sensitive to tail arrangement. However, the Mach 0.4 case shown in Figure 4.36 to Figure 4.38 show better agreement between the two configu-

rations for the forebody pressures. The cause of the difference in the Mach 0.85 cases may be in the level of grid refinement that took place in the forebody region.

5. Results using Navier-Stokes Version of SPLITFLOW

With the contract monitor's permission, a viscous analysis of one case was made using the hybrid grid version of SPLITFLOW. The case selected was one in which the Euler analysis tended to have difficulty converging; the centerline tail geometry at Mach number of 0.4, and sideslip angles of four and seven degrees at an angle-of-attack of 25 degrees. The viscous analysis provided indications of flow unsteadiness, explaining the reason for the convergence difficulties in the inviscid case. This was a pilot effort in implementing viscous capability in SPLITFLOW, and an effective strategy had not yet been devised for efficient problem setup. The purpose of the analysis was to demonstrate hybrid grid technology, and to compare viscous and inviscid flowfields for a high angle of attack case with sideslip..

A viscous analysis using the hybrid version of SPLITFLOW begins with the generation of a prismatic grid about the aircraft surface. The prismatic grid is produced by marching the surface triangulation outward along carefully computed normal vectors at the grid nodes. The procedure is briefly described in Ref. 9. Typically ten to twenty grid layers are generated in the final prismatic grid.

The surface mesh used for the viscous case was modified from the surface mesh used to define the geometry for the inviscid analyses. A finer surface grid resolution was desired near the leading edge and trailing edge of the wing and the leading edge of the forebody. Therefore, the CAD program was used to produce a facet file containing 46,214 triangular facets on the MTVI surface. This surface mesh was marched out 21 layers, producing a prismatic grid containing 970,494 triangular-prismatic elements. A view of the prismatic grid near the vertical tail is shown in Figure 5.1.

The Cartesian grid then uses the outer layer of the prismatic grid as its boundary surface for the initial grid generation process. Subsequent refinement of the Cartesian grid was based on flowfield gradients in Mach number, turbulent length scale and helicity. Inclusion of the turbulent length scale probably resulted in some grid refinement at the interface between the prismatic and Cartesian grid that was unnecessary. The Cartesian grid was prohibited from growing any larger due to the user specified target number of cells. The prismatic grid is not refined as part of the grid adaption process. However, the user may elect to regenerate the prismatic grid external to the flow solver and reinsert the new grid into the Cartesian grid. This is sometimes necessary if the geometry is changed or if the grid resolution in the boundary layer is inadequate. The prismatic grid in this analysis was generated once and held constant during the coarse of the solution.

The convergence histories are shown in Figure 5.2 and Figure 5.3. The force and moment his-

21

tories for the viscous and inviscid analyses are shown in the figures. The improvement in the integrated forces and moments, as compared to the test data, is apparent. Some oscillations occur in the side force plot and the moment plots. The oscillation is likely caused by the unsteadiness of this particular case in the separated region on the aft portion of the wing after the vortex burst. The Cartesian portion of the hybrid grid grew from 87,209 total cells to 448,345 total cells, over the course of the grid adaption for the entire analysis.

Comparison of the surface pressures is shown in Figure 5.4. There is an improvement in the agreement with the test data, as expected. The forebody suction pressures are no longer over-predicted, but instead are underpredicted. The agreement is better on the leeward side where the vortex is weaker. Refinement of the Cartesian grid in the forebody region was relatively poor due to the smaller gradients in the region relative to the gradients over the wing and the limited amount of refinement that was allowed. An improved resolution of the vortex could improve the suction peak pressure further. The pressure comparisons over wing show excellent agreement with the test data on the leeward side of the vehicle. The computed pressures on the windward side tended to oscillate through the data for the last station, possibly indicating the unsteadiness of the flowfield. This oscillation was also seen in the Cp contour plots over the wing to be shown later.

Figure 5.5 through Figure 5.10 show the difference in the pressure field between the inviscid and viscous solution at the six axial stations. The contour levels were set identical for the two solutions so a direct comparison can be made. The improved grid resolution of the forebody vortex is evident in the inviscid solution. However, the vortex core over the wing sections tended to be more resolved for the viscous case.

Figure 5.11 through Figure 5.16 show the differences in the Mach number contours between the inviscid and viscous solutions at the six axial stations. Identical contour levels were selected for the plots. The interesting feature in this series of plots is the apparent bursting of the vortex at the last station on the windward side of the vehicle. The inviscid solution did not show any indication of vortex burst.

Velocity vectors for the fifth axial station on the windward side of the vehicle are shown in Figure 5.17. The inviscid solution does not resolve the secondary vortex. Instead, the inviscid solution shows a weak crossflow shock on the upper surface in the vicinity of the secondary vortex in the viscous solution. The location of the weak shock is indicated in the figure. The compression from the crossflow shock is not visible in the pressure comparison, Figure 5.4, due to the large amount of expansion around the leading edge region in the inviscid solution.

The inviscid integrated force and moment data, Figure 5.18, are shown with the Navier-Stokes integrated results at two sideslip angles. The viscous results indicated unsteady flow, as the forces and moments showed oscillatory behavior even at the end of the computations. This is likely to be a characteristic of the test data as well at these flow conditions. The pre-

dicted data has been taken as the average of the last 100 steps in each calculation. The results show that the viscous resultsand the trend with sideslip are much closer to the test data than the Euler predictions.

The comparison of the effect of transonic conditions on vortex behavior can be cataloged using the classical vortex characterization of Miller and Wood (Ref. 10), depending on the local Mach number and angle-of-attack defined normal to the leading edge. The correlation from Ref. 10 is shown in Figure 5.19. The leading-edge sweep of the MTVI configuration of 60 degrees was used to compute the range of local Mach number and angle of attack for Case 1 through 4 in the run matrix; these correspond to the two dashed lines that have been added to the upper left portion of the figure. Thus, the MTVI test data should exhibit subsonic vortex behavior at Mach 0.4, and should indicate supersonic vortex characteristics at the higher angles of attach at Mach 0.85. Local supersonic flow at Mach 0.85 was inferred from the test data,since the critical pressure coefficient was exceeded on the surface. It is noted that the test configuration has a combined vortical flowfield from the forebody chine and wing, which is not part of the correlated data.

The inviscid Euler predictions cannot be directly compared with the Miller and Wood correlations. The viscous SPLITFLOW results, for one sideslip case at Mach 0.4, provide a comparison between inviscid and viscous simulations of local conditions (seen in Figure 5.17). The inviscid results indicated a crossflow shock on the windward wing. This is consistent with the Euler predictions from Ref. 3, which showed crossflow shocks developed on a 65-degree swept wing at a freestream Mach number of 0.5 and an angle-of-attack of 20 degrees. The viscous prediction for the MTVI shows all subsonic flow on the windward side. Returning to Figure 5.19, the geometric location of the case 5 centerline tail configuration at a sideslip angle of 4 degrees is shown as two data points on either side of the angle of attack trend line plotted earlier. These two locating points correspond to the leeward and windward wing effective angles-of-attack for the viscous case (α=25 degrees, β=4 degrees), which is consistent with the Miller and Wood correlation for this Mach number and angle of attack.

6. Conclusions

Results of this study showed that the SPLITFLOW code predicted the trends of configuration forces and moments up to 7 degrees of sideslip at angles-of-attack to 30 degrees. The results also indicate that the SPLITFLOW Euler code provides reliable prediction of the trends due to compressibility over a wide range of angles-of-attack and angles of sideslip for the MTVI configuration with both the centerline tail and twin tail arrangements. These trends are useful for preliminary design of flight vehicles, where rapid configuration evolution does not permit wind tunnel evaluation of geometry modifications before configuration selections are made. The predictions of forces and surface pressures were representative of the data, with some deviation from the data occurring mainly in the prediction of peak surface pressure lev-

els. Typical of Euler inviscid simulations, the code produced overprediction of the level of peak suction Cp generated on wing leading edges and chine forebody regions, especially at higher angles-of-attack and at the subsonic freestream conditions. SPLITFLOW incorporates a relatively low-dissipative numerical scheme by combining the superbee flux limiter with a compression parameter. Also, the grid refinement available in the code reduces local cell size near discontinuities, reducing numerical viscosity. The predictions at transonic conditions, where the value of vacuum pressure coefficient is substantially reduced, were much closer to the measured surface pressure data. The general prediction capability of SPLITFLOW for transonic surface pressures is very favorable, even for the complex multiple-vortical flows used in this study. The inviscid analysis reliably predicts the aerodynamic trends in configuration angle-of-attack or yaw, or configuration shape variations such as tail placement.

The viscous analysis for two sideslip angles at Mach 0.4 demonstrated the approach for computing viscous flowfields using SPLITFLOW technology. The results showed improved comparisons with the test data, particularly the integrated forces and moments. Additional calibration work is required to determine the additional accuracy gained using a Navier-Stokes solver over an Euler solver for these configurations and the feasibility of performing the analyses in a timely manner for preliminary design. The flowfield predicted with Navier-Stokes showed evidence of unsteadiness, making the results somewhat preliminary until a solution strategy emerges for these solutions.

Specific recommendations are made for future studies. The need exists to rapidly and accurately predict the control effectiveness of control surfaces and the hinge moments for leading-edge flaps. It is suggested that additional Euler comparisons be made using force and pressure data for deflected flaps and control surfaces. A quantification of the Mach number dependence on lateral-directional prediction capability of Euler solutions for forebody flows would provide assistance to the design community.

7. Acknowledgments

References

1. Karman, S.L. Jr., "SPLITFLOW: a 3D Unstructured Cartesian/Prismatic Grid CFD Code for Complex Geometries," AIAA-95-0343, Jan. 1995.

2. Finley, D.B., "Euler Technology Assessment Program for Preliminary Aircraft Design Employing SPLITFLOW Code with Cartesian Unstructured Grid Method," NASA CR-4649, March 1995.

3. Hoeijmakers, H.W.M., "Modeling and Numerical Simulation of Vortex Flow in Aerodynamics," AGARD-CP-494, Vortex Flow Aerodynamics, July 1991.

4. Finley, D.B., "Application of Euler Method to Transonic Flow Computation of a Hypersonic Configuration," ICAS-94-5.2, Oct., 1994.

5. Hall, R.M., private communications

6. Ghaffari, F., "On the Vortical-Flow Prediction Capability of an Unstructured-Grid Euler Solver," AIAA-94-0163.

7. Munz, C., "On the Numerical Dissipation of High Resolution Schemes for Hyperbolic Conservation Laws," Journal of Computational Physics, vol. 77, 1988, pp. 18-39.

8. Harten, A., "High-Resolution Schemes for Hyperbolic Conservation Laws," Journal of Computational Physics, vol. 49, 1983, pp. 357-393.

9. Karman, S.L. Jr., "Unstructured Cartesian/Prismatic Grid Generation for Complex Geometries," NASA CP-3291, May 9-11, 1995. pp. 251-270.

10. Miller, D.S., and Wood, R.M., "An Investigation of Wing Leading-Edge Vortices at Supersonic Speeds," AIAA-83-1816, July 1983.

Table 4.1 Run Matrix for Computational Study

Case	α, degrees	β, degrees	M_∞	Vertical Tail
1	10, 15, 20, 25, 30	0	0.40	centerline
2	10, 15, 20, 25, 30	0	0.85	centerline
3	10, 12.5, 15, 17.5, 20, 25, 30	0	0.40	twin
4	10, 12.5, 15, 17.5, 20, 25, 30	0	0.85	twin
5	15, 25	2, 4, 7	0.40	centerline
6	15, 25	2, 4, 7	0.85	centerline
7	25	2, 4, 7	0.40	twin
8	25	2, 4, 7	0.85	twin

Centerline tail configuration
Perspective view

Side view showing surface facet definition

Top view showing surface facet definition
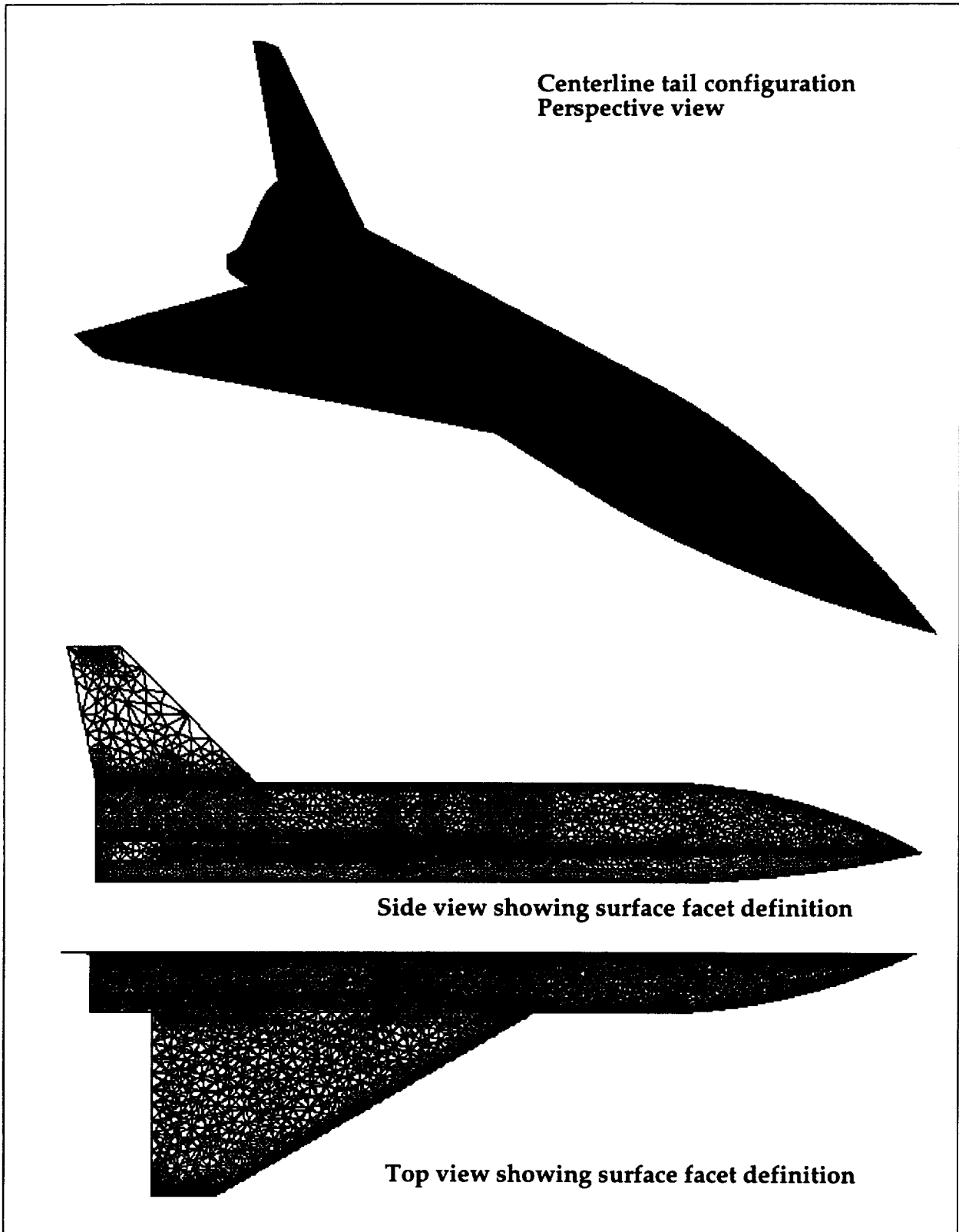
Figure 3.1 Centerline tail MTVI configuration.

Twin tail configuration
Perspective view

Side view showing surface facet definition

Top view showing surface facet definition
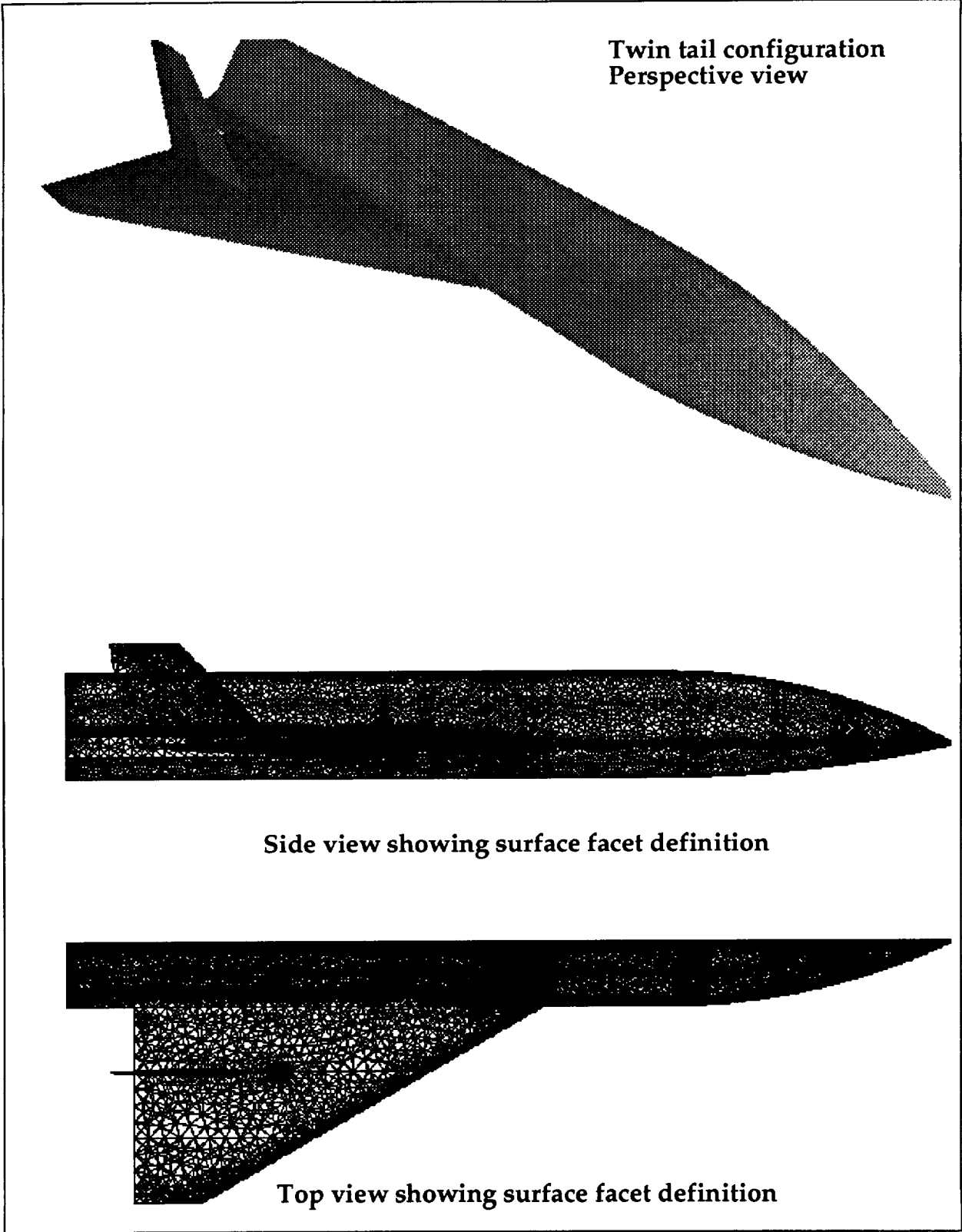
Figure 3.2 Twin tail MTVI configuration.

27

Cartesian grid at fuselage stations

Centerline tall

α = 30 deg

Mach = 0.85

Euler solution
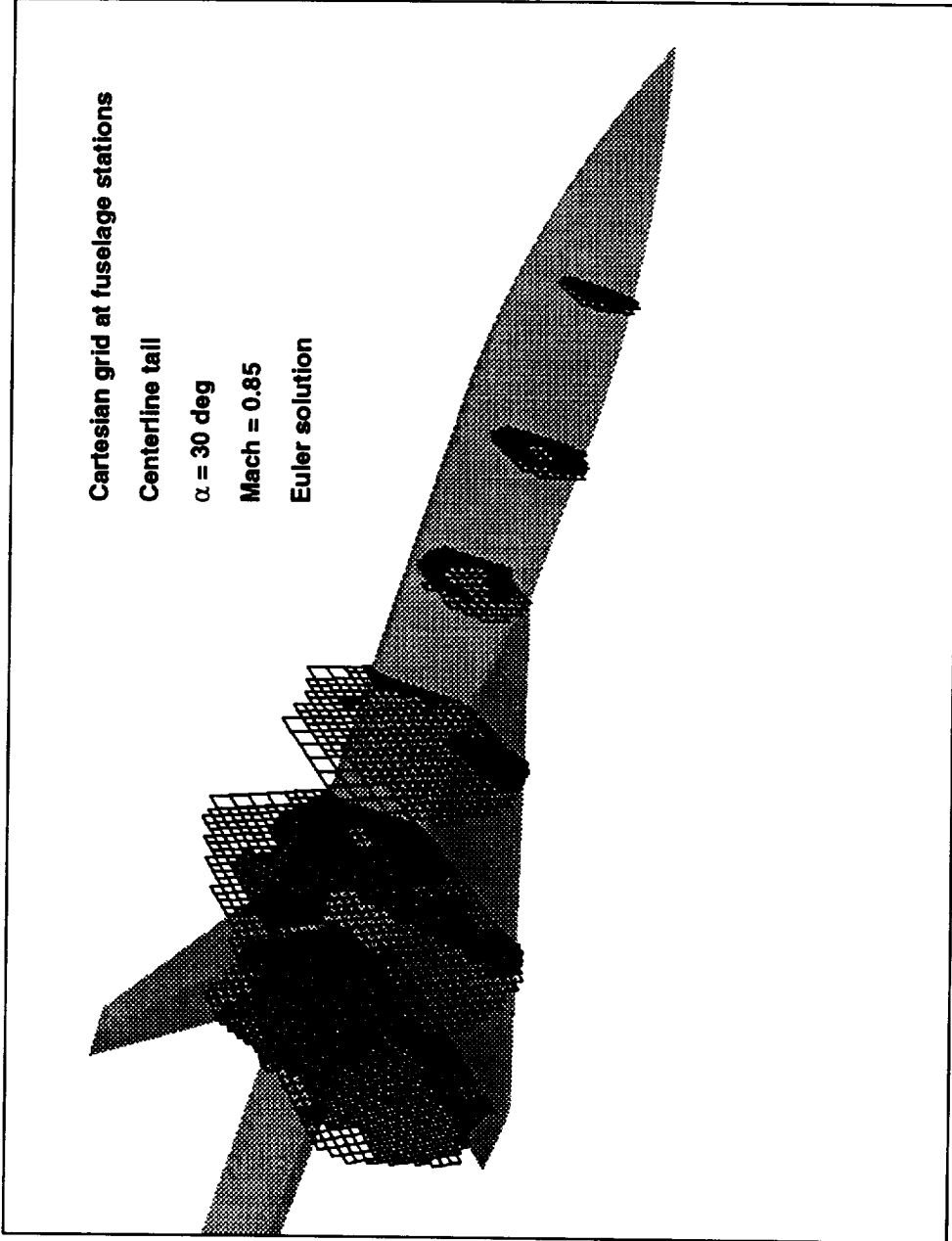
Figure 3.3 Example of final adapted Cartesian grid at selected fuselage stations.

28
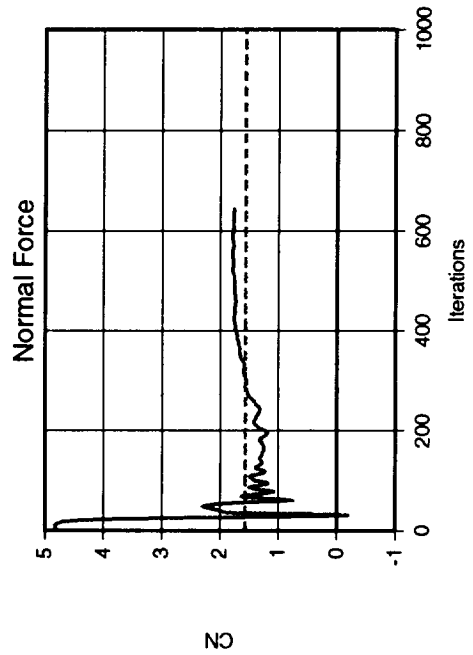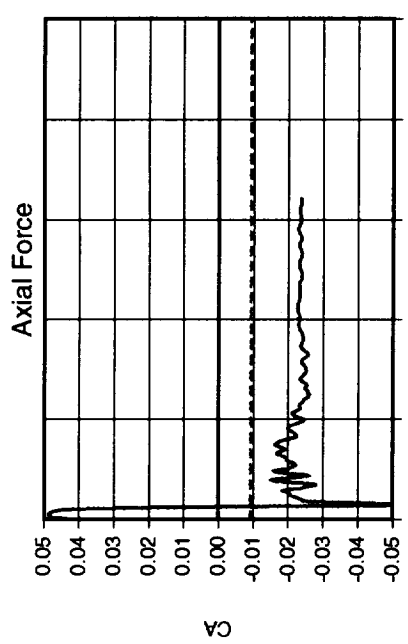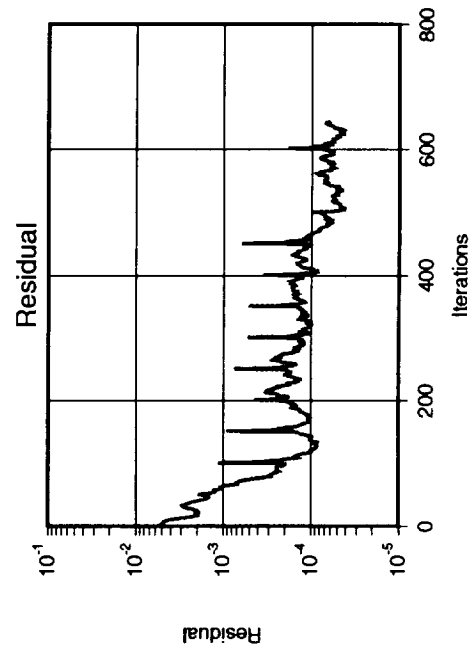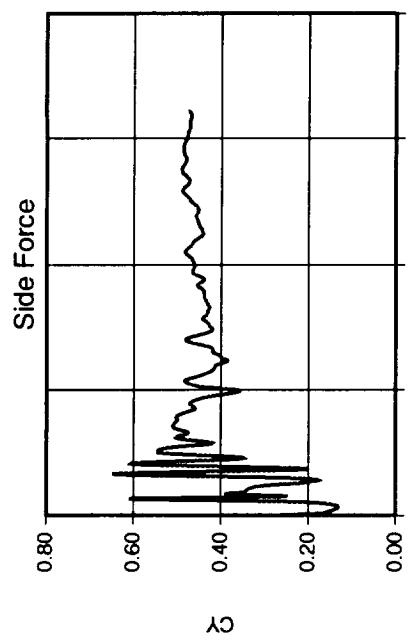
Figure 3.4 Sample force histories for symmetric solution.
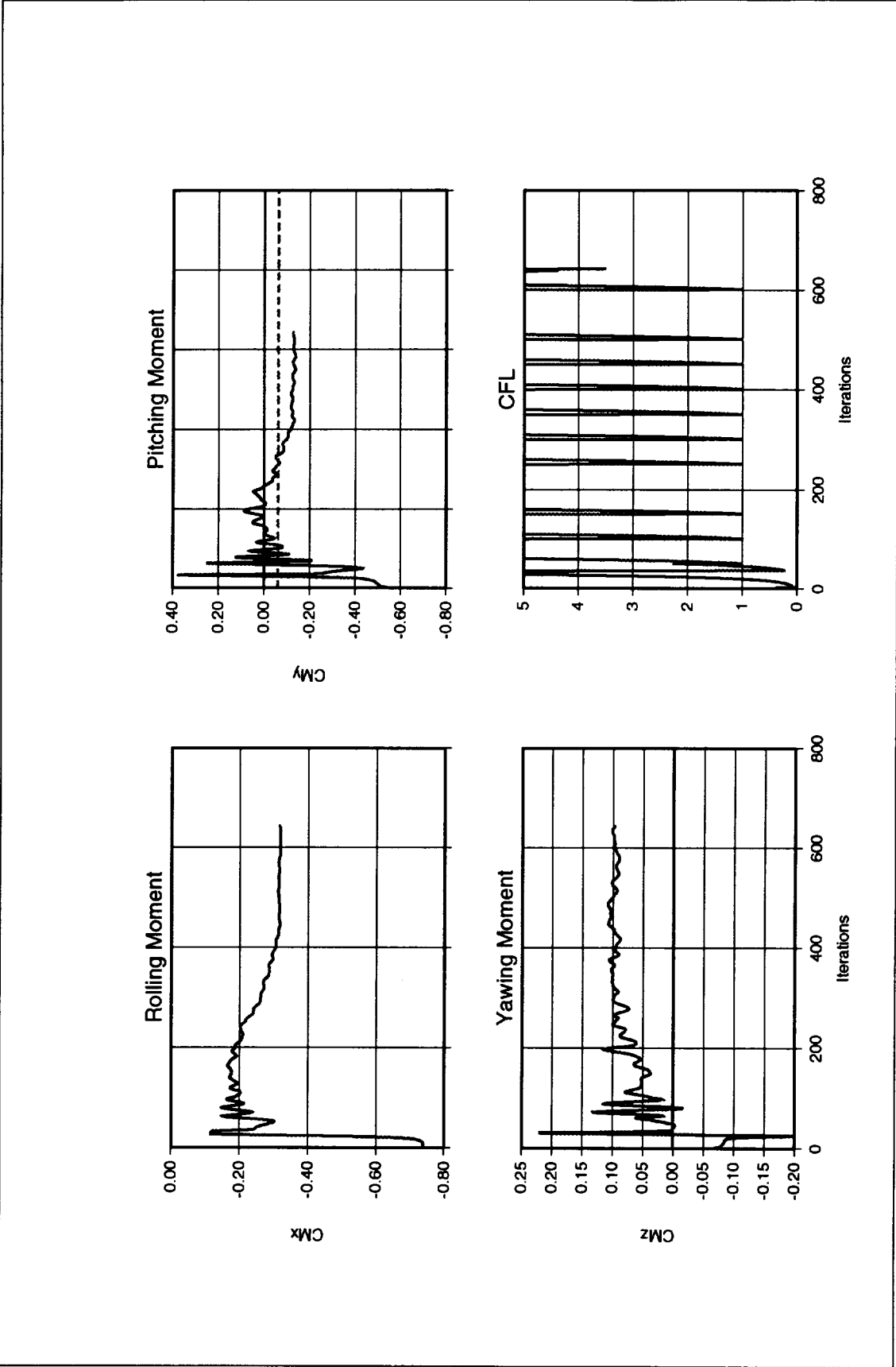
Figure 3.5 Sample moment histories for symmetric solution.
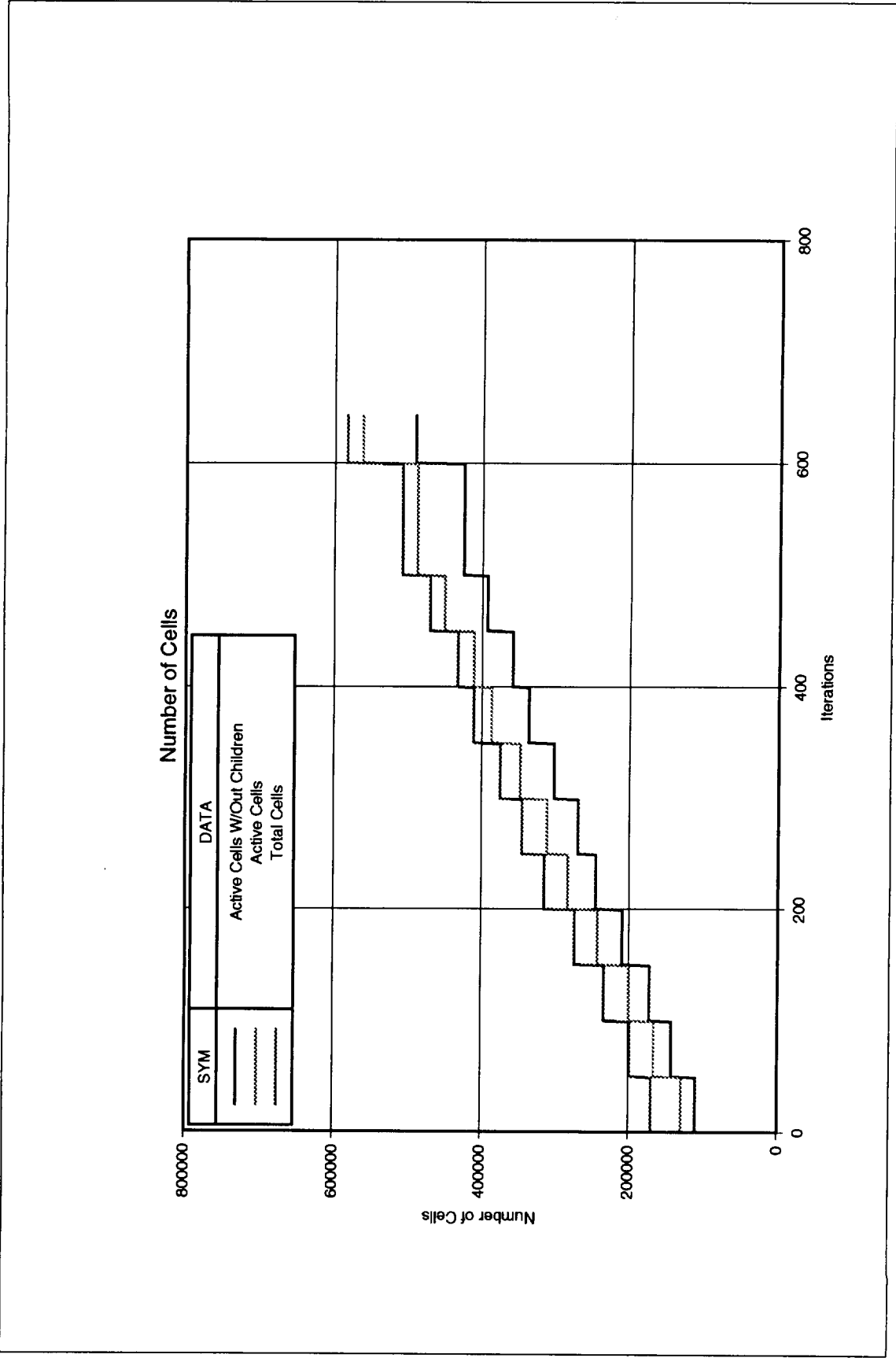
Figure 3.6 Sample cell count histories for symmetric solution.
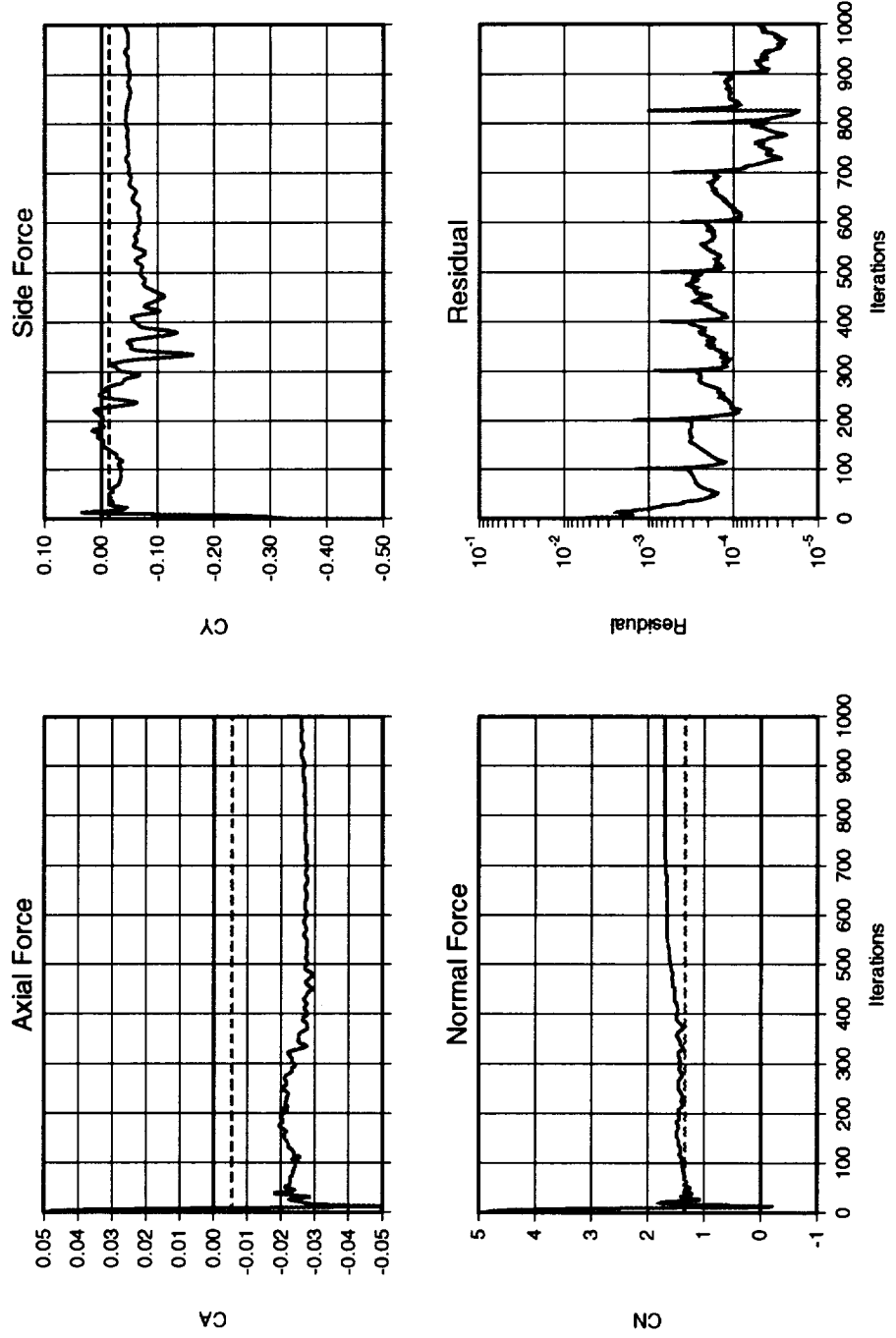
Figure 3.7 Sample force histories for sideslip solution.
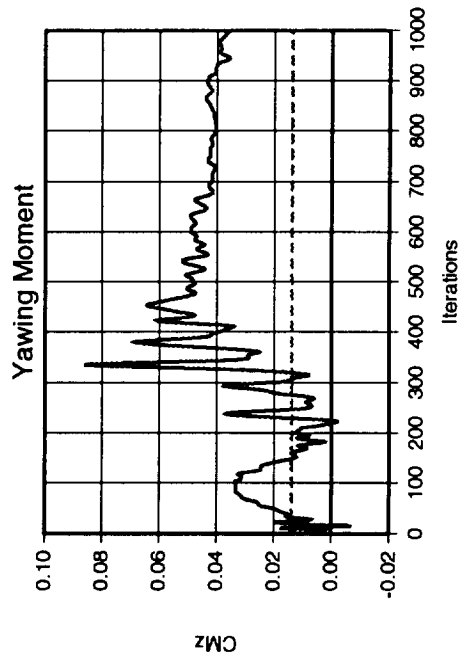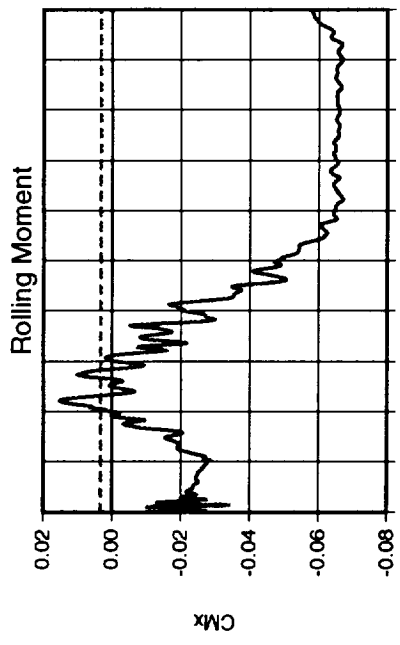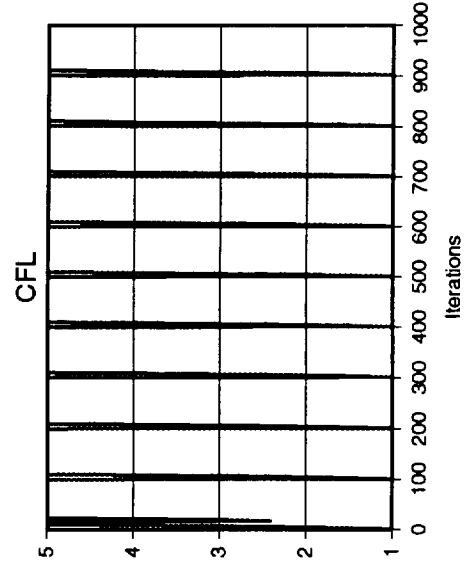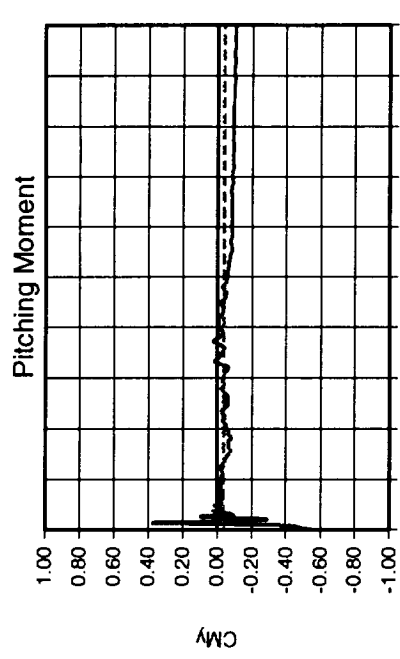
Figure 3.8 Sample moment histories for sideslip solution.
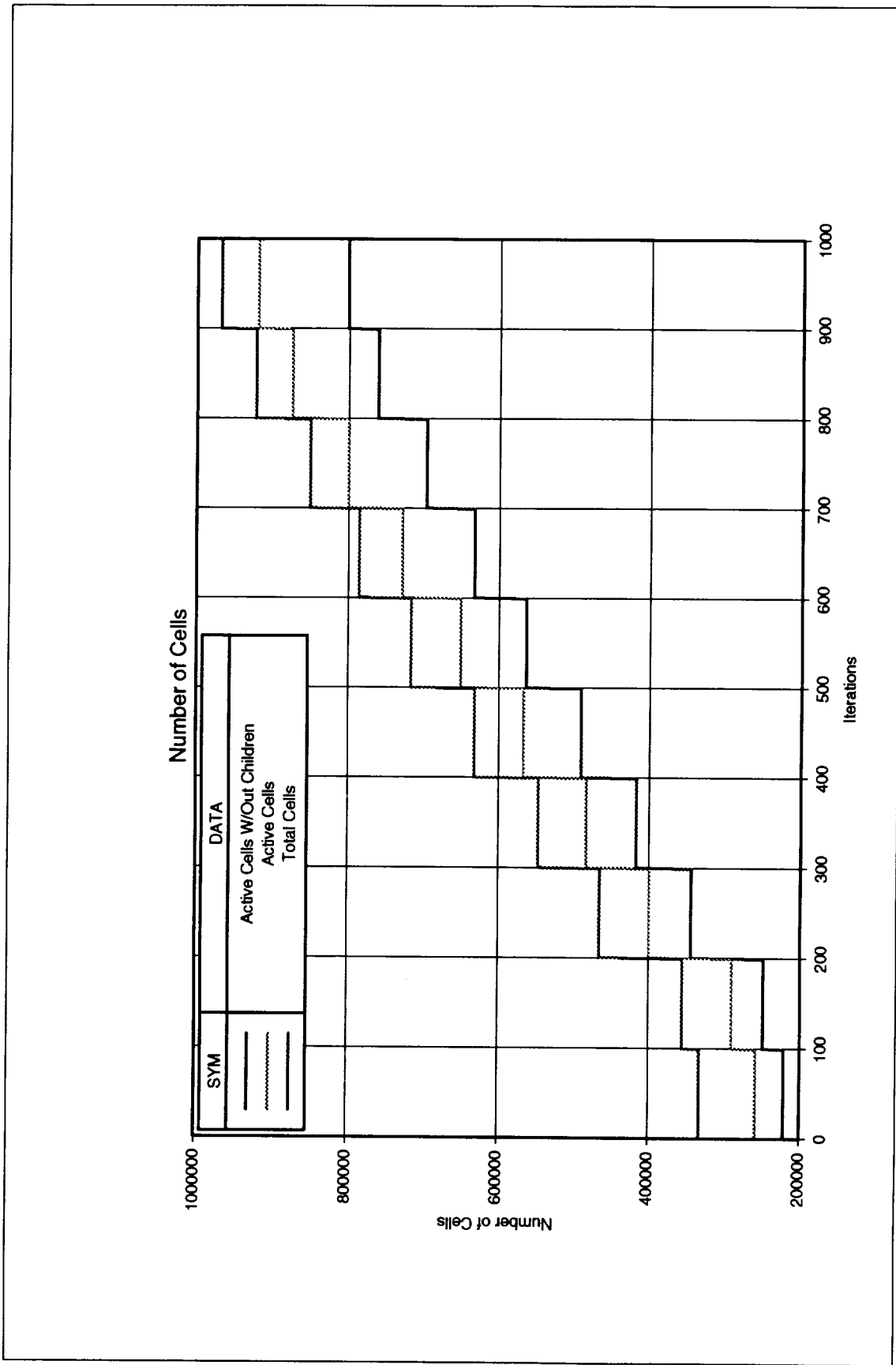
Figure 3.9 Sample cell count histories for sideslip solution.
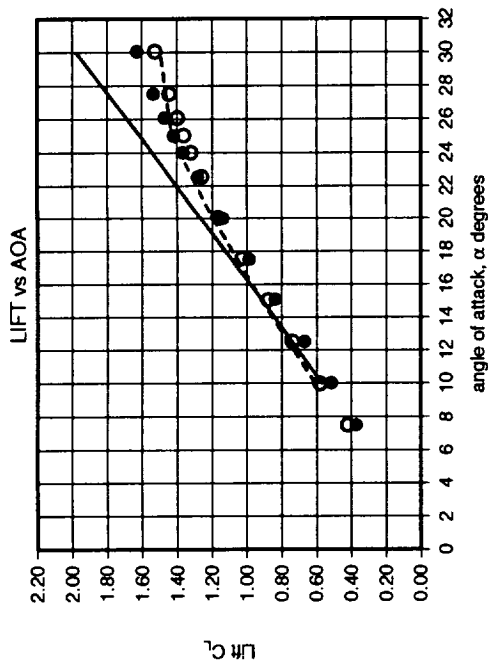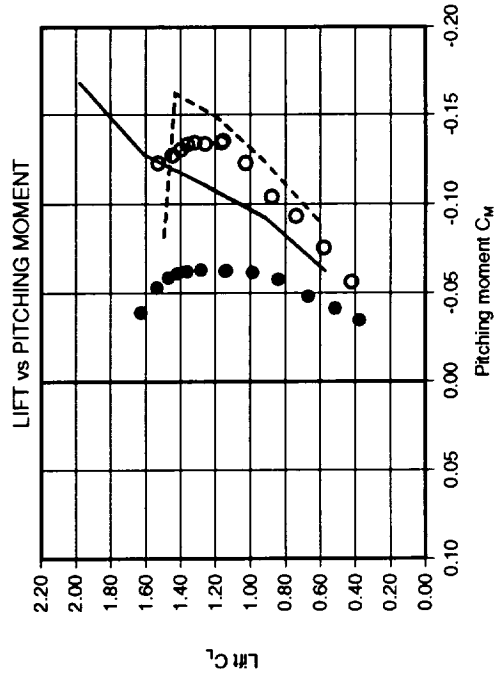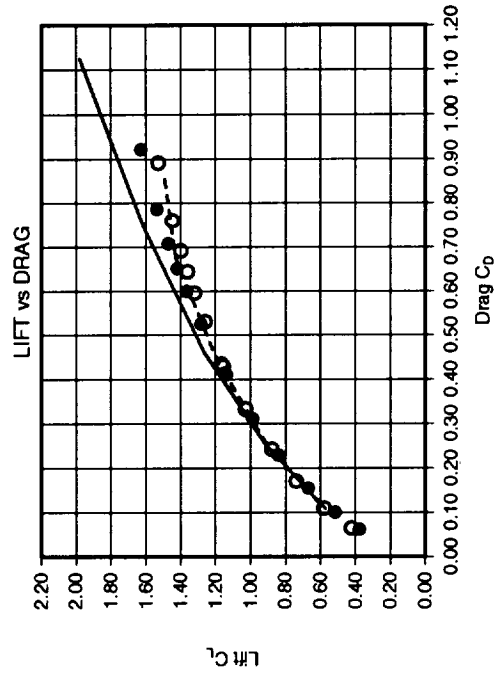
Figure 4.1 Lift, drag and pitching moment comparison to test data for symmetric centerline tail solution.
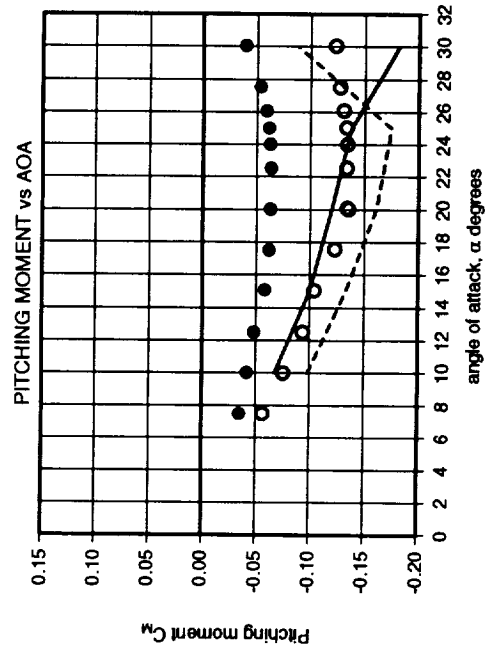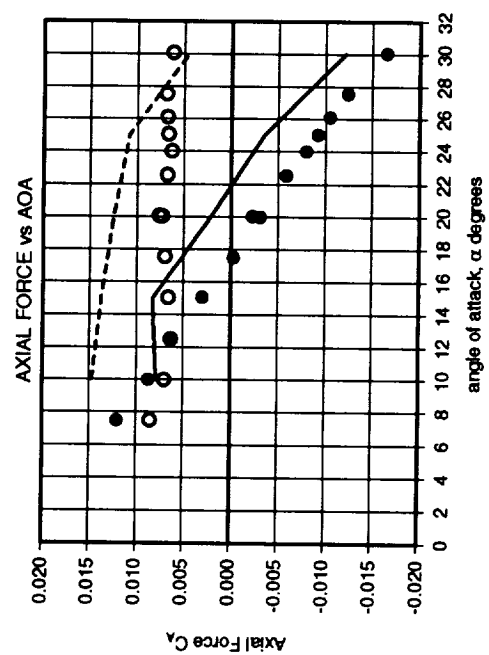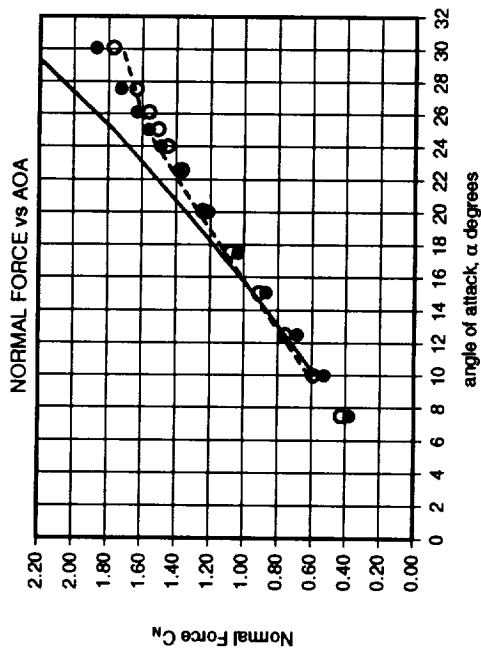
35

Figure 4.2 Normal force, axial force and pitching moment comparison to test data for symmetric centerline tail solution.
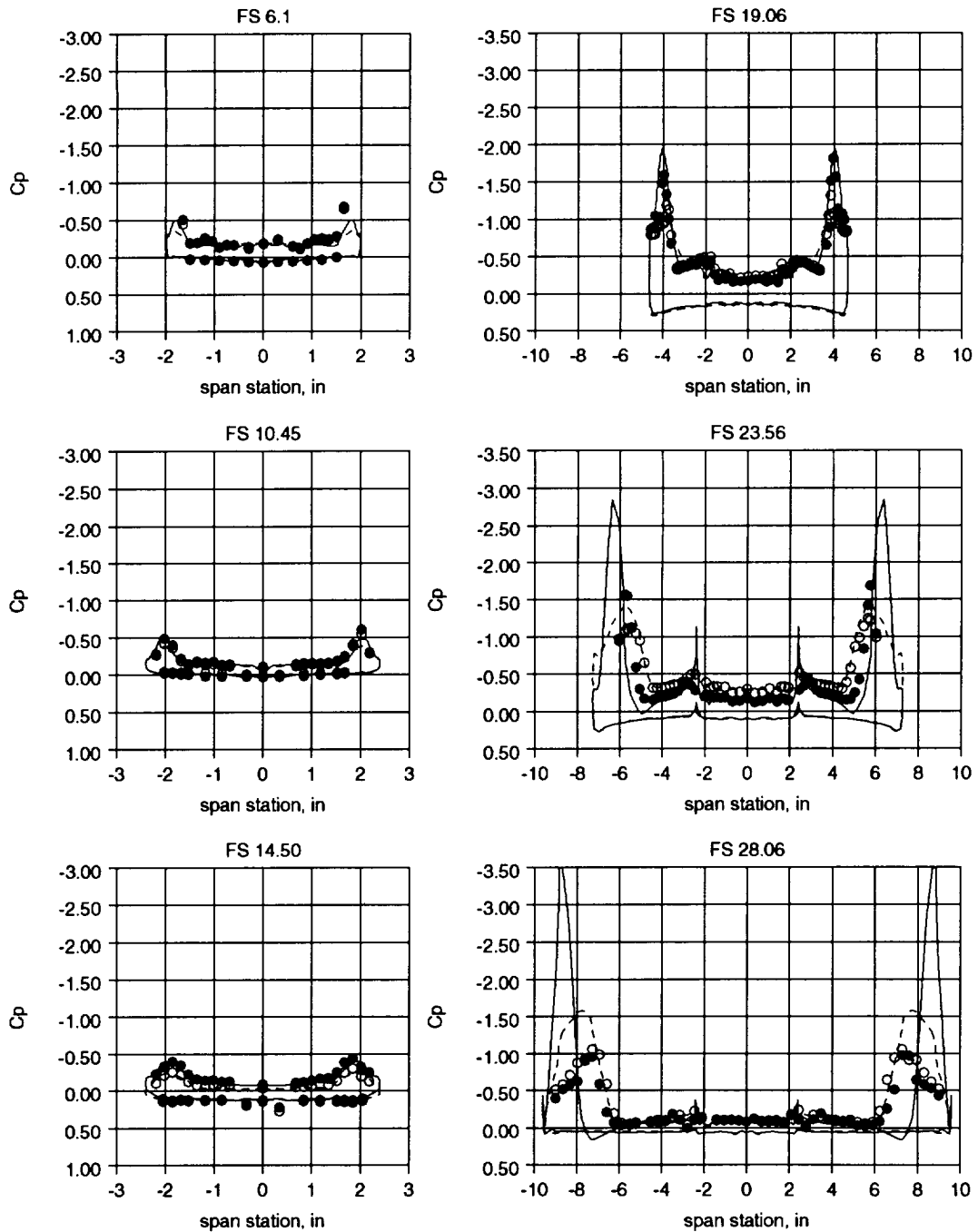
Figure 4.3 Surface pressure comparison to test data for symmetric centerline tail configuration at 10 degrees angle-of-attack.

Figure 4.4 Surface pressure comparison to test data for symmetric centerline tail configuration at 15 degrees angle-of-attack.

Figure 4.5 Surface pressure comparison to test data for symmetric centerline tail configuration at 20 degrees angle-of-attack.

39

Figure 4.6 Surface pressure comparison to test data for symmetric centerline tail configuration at 25 degrees angle-of-attack.

Figure 4.7 Surface pressure comparison to test data for symmetric centerline tail configuration at 30 degrees angle-of-attack.

41
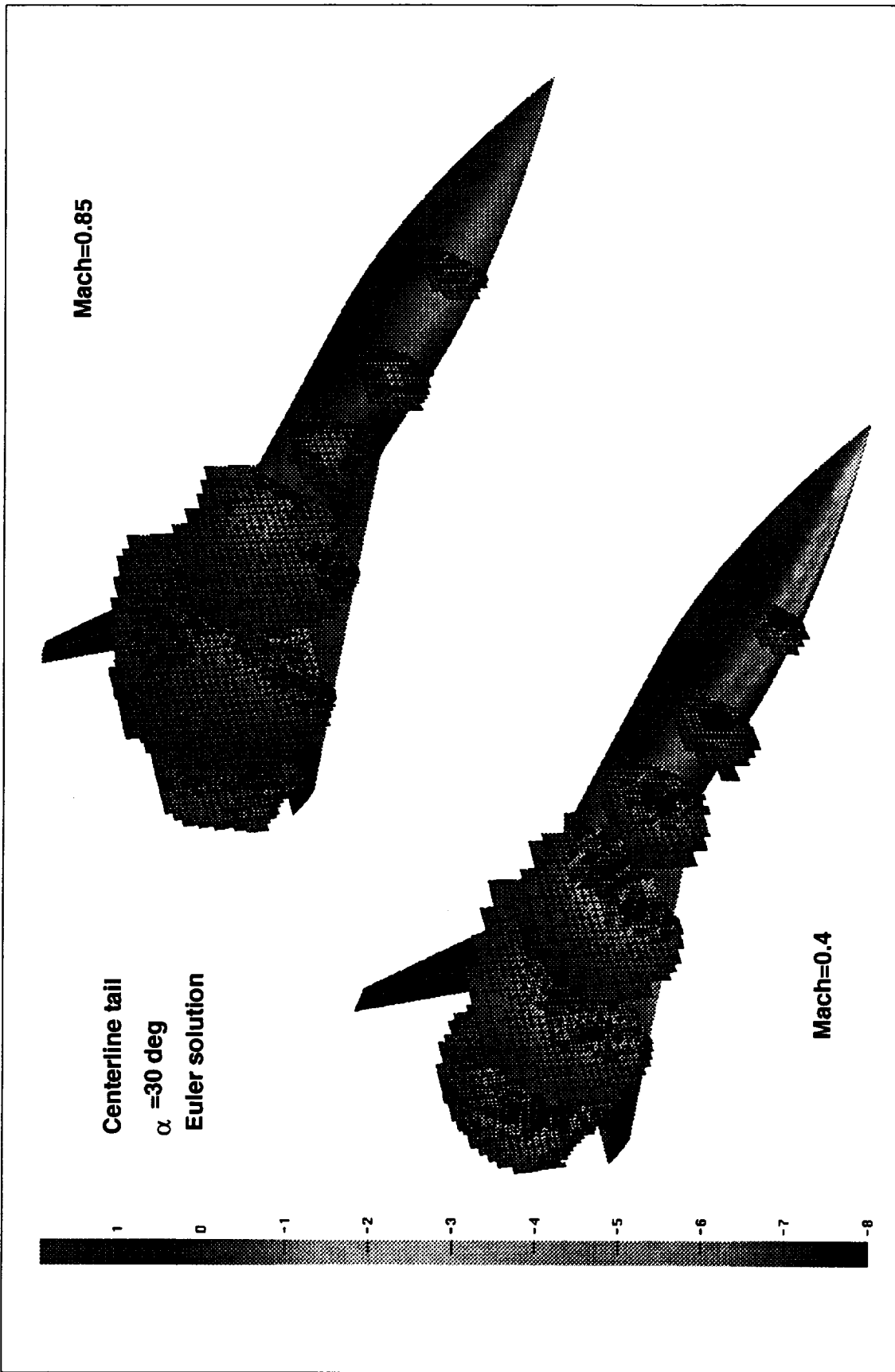
Figure 4.8 Effect of Mach number on Cp for centerline tail configuration.
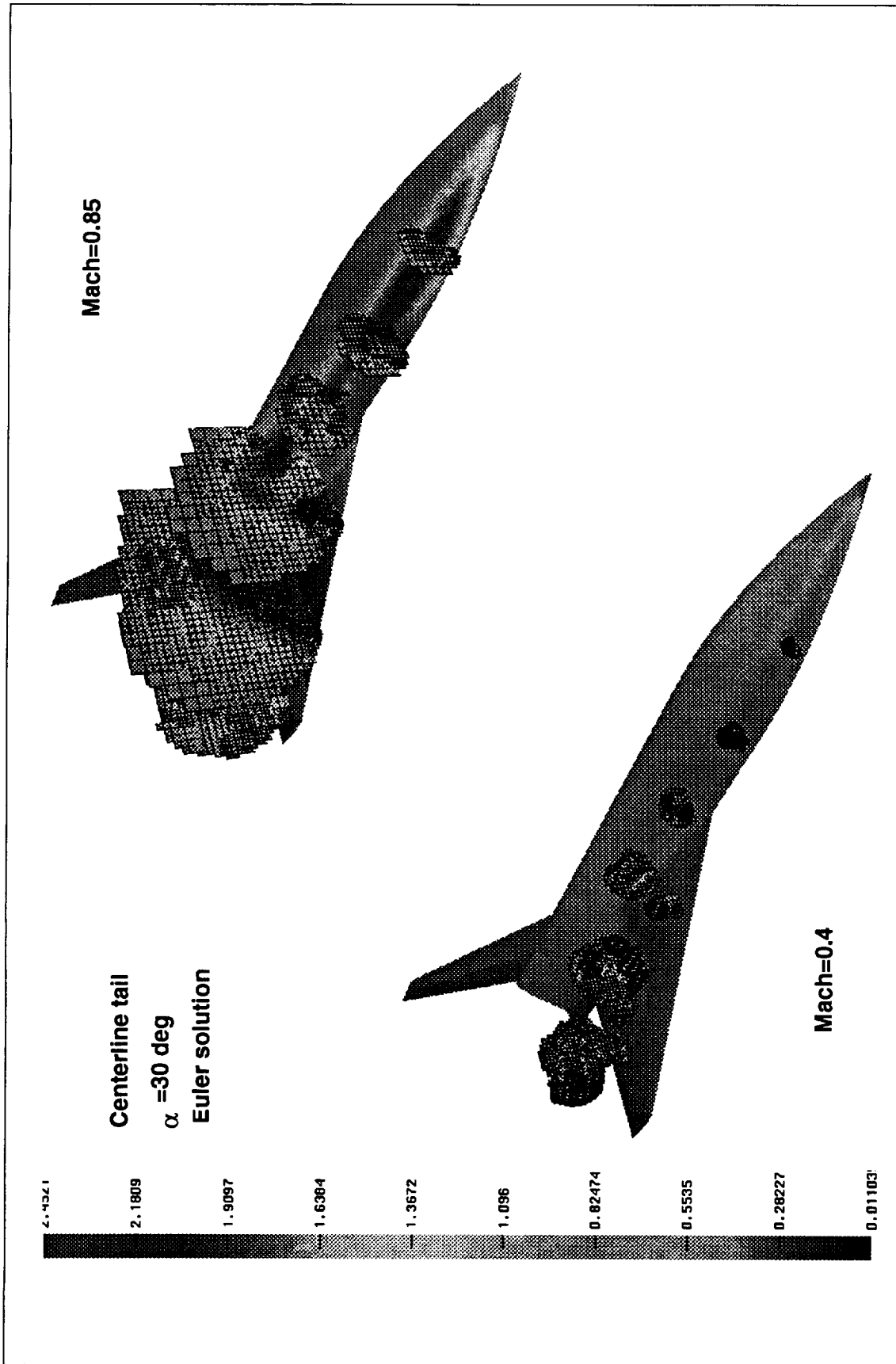
Figure 4.9 Effect of Mach number on local Mach number for centerline tail configuration.
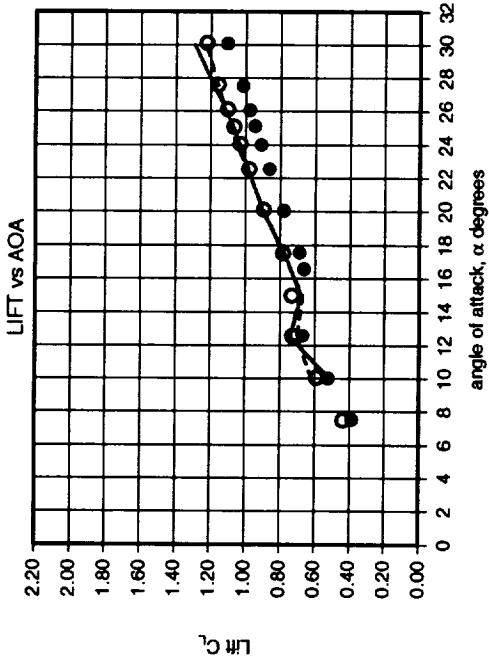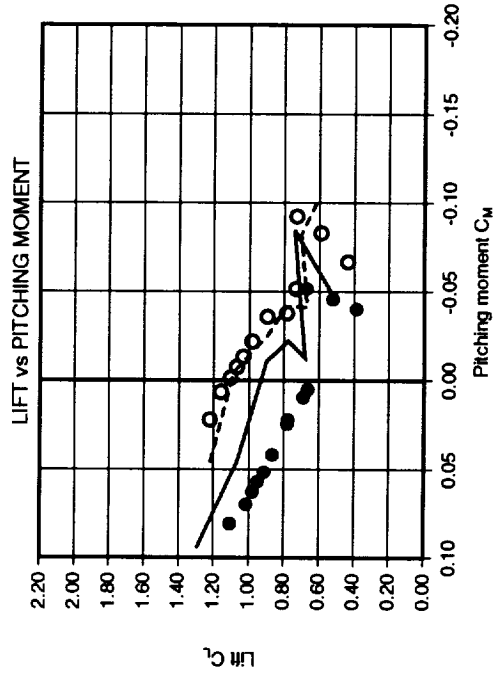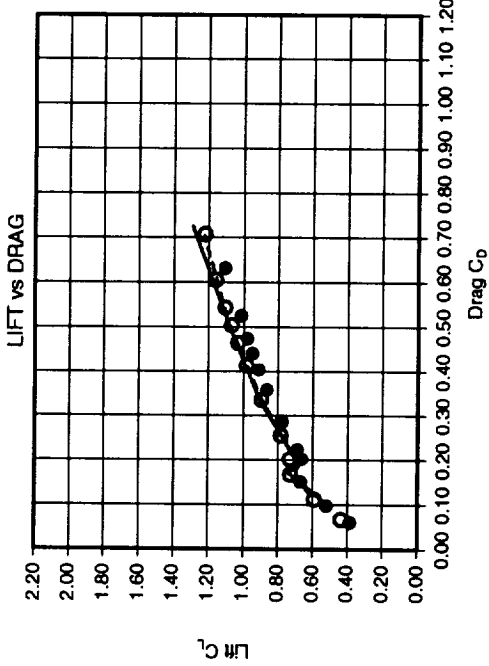
Figure 4.10 Lift, drag and pitching moment comparison to test data for symmetric twin tail solution.
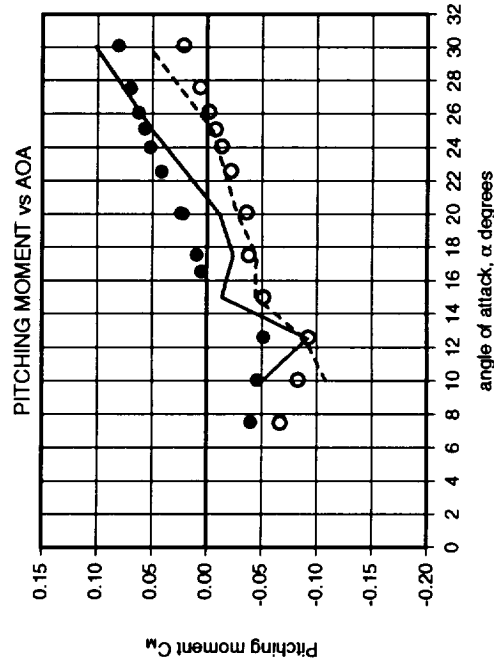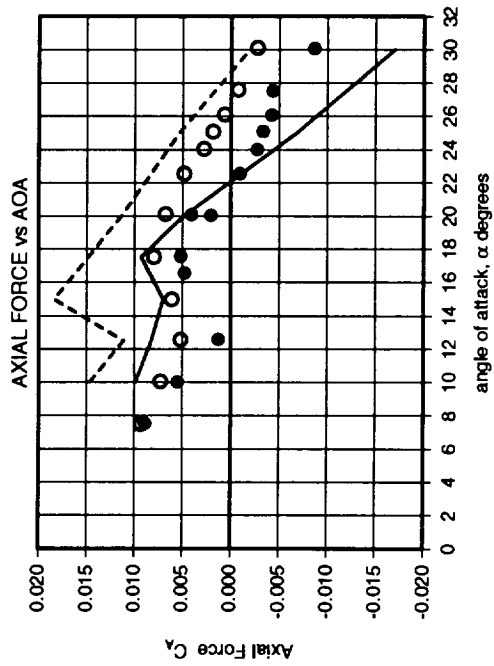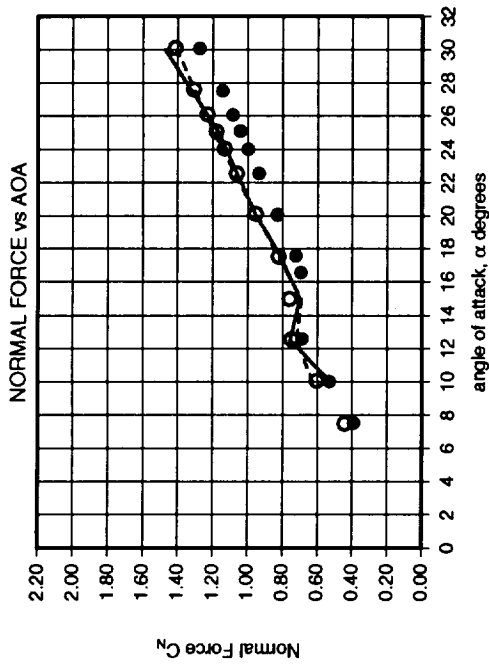
Figure 4.11 Normal force, axial force and pitching moment comparison to test data for symmetric twin tail solution.
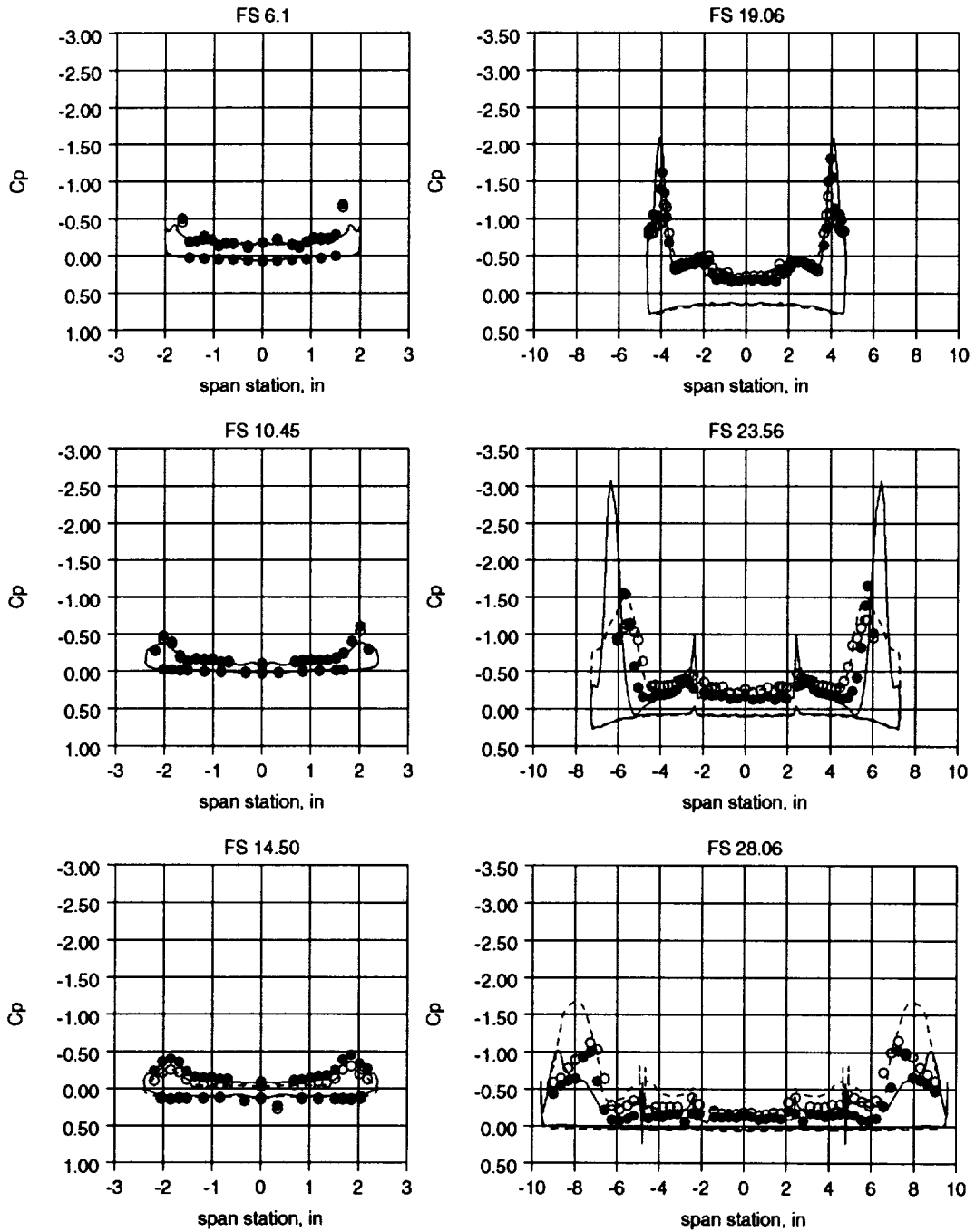
Figure 4.12 Surface pressure comparison to test data for symmetric twin tail configuration at 10 degrees angle-of-attack.

46

Figure 4.13 Surface pressure comparison to test data for symmetric twin tail configuration at 12.5 degrees angle-of-attack.

47

SYM	Data	Geometry	Mach	α
——————	SPLITFLOW	Twin Tail	Mach=0.40	15.0
— — — — —	SPLITFLOW	Twin Tail	Mach=0.85	15.0
●	Test	Twin Tail	Mach=0.40	15.0
○	Test	Twin Tail	Mach=0.85	15.0
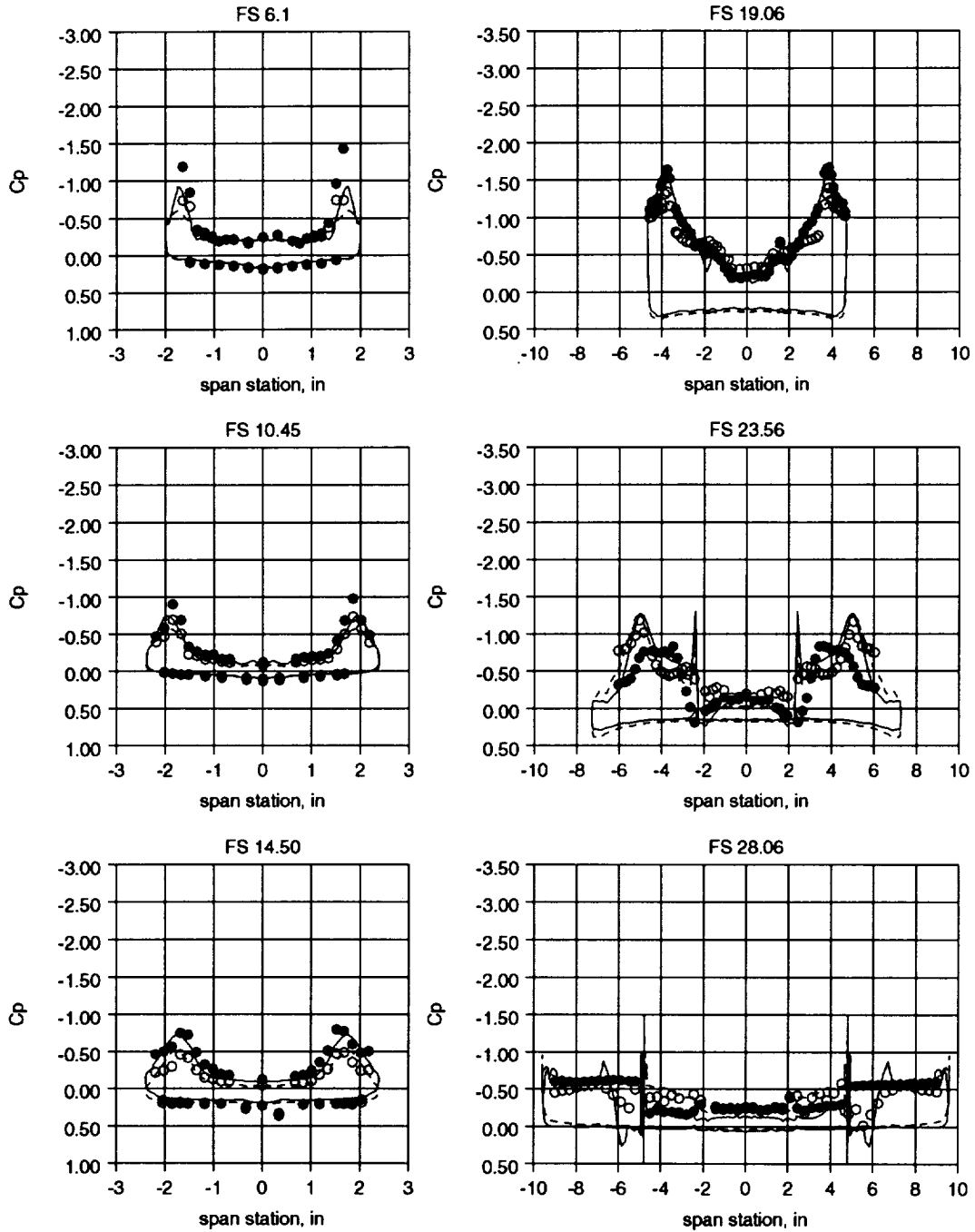
Figure 4.14 Surface pressure comparison to test data for symmetric twin tail configuration at 15 degrees angle-of-attack.

48

Figure 4.15 Surface pressure comparison to test data for symmetric twin tail configuration at 17.5 degrees angle-of-attack.

49

Figure 4.16 Surface pressure comparison to test data for symmetric twin tail configuration at 20 degrees angle-of-attack.

SYM	Data	Geometry	Mach	α
——	SPLITFLOW	Twin Tail	Mach=0.40	25.0
- - - -	SPLITFLOW	Twin Tail	Mach=0.85	25.0
●	Test	Twin Tail	Mach=0.40	25.0
○	Test	Twin Tail	Mach=0.85	25.0
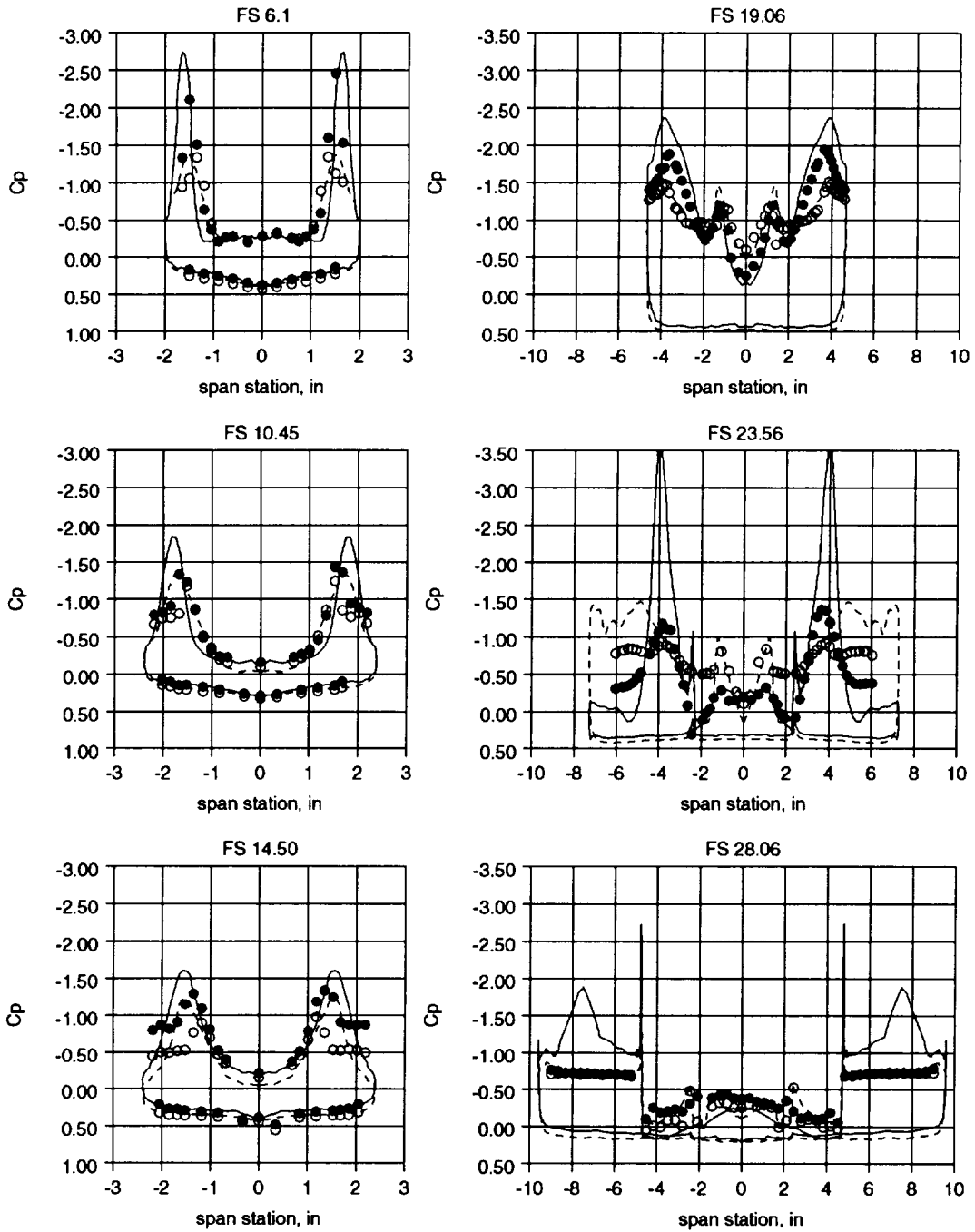
Figure 4.17 Surface pressure comparison to test data for symmetric twin tail configuration at 25 degrees angle-of-attack.

51
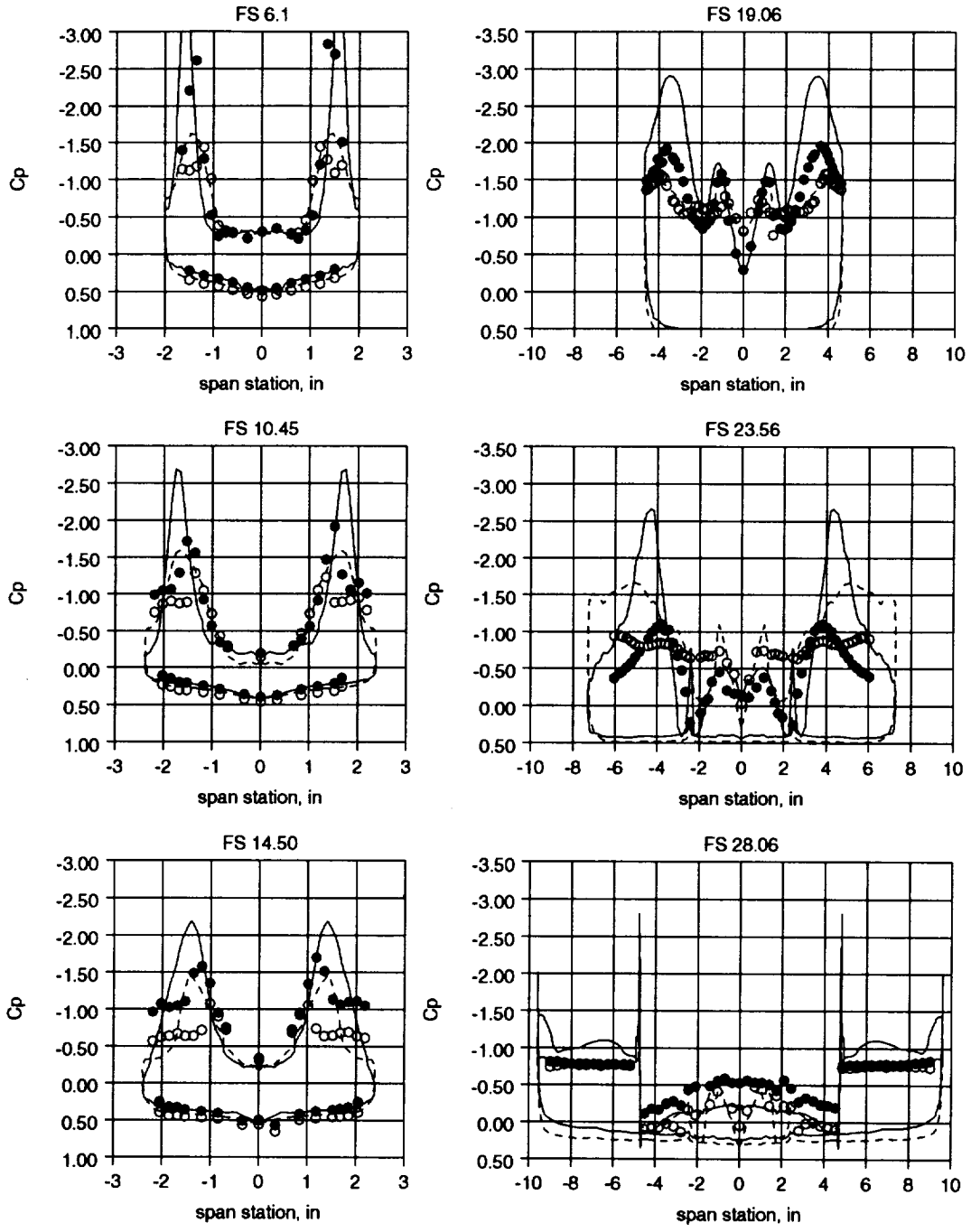
Figure 4.18 Surface pressure comparison to test data for symmetric twin tail configuration at 30 degrees angle-of-attack.
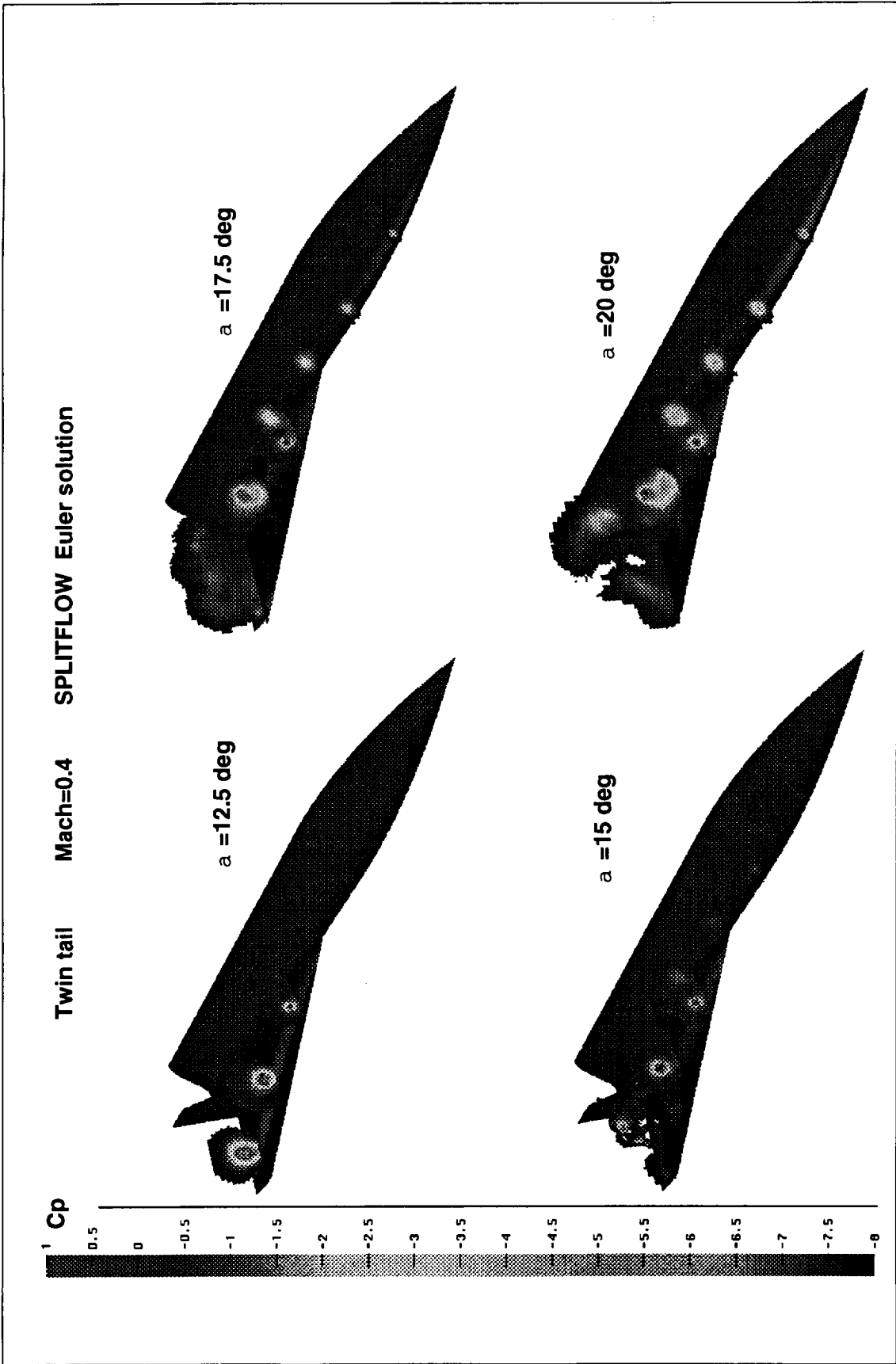
Figure 4.19 Effect of angle-of-attack on pressure coefficient.
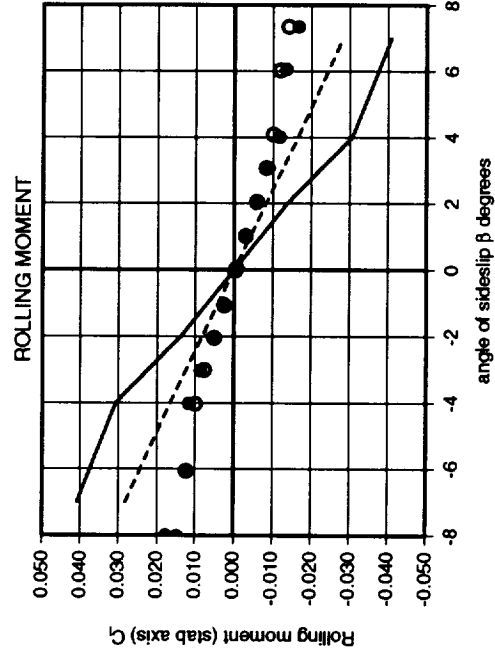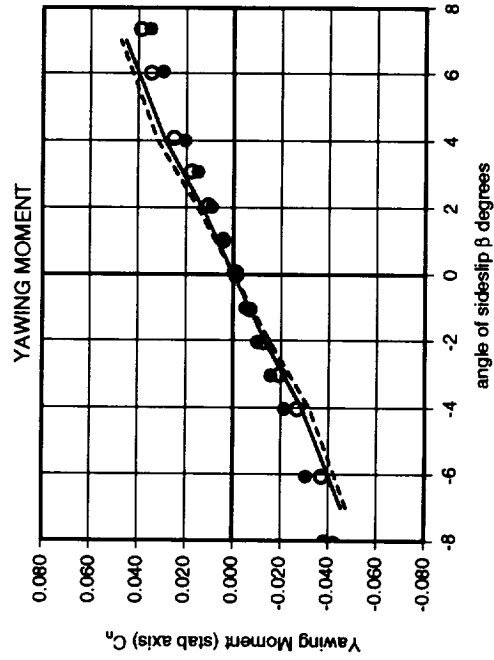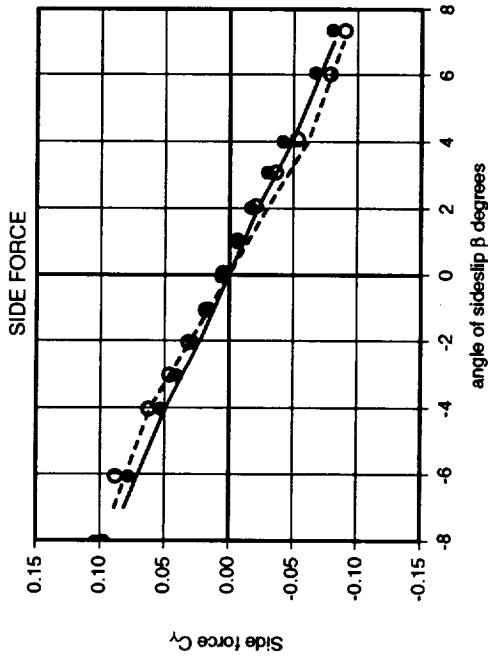
Figure 4.20 Compressibility effects on lateral directional forces/moments for centerline tail, stability axes, angle-of-attack=15.
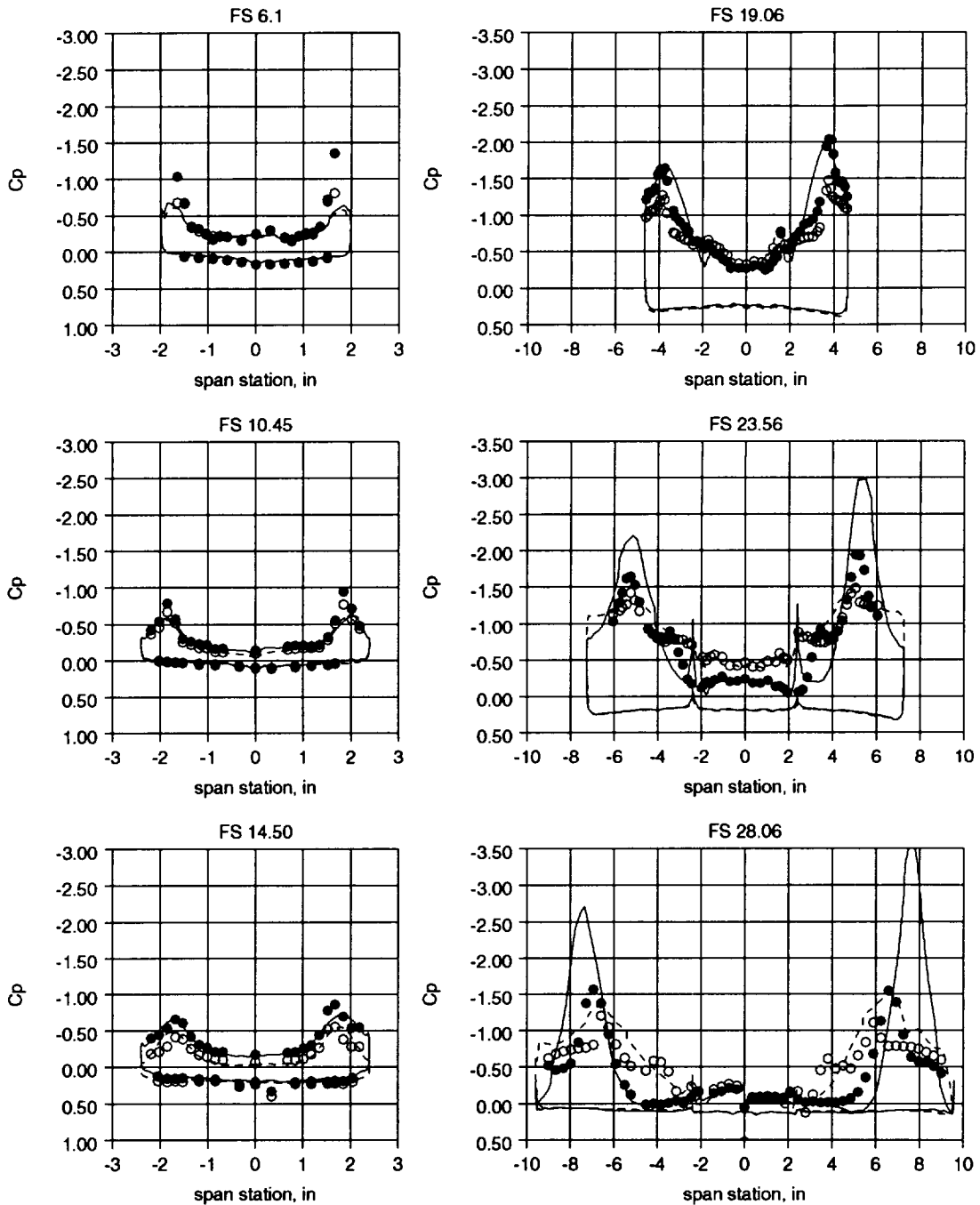
Figure 4.21 Surface pressure comparison to test data for centerline tail configuration at 15 degrees angle-of-attack, 2 degrees angle-of-sideslip.

55

Figure 4.22 Surface pressure comparison to test data for centerline tail configuration at 15 degrees angle-of-attack, 7 degrees angle-of-sideslip.
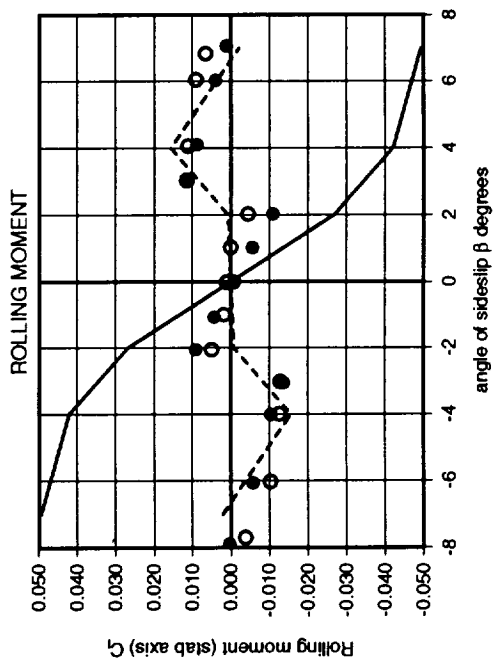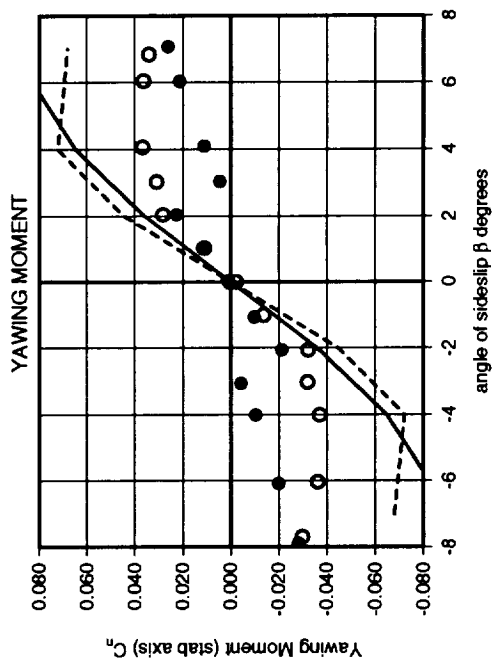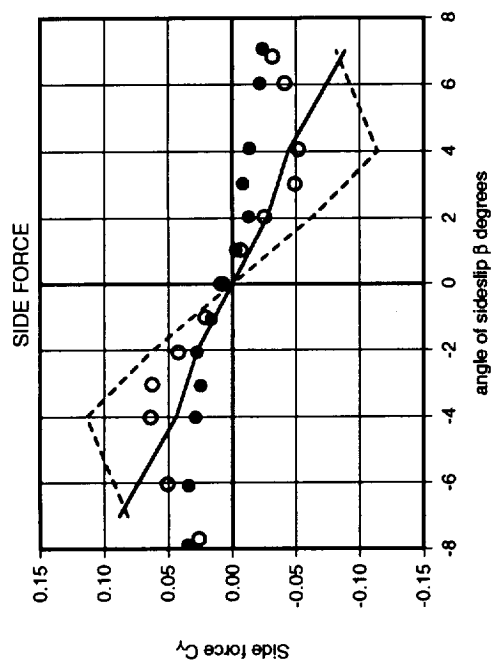
Figure 4.23 Compressibility effects on lateral directional forces/moments for centerline tail, stability axes, angle-of-attack=25.
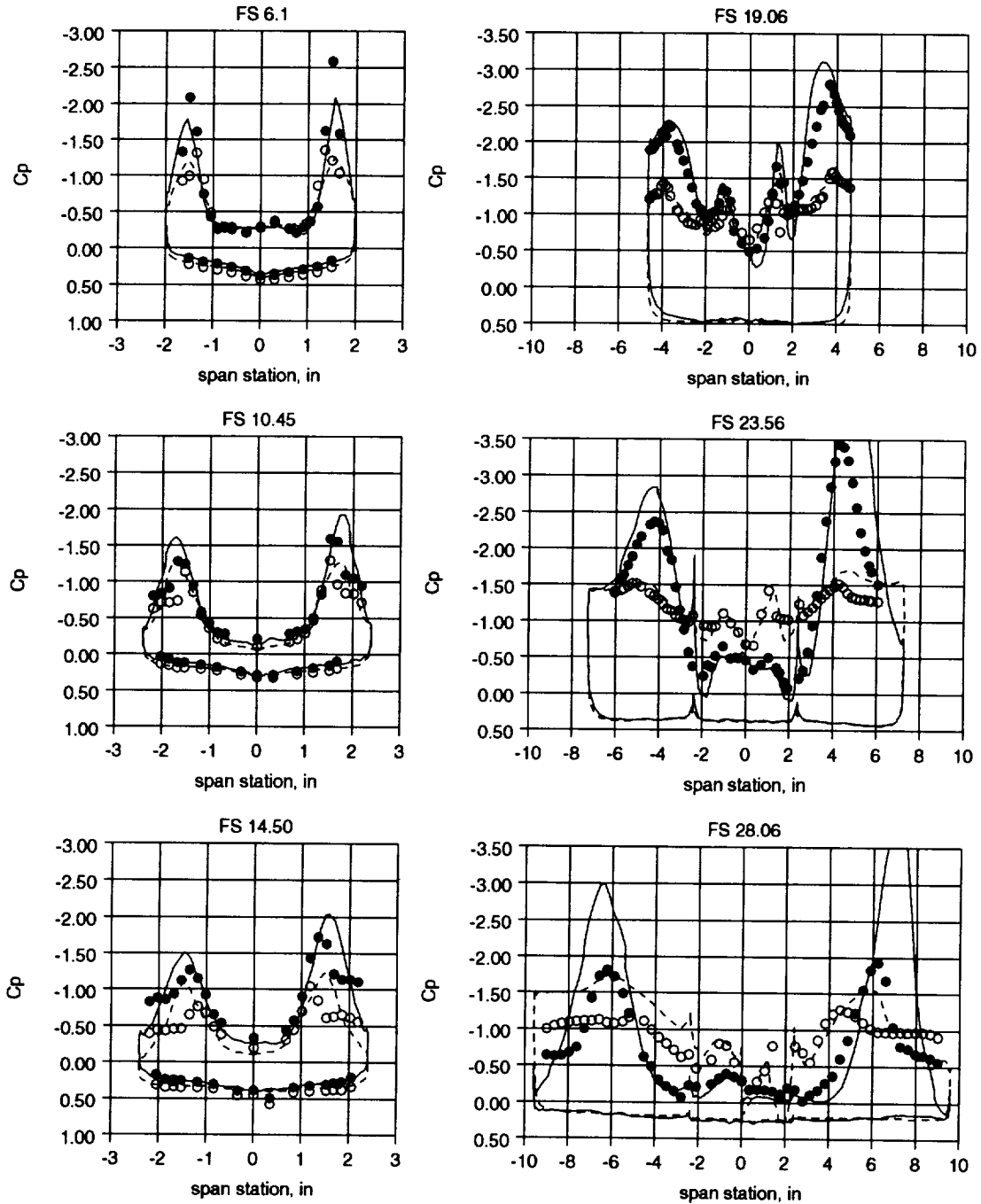
Figure 4.24 Surface pressure comparison to test data for centerline tail configuration at 25 degrees angle-of-attack, 2 degrees angle-of-sideslip.

58
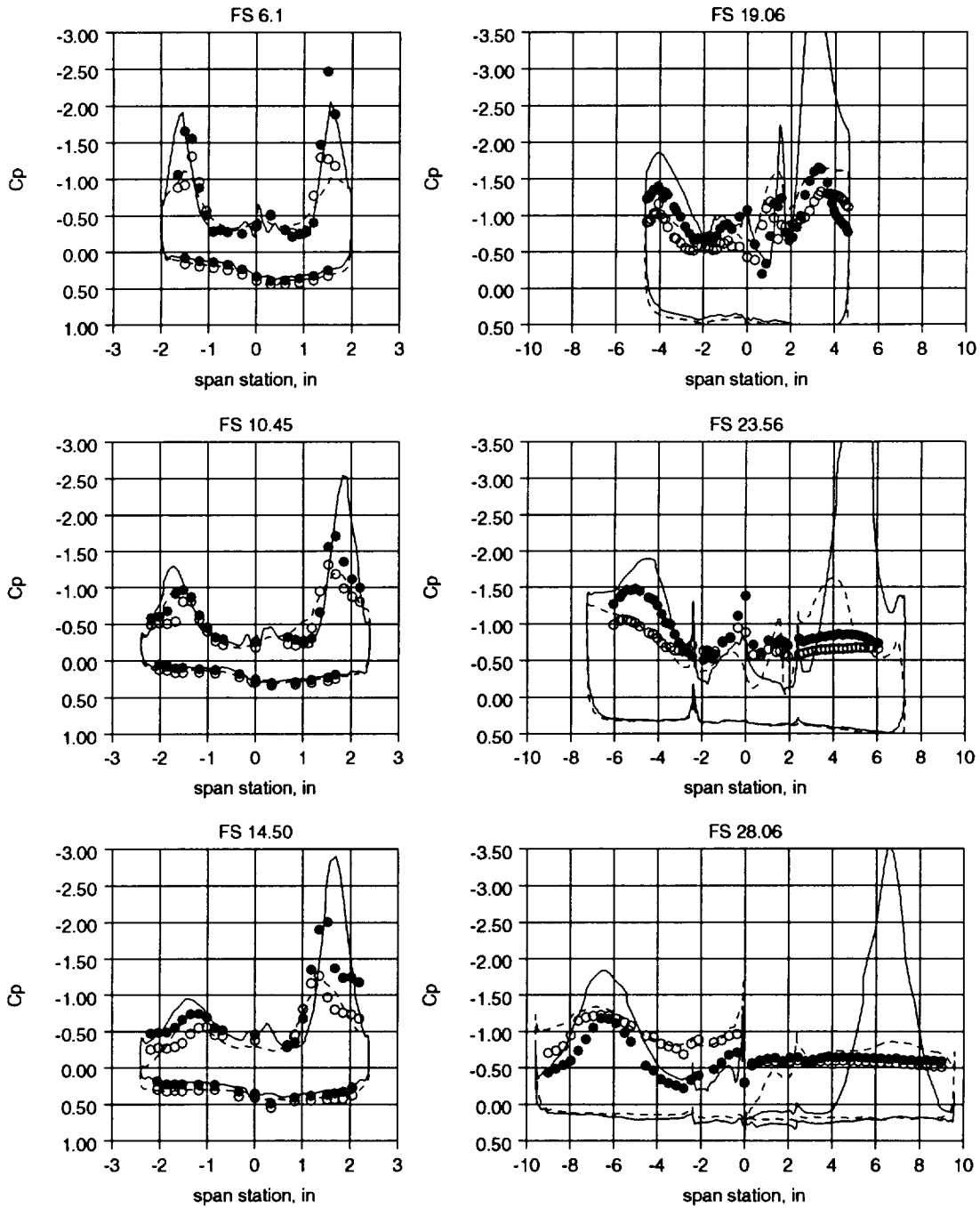
Figure 4.25 Surface pressure comparison to test data for centerline tail configuration at 25 degrees angle-of-attack, 7 degrees angle-of-sideslip.

59

Surface pressure in +Y direction.

Mach 0.4

β = 7 degrees

α = 25 degrees

Data range: -Cp * ny = -1.5 to 1.5
Black is low value. White is high value.

Leeward side

Windward side

Forebody suction is major contributor to side force
and yawing moment.
Much larger suction force on windward side.
Very little contribution from vertical tail.
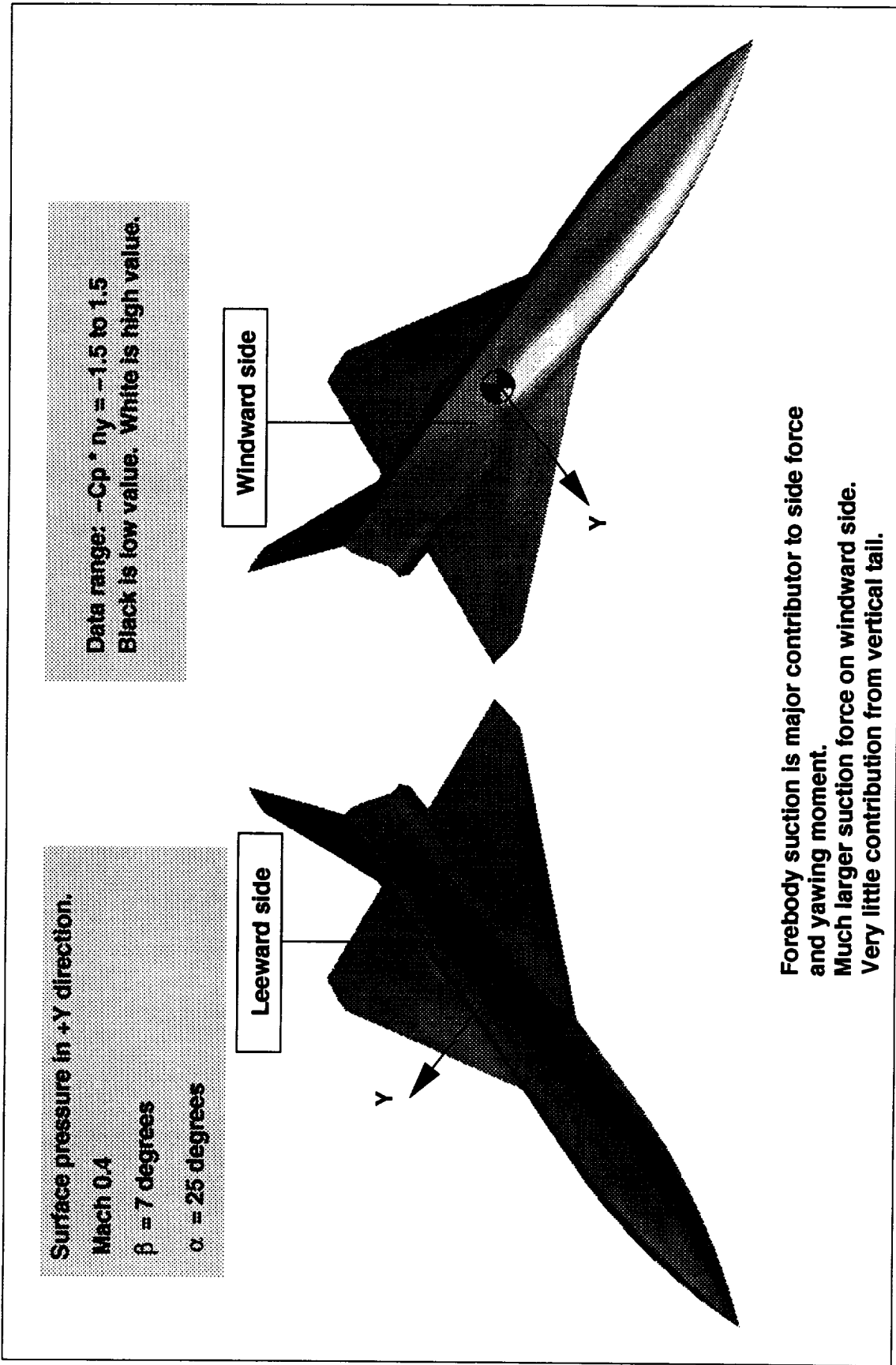
Figure 4.26 Graphic depiction of pressure loads contributing to side force and yawing moment for centerline tail solution.
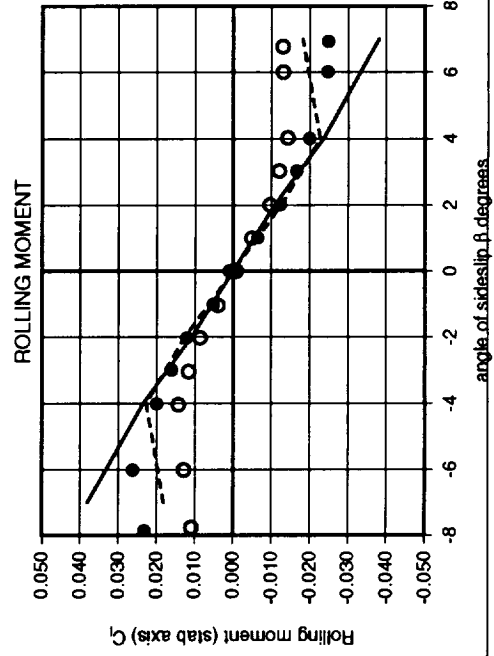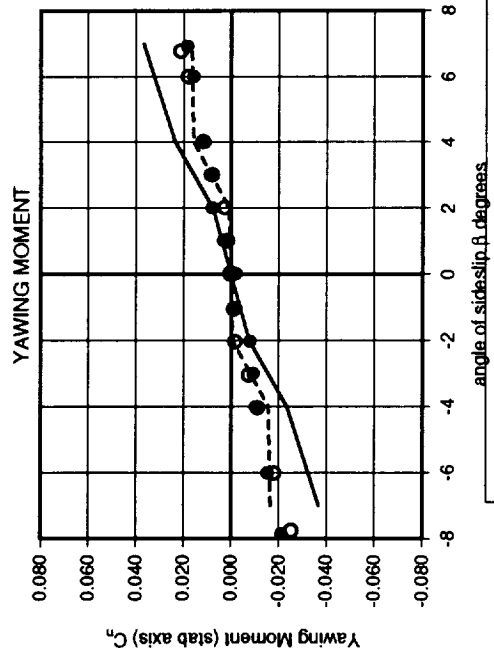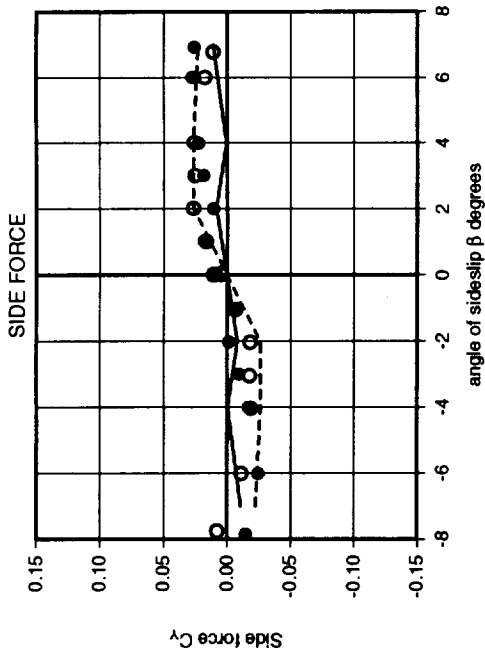
Figure 4.27 Compressibility effects on lateral directional forces/moments for twin tail, stability axes, angle-of-attack=25.
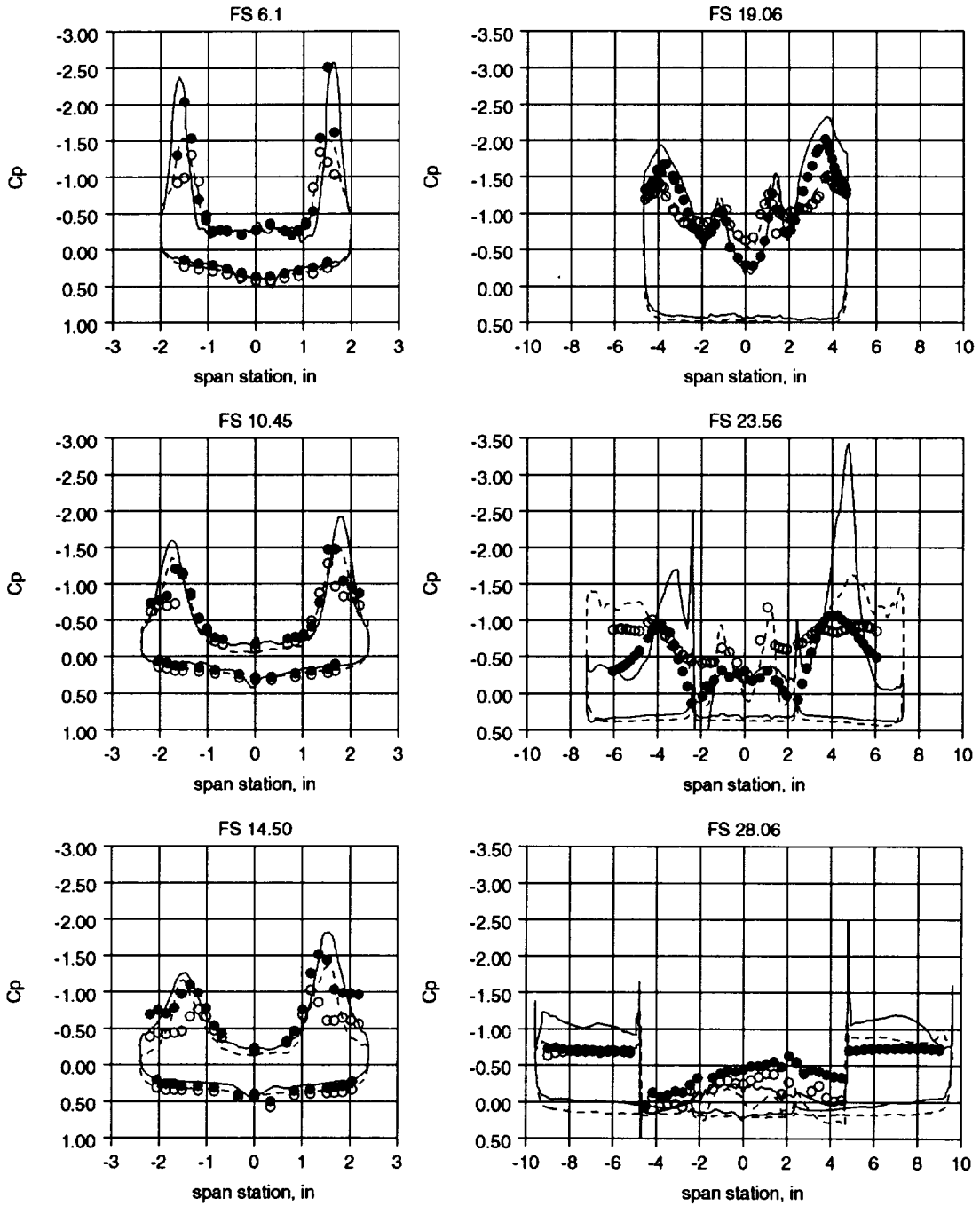
Figure 4.28 Surface pressure comparison to test data for twin tail configuration at 25 degrees angle-of-attack, 2 degrees angle-of-sideslip.
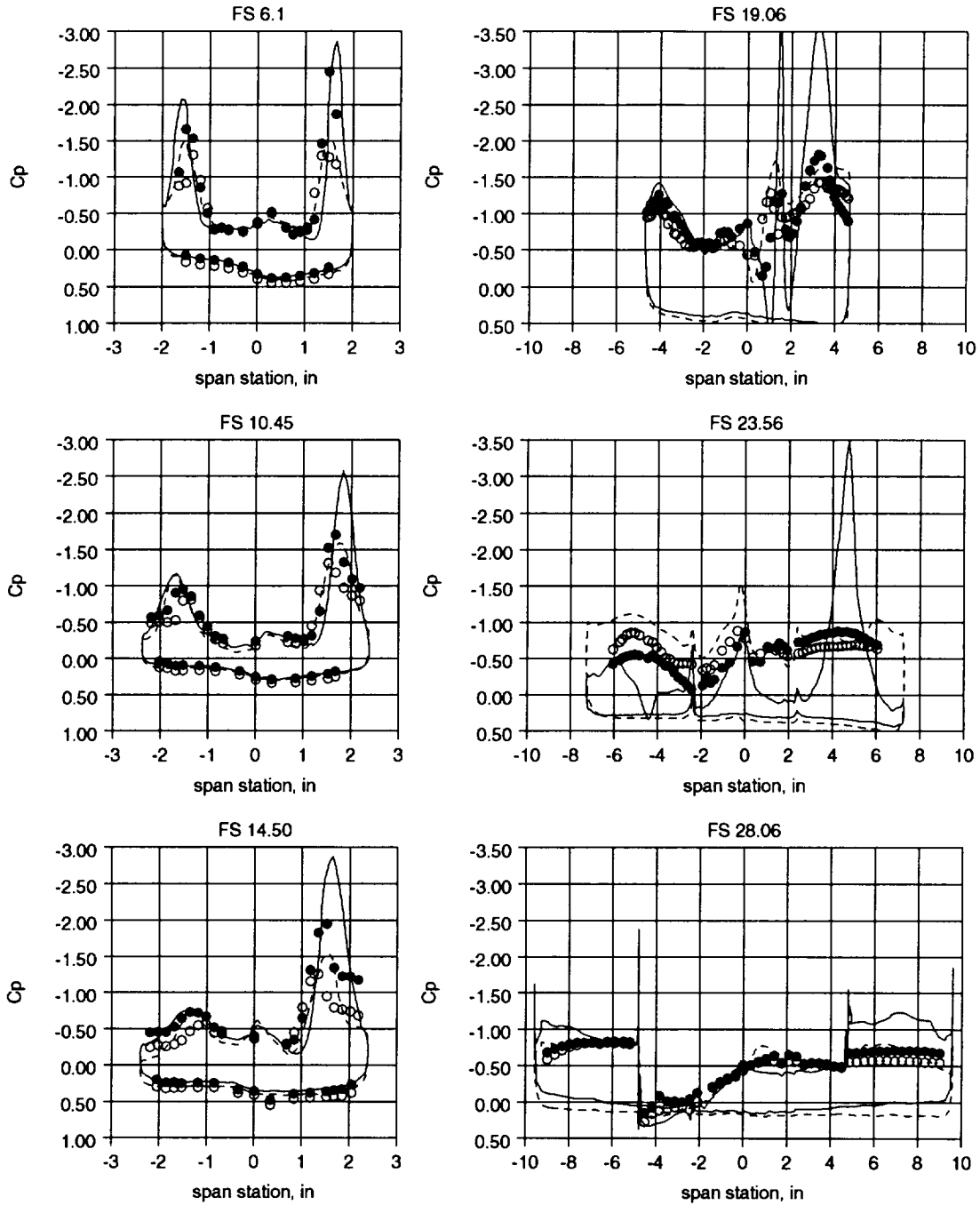
Figure 4.29 Surface pressure comparison to test data for twin tail configuration at 25 degrees angle-of-attack, 7 degrees angle-of-sideslipangle-of-sideslip.

63

Surface pressure in +Y direction.

Mach 0.4

β = 7 degrees

α = 25 degrees

Leeward side

Windward side

Data range: –Cp * hy = –1.5 to 1.5.
Black is low value. White is high value.

Forebody suction is large contributor to side force and yawing moment.
Much larger suction force on windward side.
Significant contributions from vertical tails offset force due to forebody suction.

Figure 4.30 Graphic depiction of pressure loads contributing to side force and yawing moment for twin tail solution.

Local Mach contours

α = 20 degrees

Mach = 0.85

SPLITFLOW inviscid solution
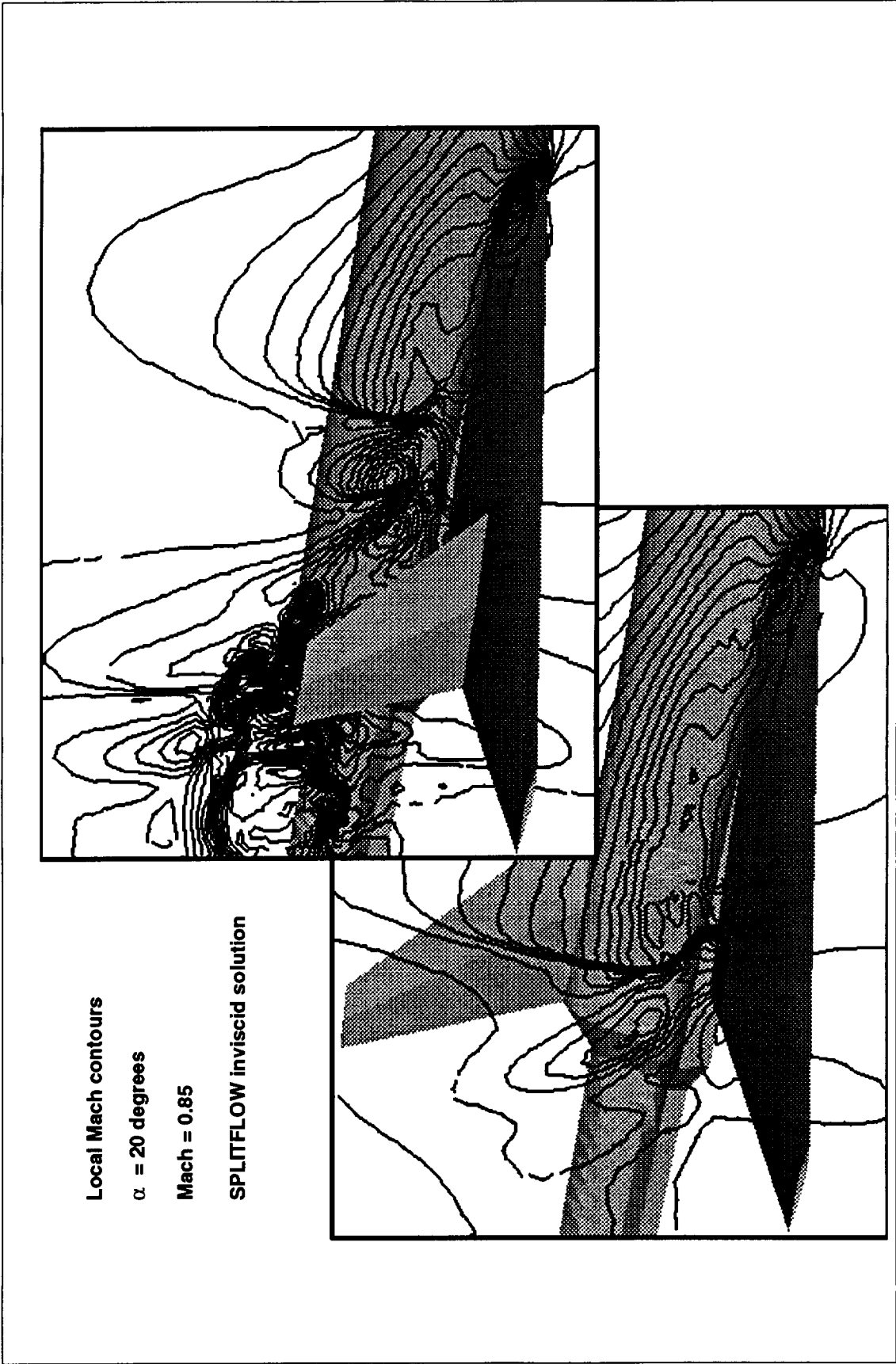
Figure 4.31 Comparison of local Mach contours at span station 3.5 for Mach 0.85, angle-of-attack= 20 degrees.

Local Mach contours

α = 25 degrees

Mach = 0.85

SPLITFLOW inviscid solution
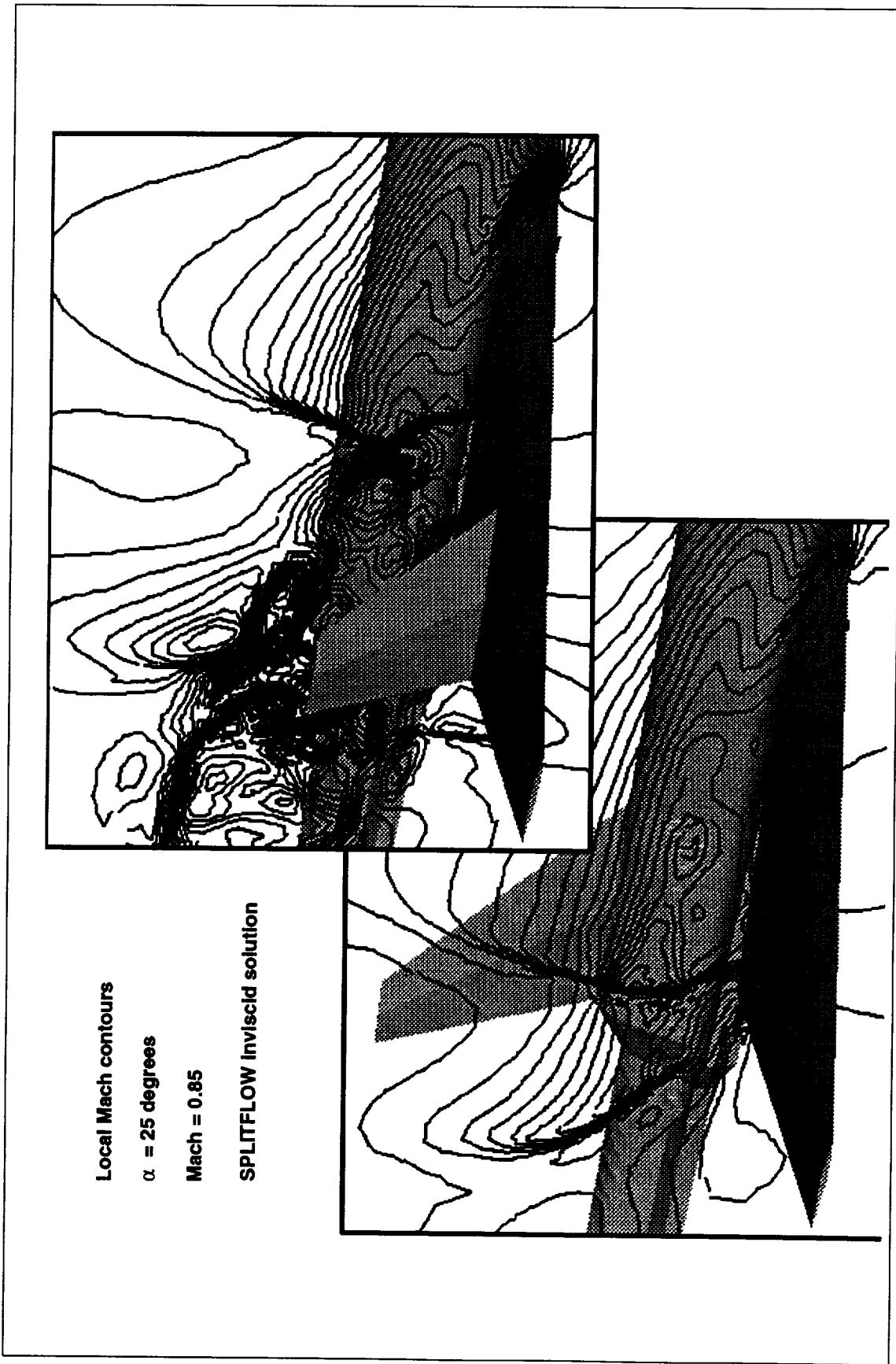
Figure 4.32 Comparison of local Mach contours at span station 3.5 for Mach 0.85, angle-of-attack= 25 degrees.

Local Mach contours

α = 30 degrees

Mach = 0.85

SPLITFLOW inviscid solution
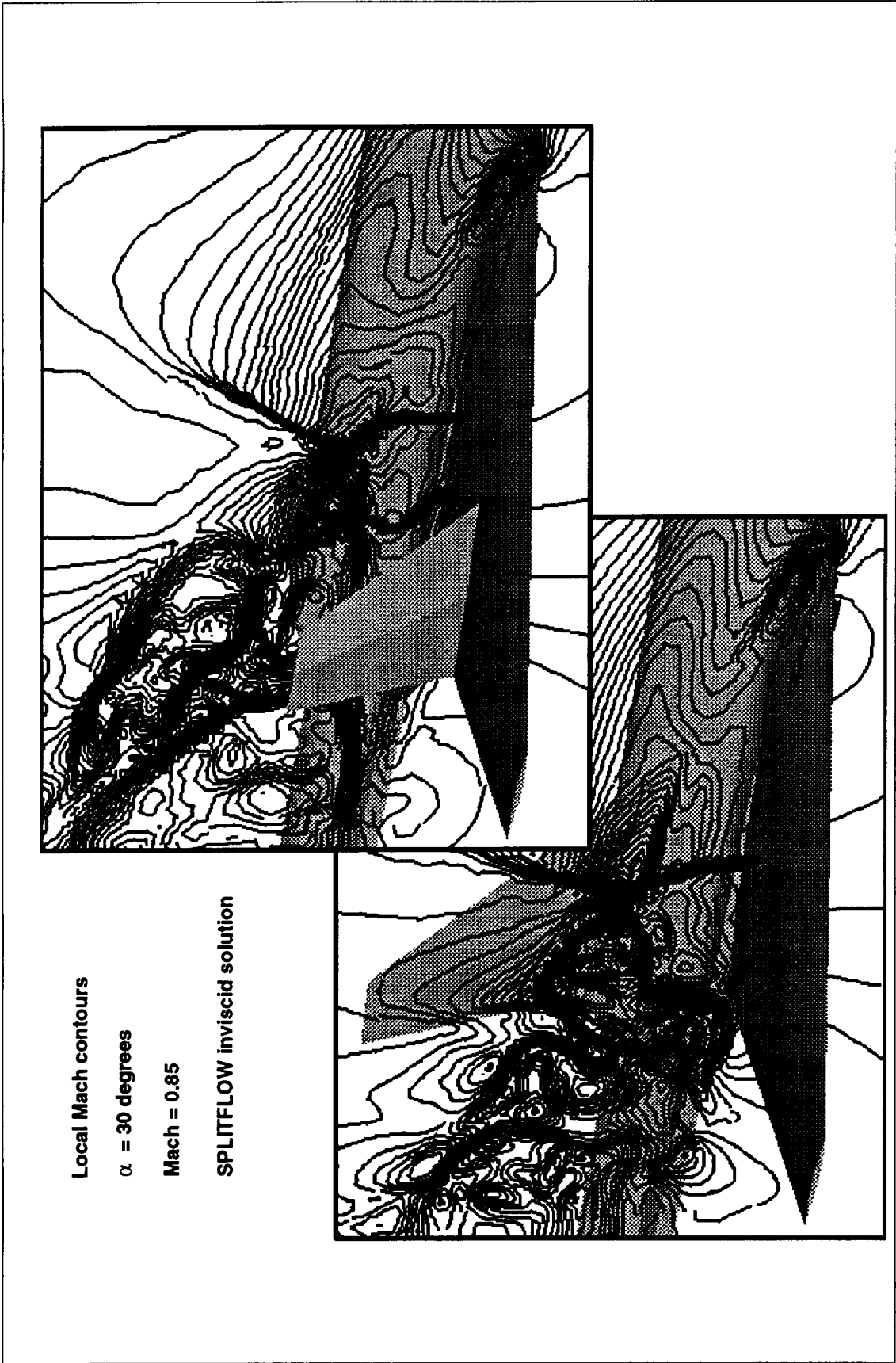
Figure 4.33 Comparison of local Mach contours at span station 3.5 for Mach 0.85, angle-of-attack= 30 degrees.

Pressure coefficient

α = 25 degrees

Mach = 0.85

SPLITFLOW inviscid solution
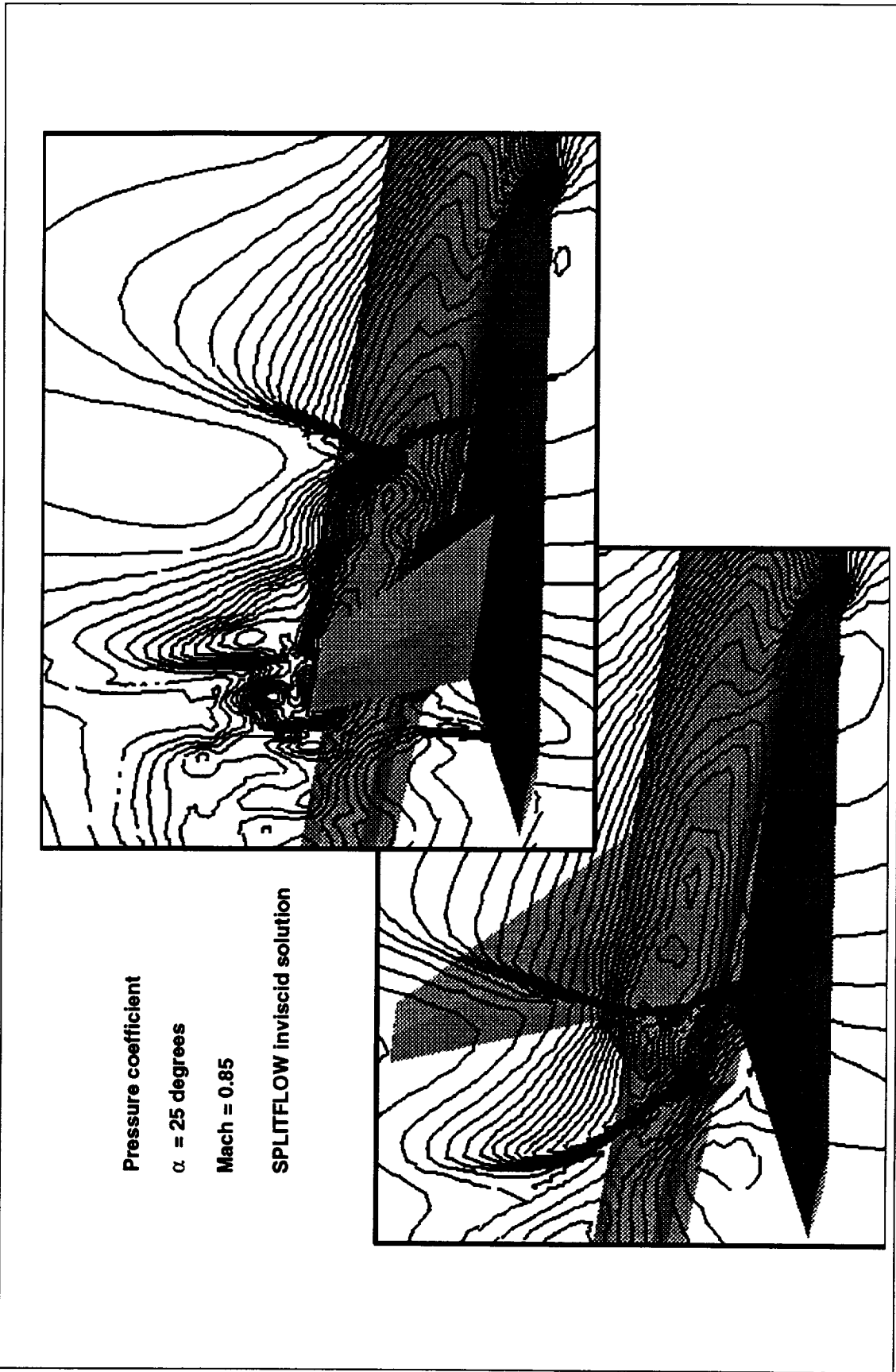
Figure 4.34 Comparison of local pressure contours at span station 3.5 for Mach 0.85, angle-of-attack= 25 degrees.

Crossflow Mach contours

α = 25 degrees

Mach = 0.85

SPLITFLOW inviscid solution

Crossflow Shocks
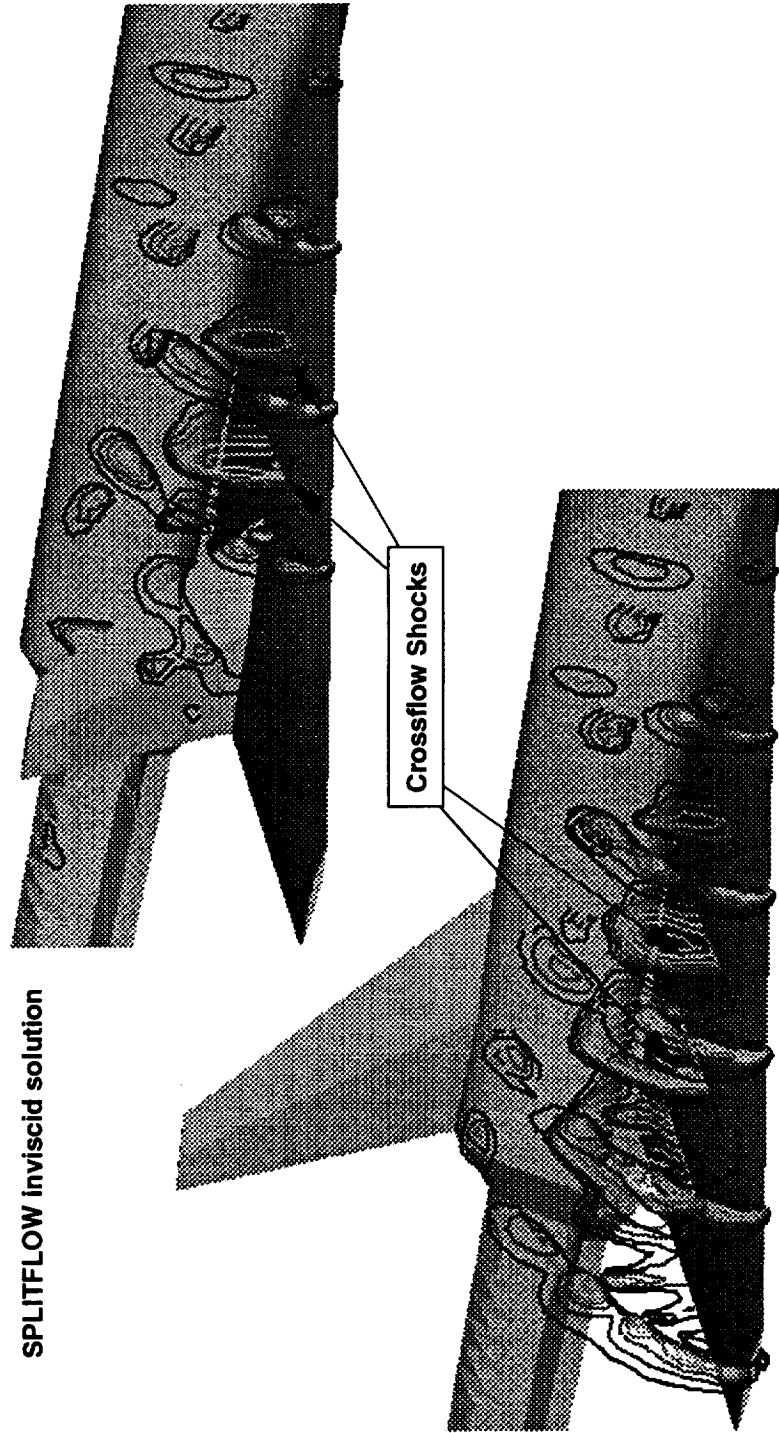
Figure 4.35 Comparison of crossflow Mach contours are selected axial stations for Mach 0.85, angle-of-attack= 25 degrees.

69
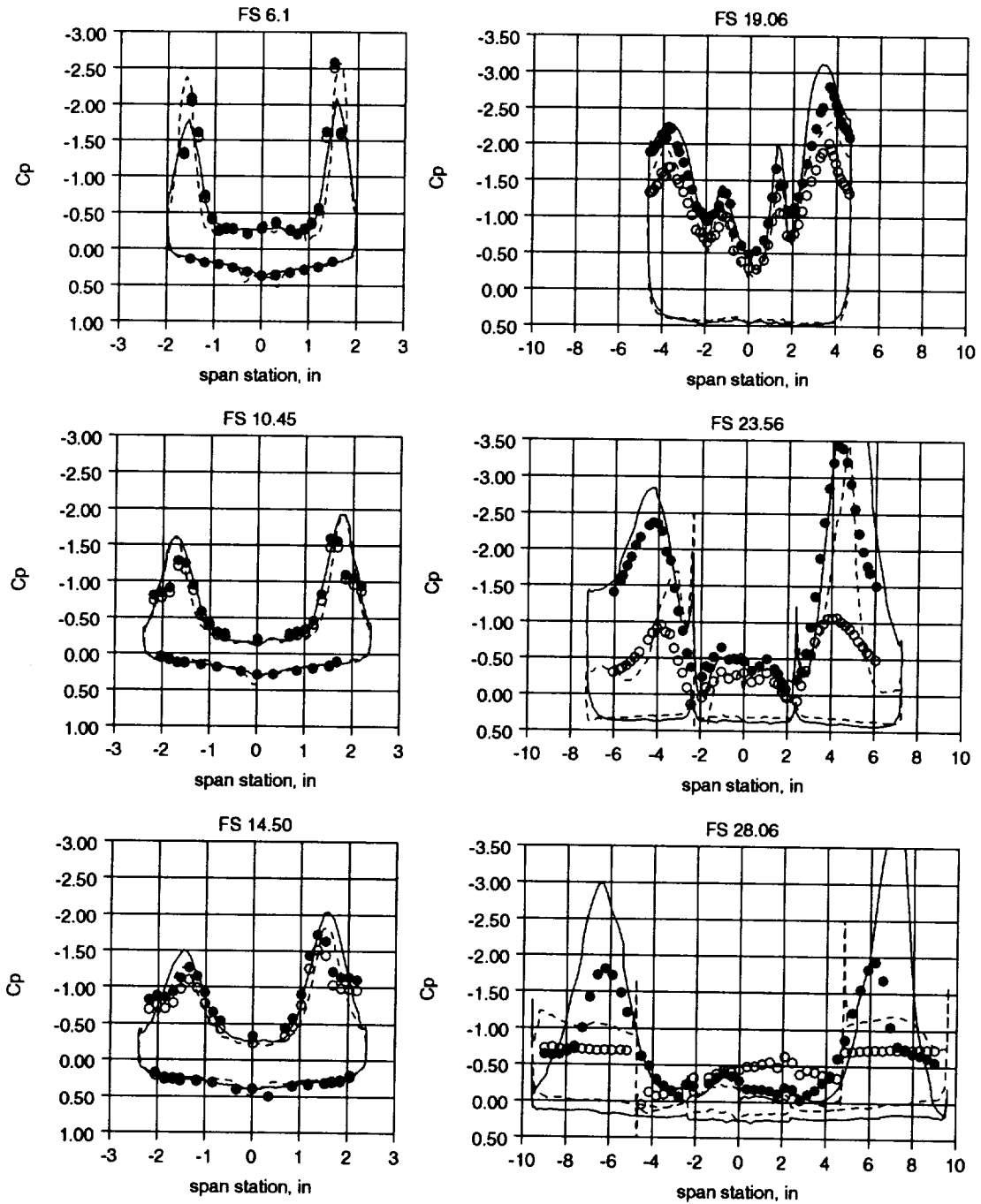
Figure 4.36 Surface pressure comparison to test data for Mach 0.4 at 25 degrees angle-of-attack, 2 degrees angle-of-sideslip.
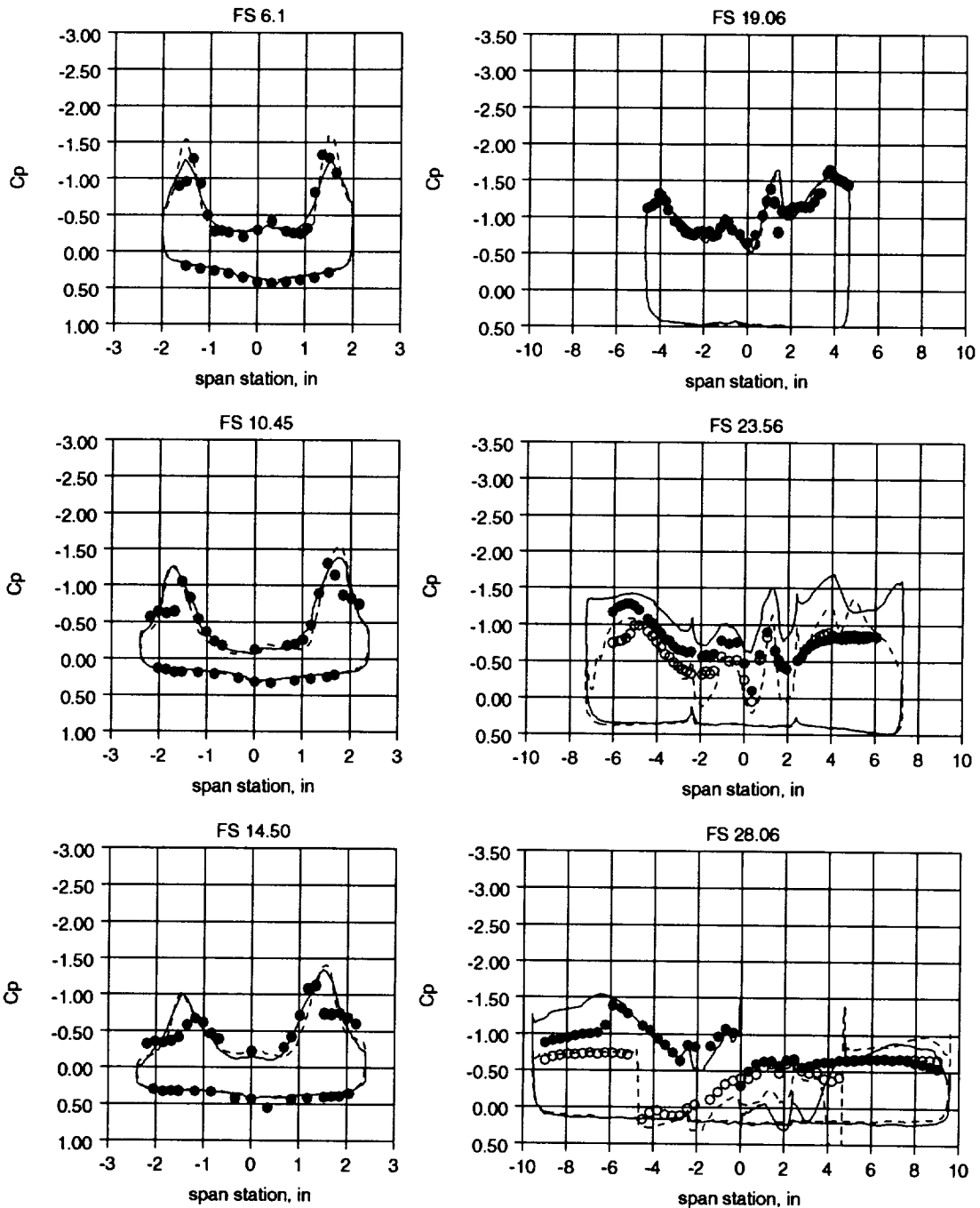
70
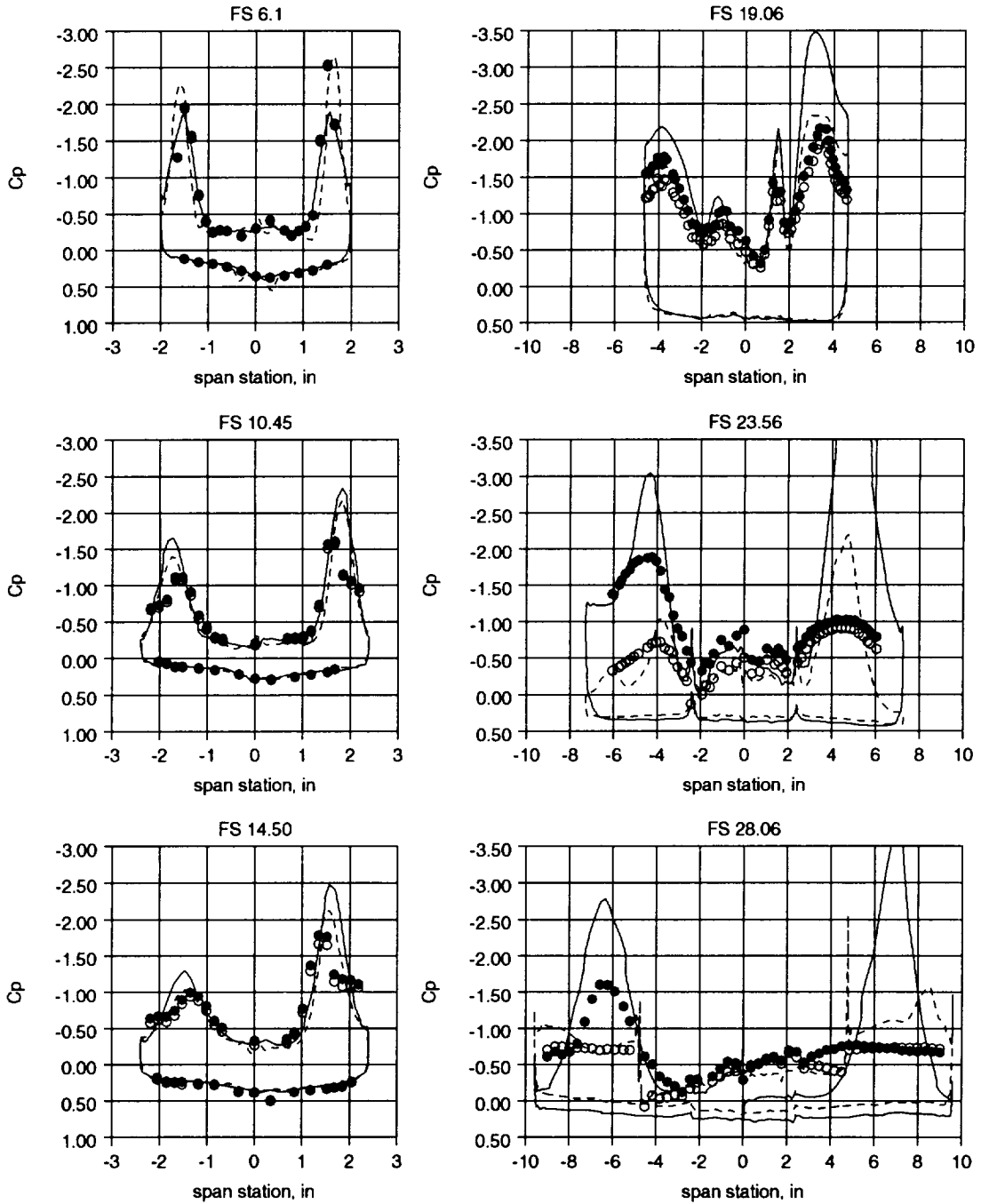
Figure 4.37 Surface pressure comparison to test data for Mach 0.4 at 25 degrees angle-of-attack, 4 degrees angle-of-sideslip.

71

| SYM	Data	Geometry	Mach	β,α
——	SPLITFLOW	Centerline Tail	Mach=0.40	β=7.0, α=25.0
– – –	SPLITFLOW	Twin Tail	Mach=0.40	β=7.0, α=25.0
●	Test	Centerline Tail	Mach=0.40	β=7.0, α=25.0
○	Test	Twin Tail	Mach=0.40	β=7.0, α=25.0
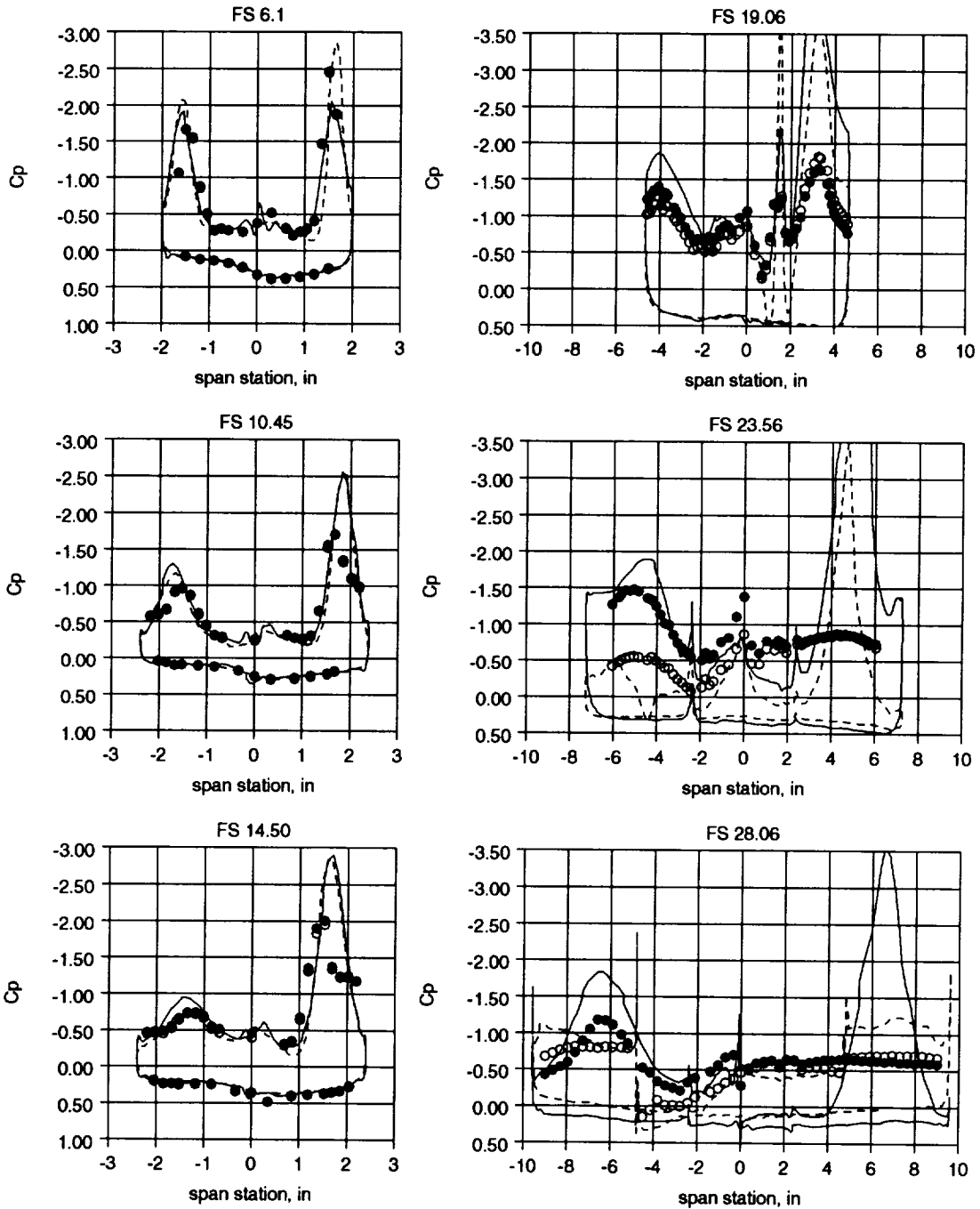
Figure 4.38 Surface pressure comparison to test data for Mach 0.4 at 25 degrees angle-of-attack, 7 degrees angle-of-sideslip.

72

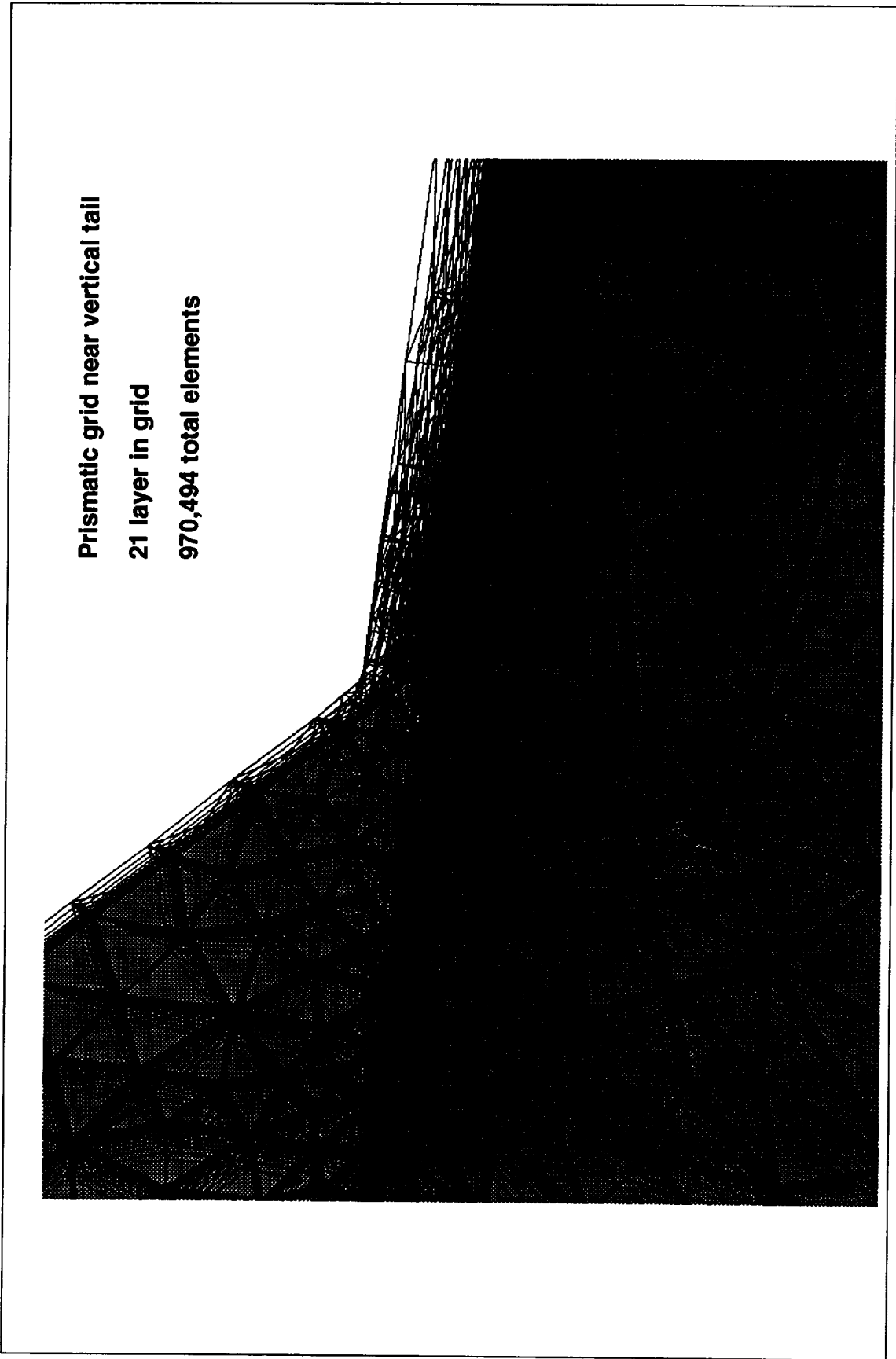| SYM	Data	Geometry	Mach	β,α
——————	SPLITFLOW	Centerline Tail	Mach=0.85	β=2.0, α=25.0
− − − − −	SPLITFLOW	Twin Tail	Mach=0.85	β=2.0, α=25.0
●	Test	Centerline Tail	Mach=0.85	β=2.0, α=25.0
○	Test	Twin Tail	Mach=0.85	β=2.0, α=25.0
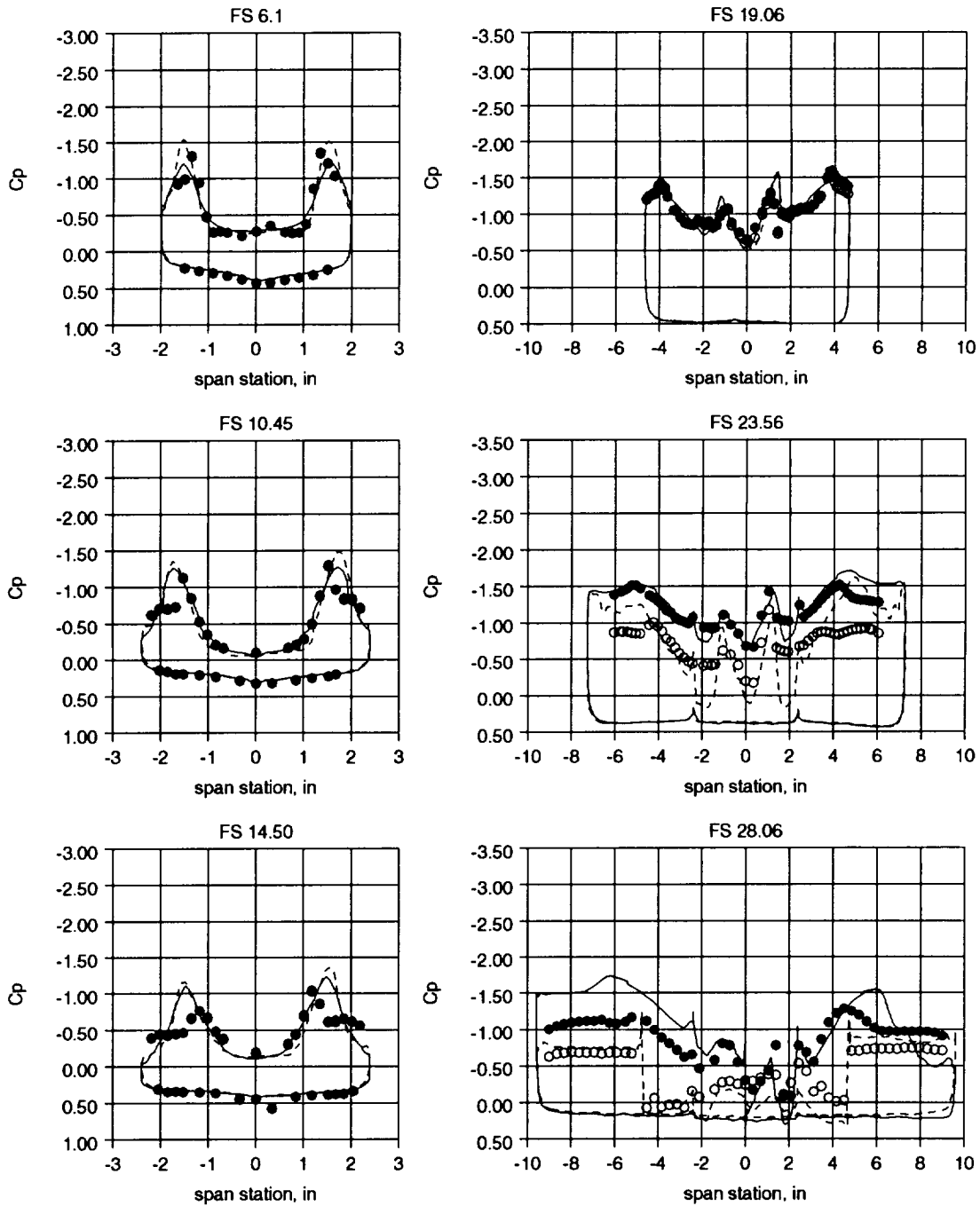
Figure 4.39 Surface pressure comparison to test data for Mach 0.85 at 25 degrees angle-of-attack, 2 degrees angle-of-sideslip.

73

Figure 4.40 Surface pressure comparison to test data for Mach 0.85 at 25 degrees angle-of-attack, 4 degrees angle-of-sideslip.

74

SYM	Data	Geometry	Mach	β,α
————	SPLITFLOW	Centerline Tail	Mach=0.85	β=7.0, α=25.0
– – – – –	SPLITFLOW	Twin Tail	Mach=0.85	β=7.0, α=25.0
●	Test	Centerline Tail	Mach=0.85	β=7.0, α=25.0
○	Test	Twin Tail	Mach=0.85	β=7.0, α=25.0
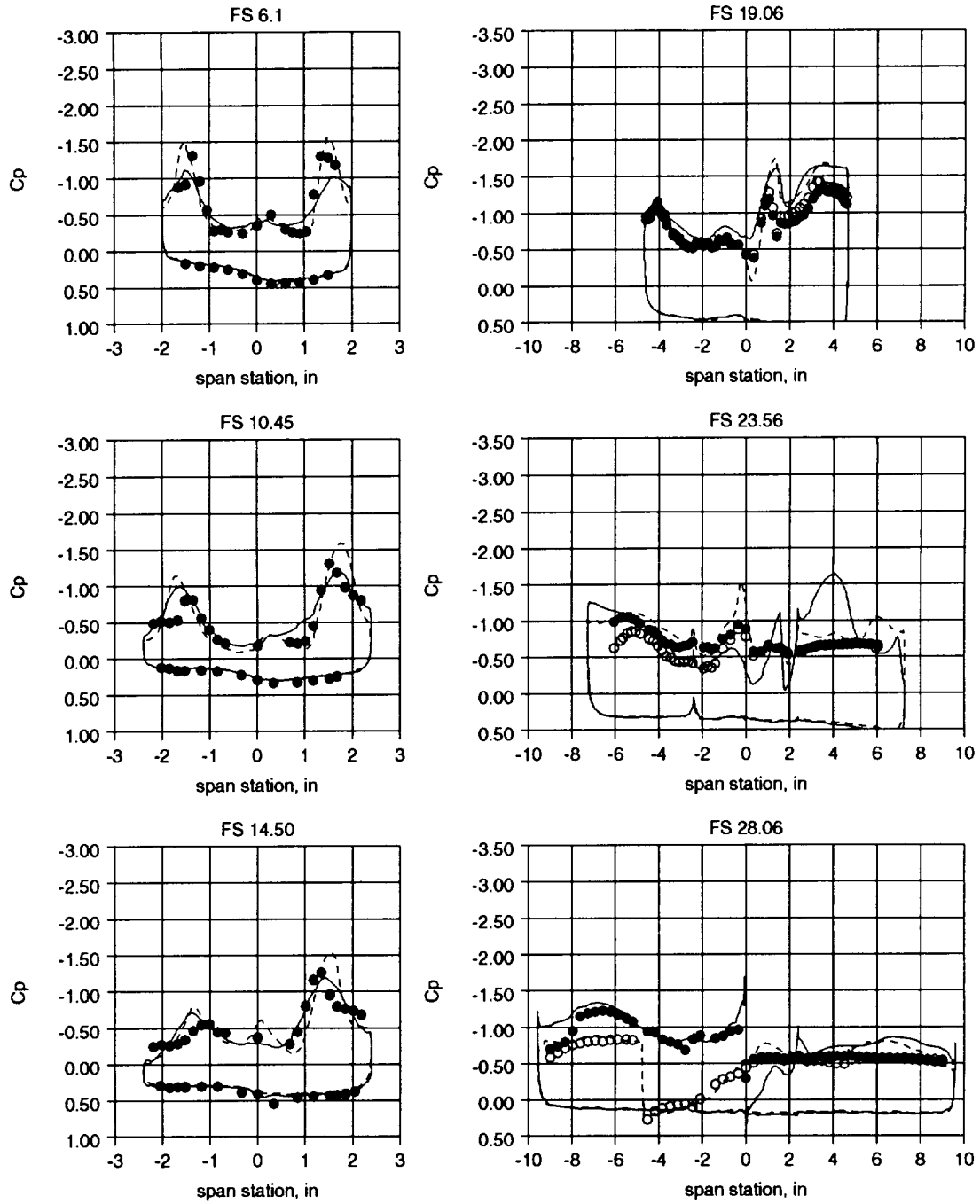
Figure 4.41 Surface pressure comparison to test data for Mach 0.85 at 25 degrees angle-of-attack, 7 degrees angle-of-sideslip.

Prismatic grid near vertical tail

21 layer in grid

970,494 total elements

Figure 5.1 Prismatic grid near vertical tail of centerline tail geometry.
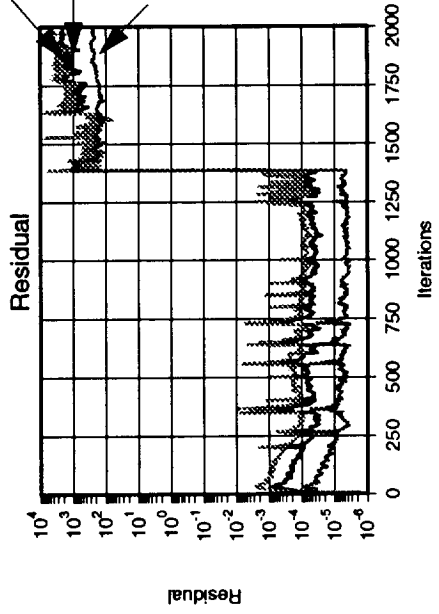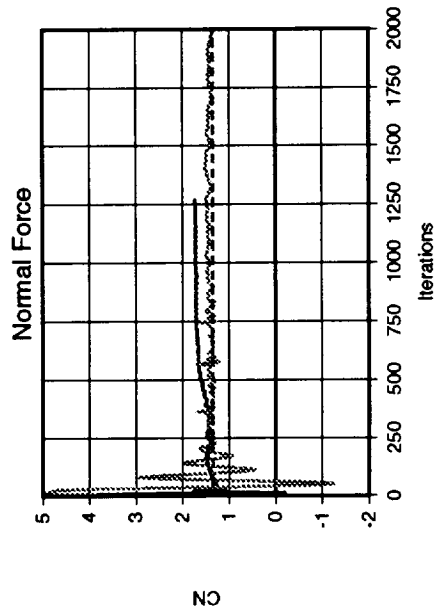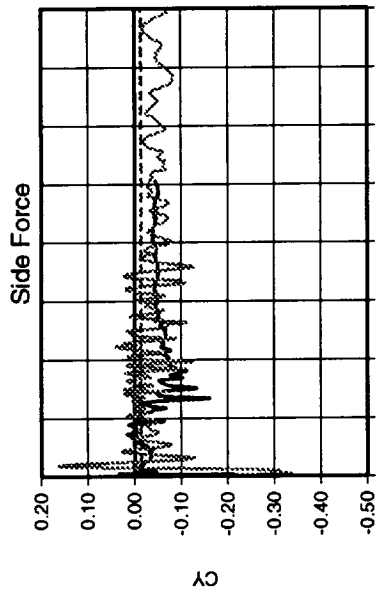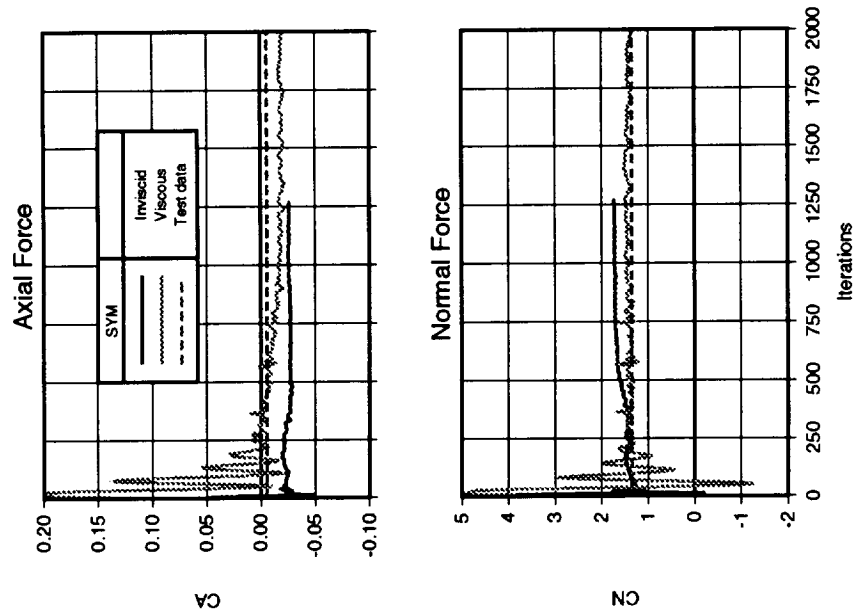
Figure 5.2 Force history comparison between inviscid and viscous solutions.
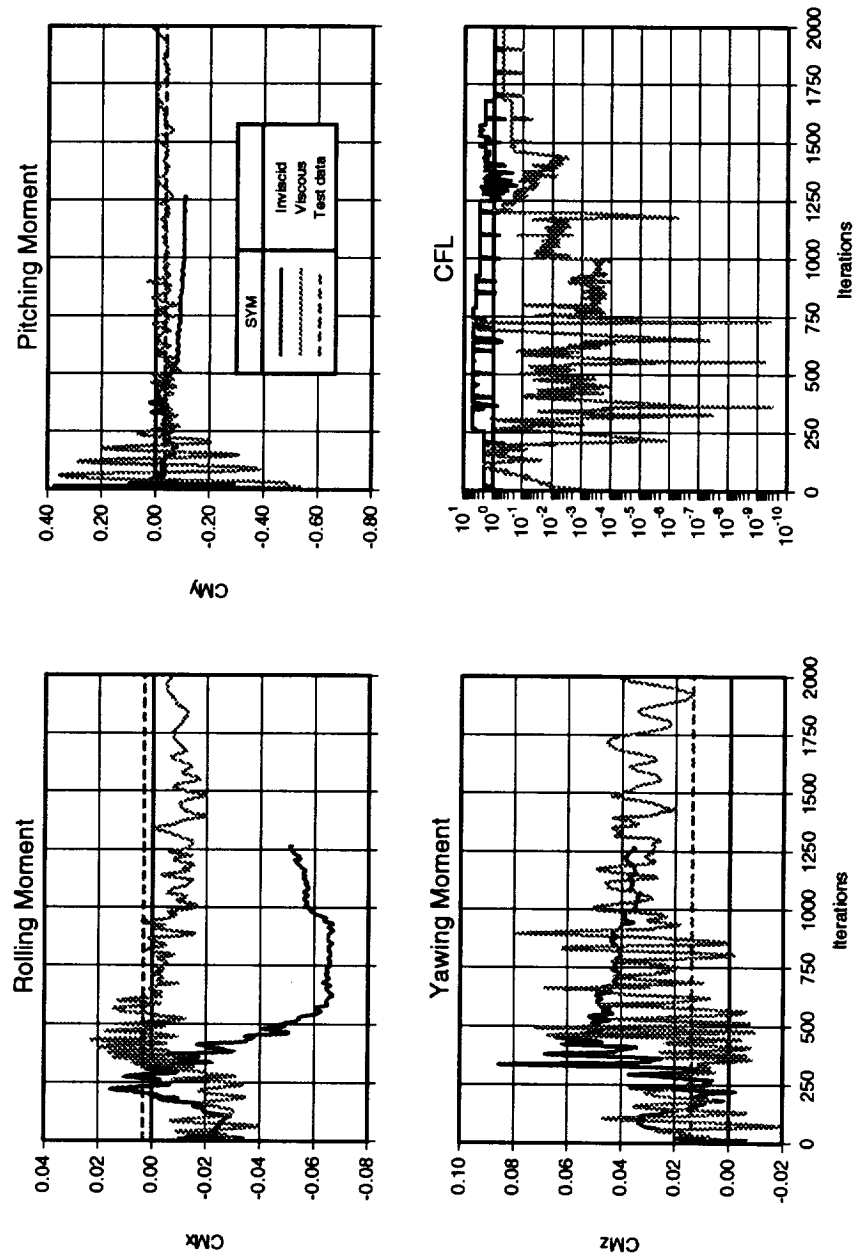
Figure 5.3 Moment history comparison between inviscid and viscous solutions.

SYM	Data	Geometry	Mach	β,α
——	SPLITFLOW	Inviscid	Mach=0.40	β=4.0, α=25.0
- - - -	SPLITFLOW	Viscous	Mach=0.40	β=4.0, α=25.0
●	Test	Test	Mach=0.40	β=4.0, α=25.0
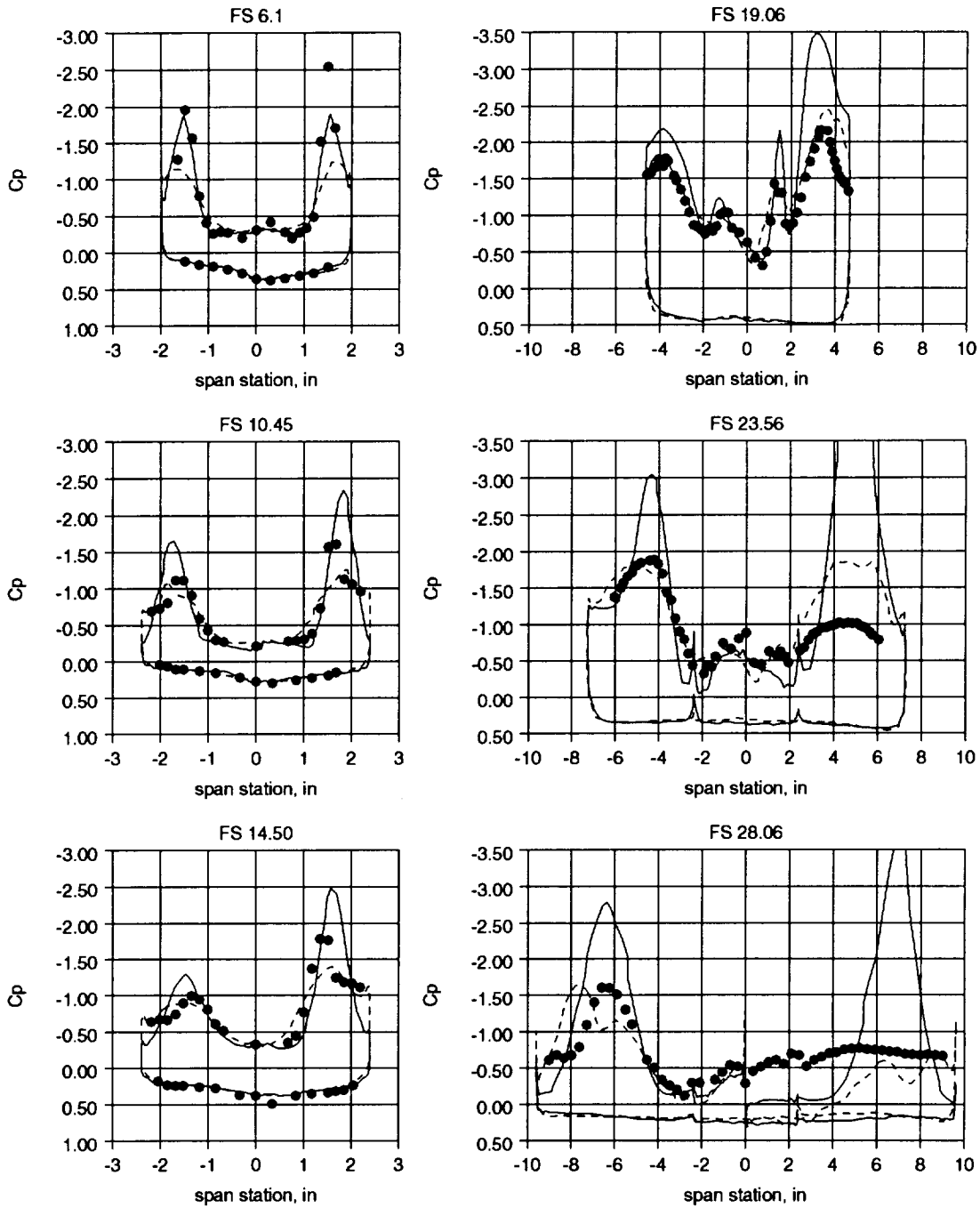
Figure 5.4 Surface pressure comparison between inviscid and viscous solutions for Mach 0.4, 25 degrees angle of attack and 4 degrees angle of sideslip.

79
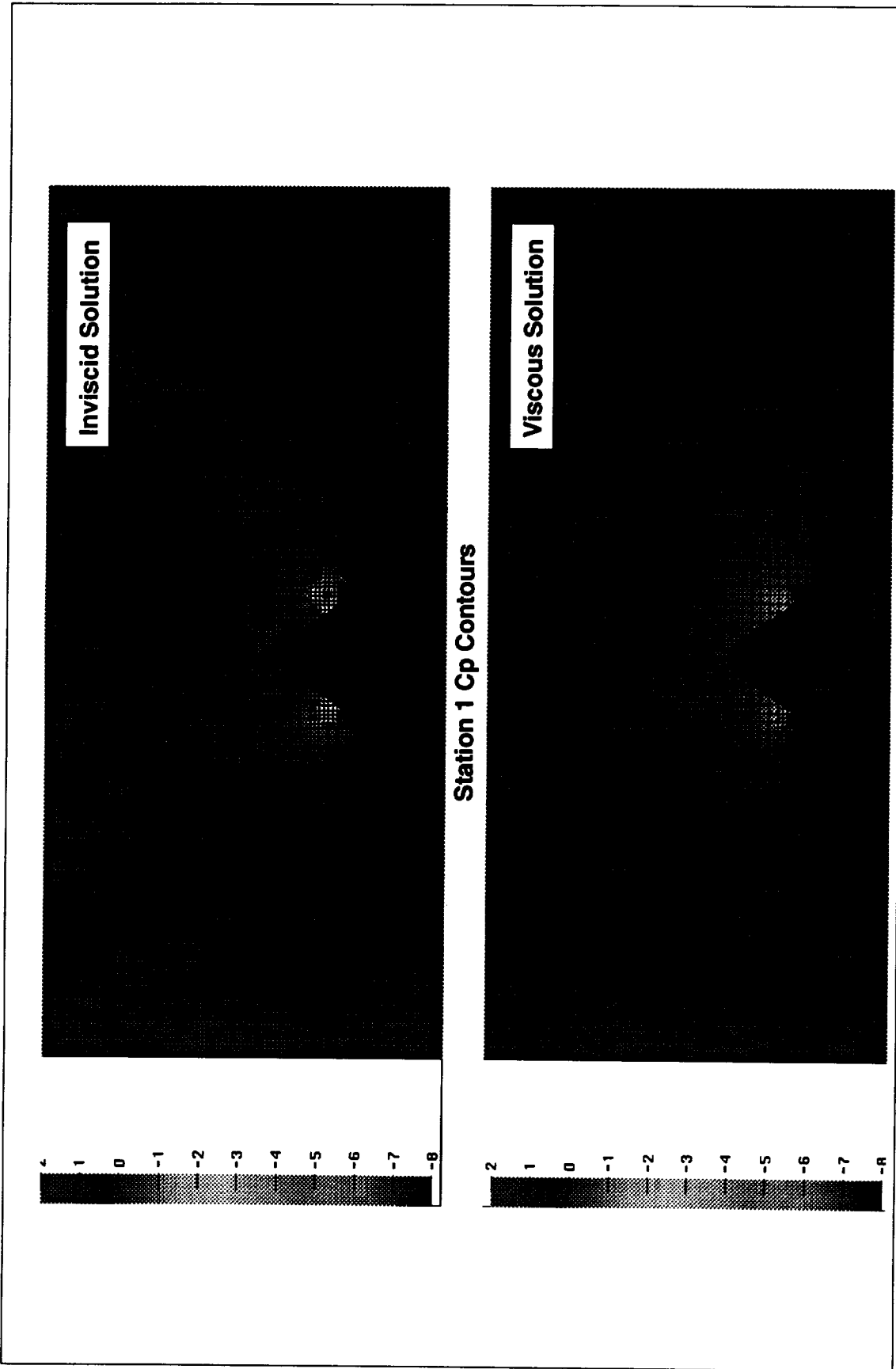
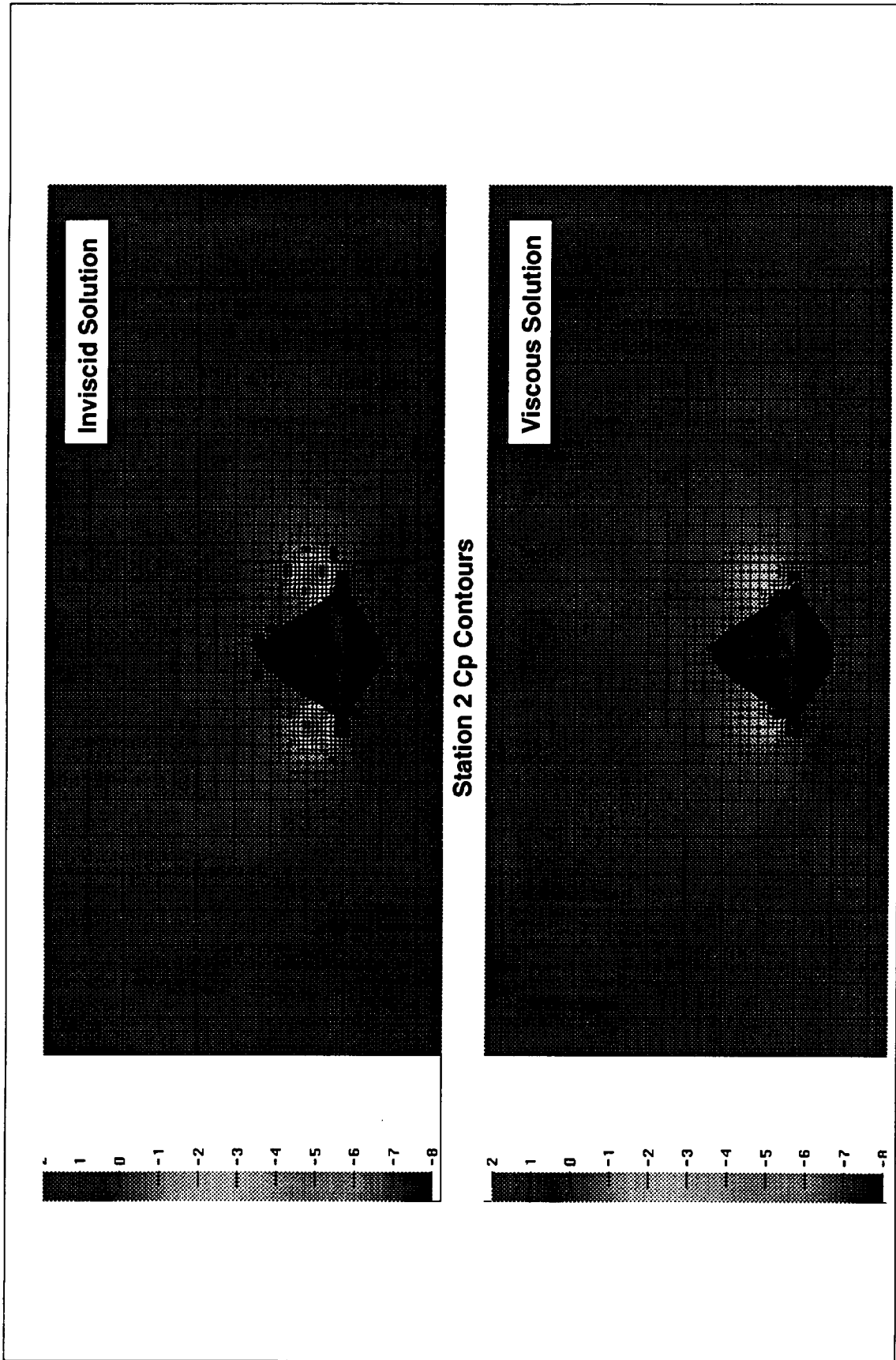Figure 5.5 Comparison of station 1 pressure coefficient contours between inviscid and viscous solutions.

Figure 5.6 Comparison of station 2 pressure coefficient contours between inviscid and viscous solutions.
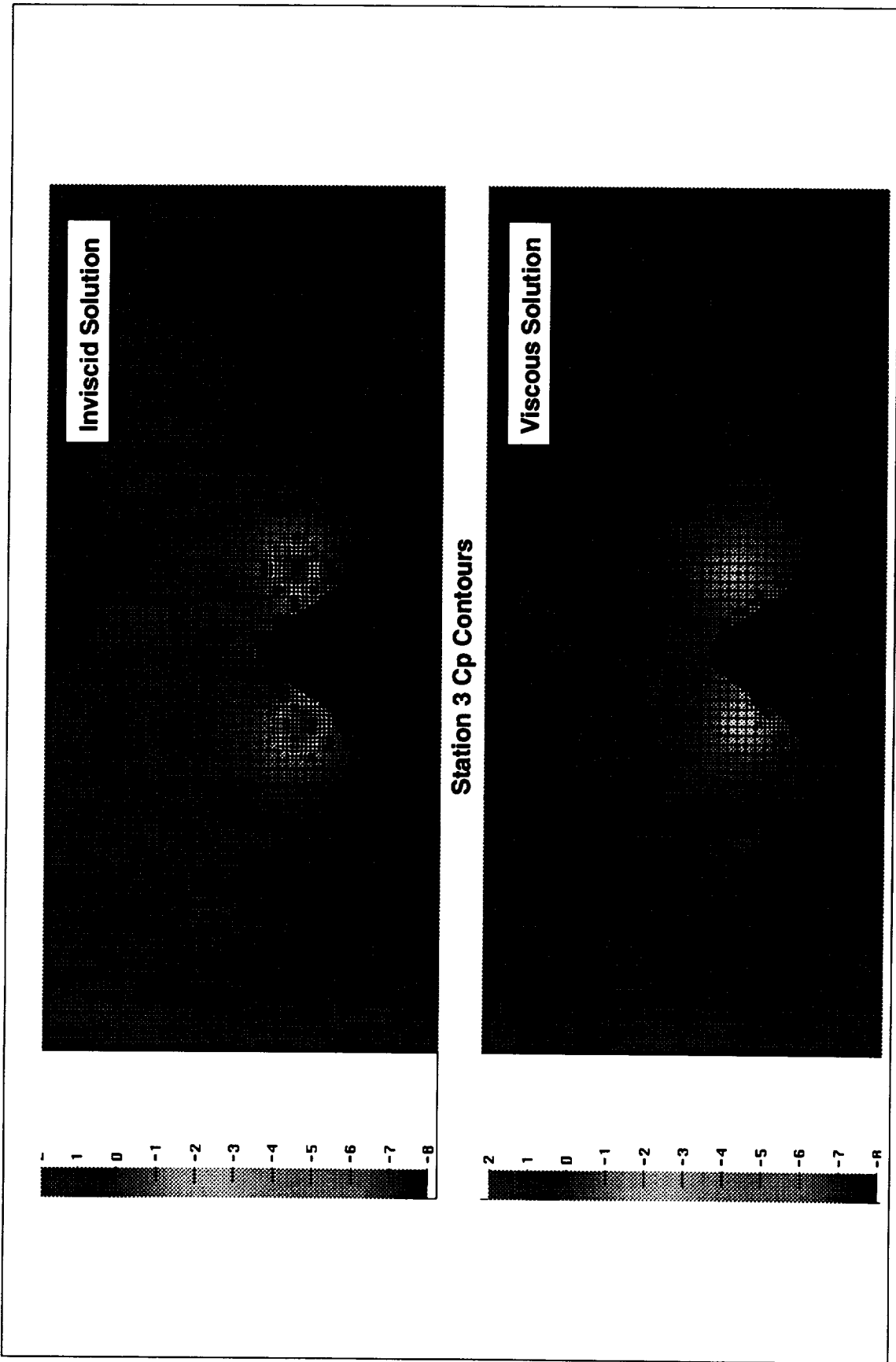
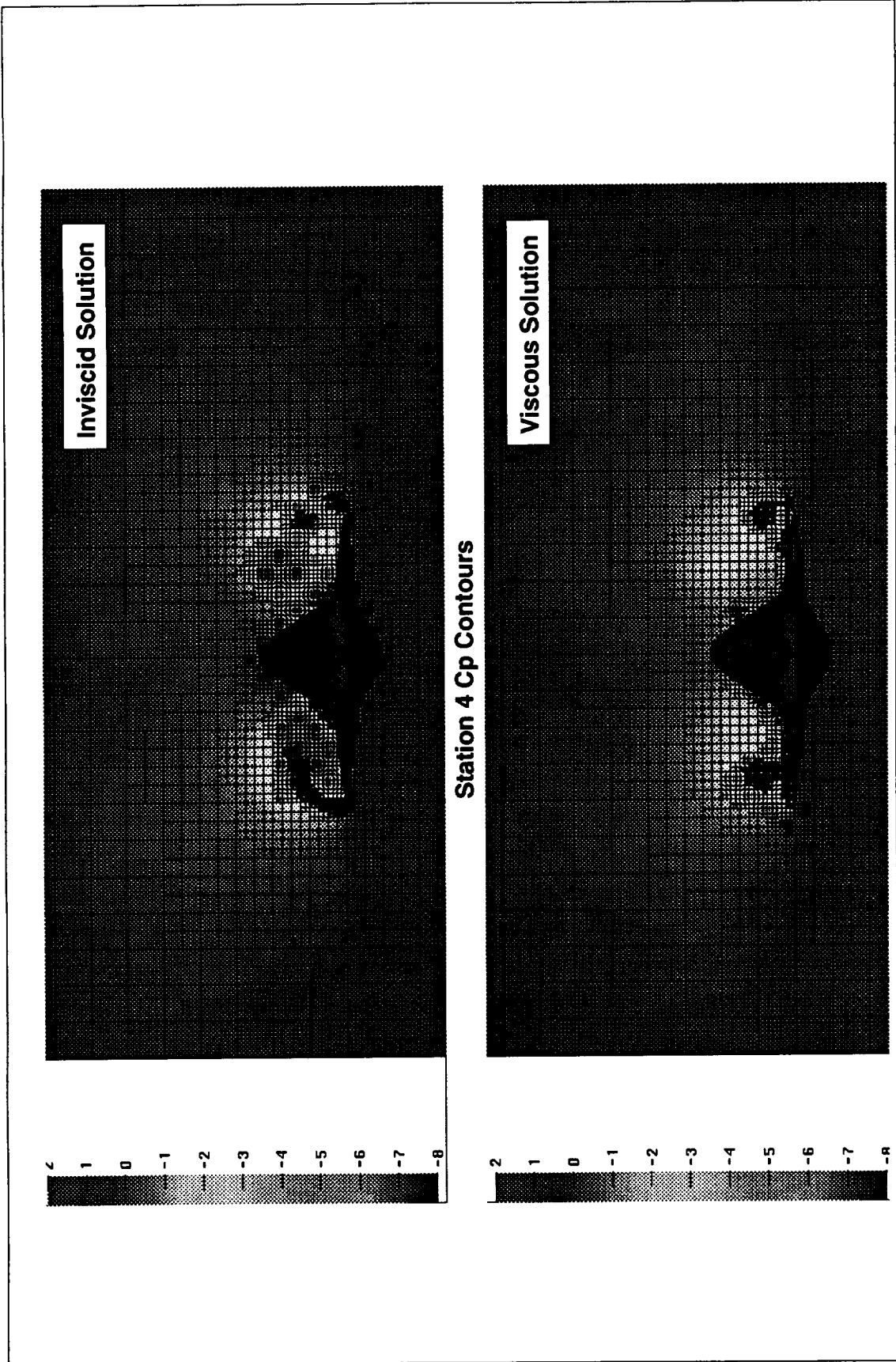Figure 5.7 Comparison of station 3 pressure coefficient contours between inviscid and viscous solutions.

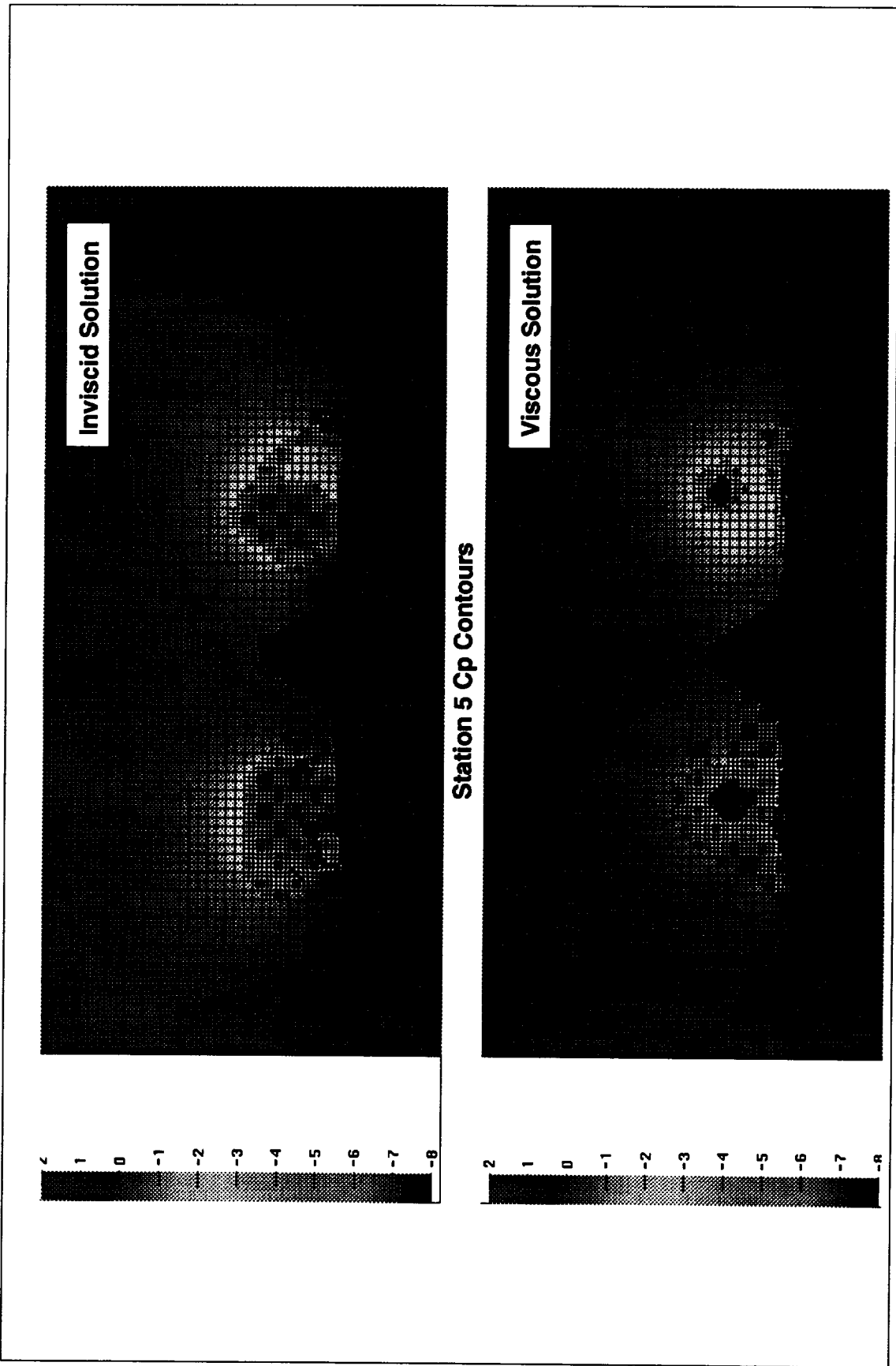**Figure 5.8 Comparison of station 4 pressure coefficient contours between inviscid and viscous solutions.**

Figure 5.9 Comparison of station 5 pressure coefficient contours between inviscid and viscous solutions.
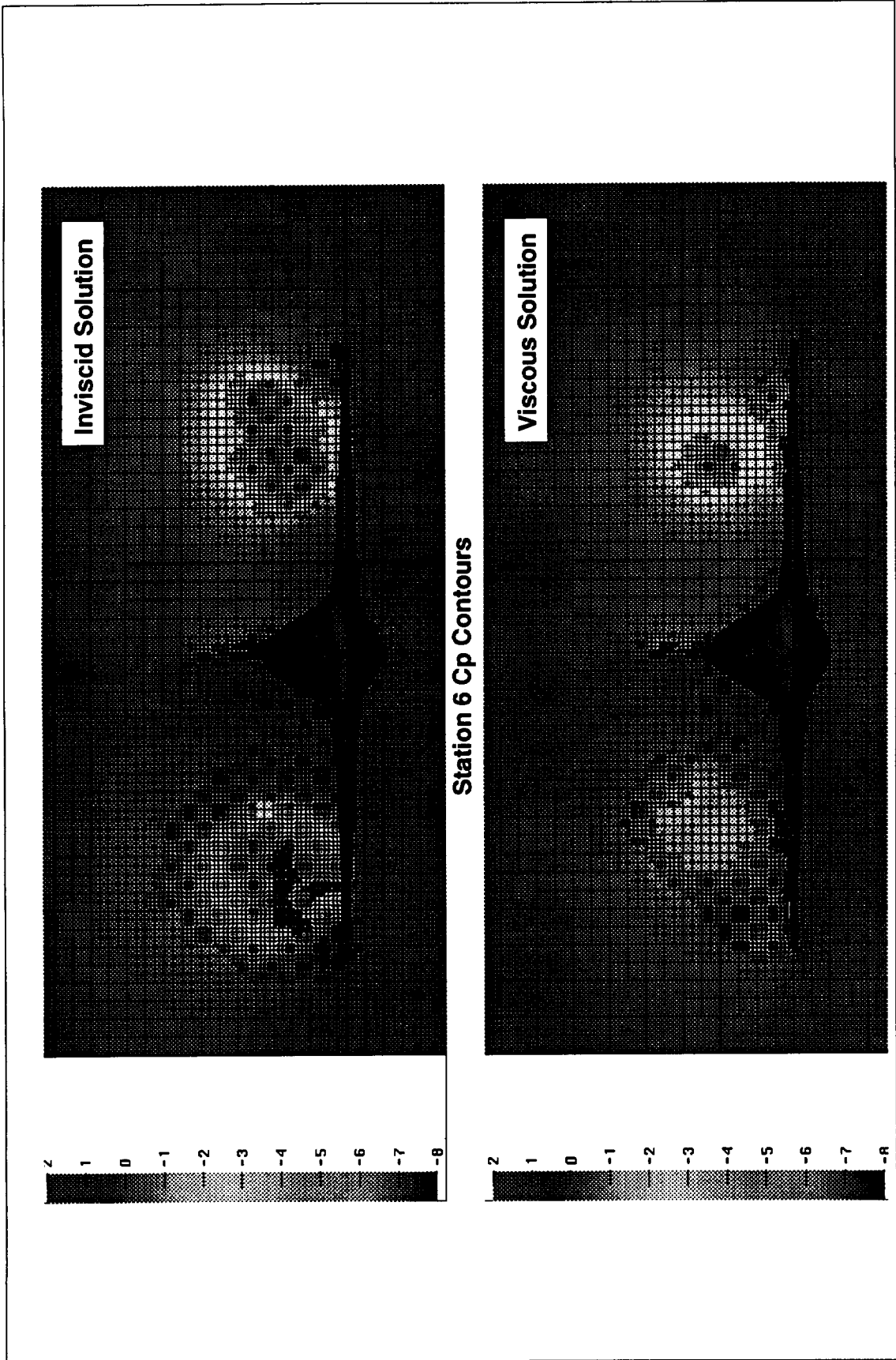
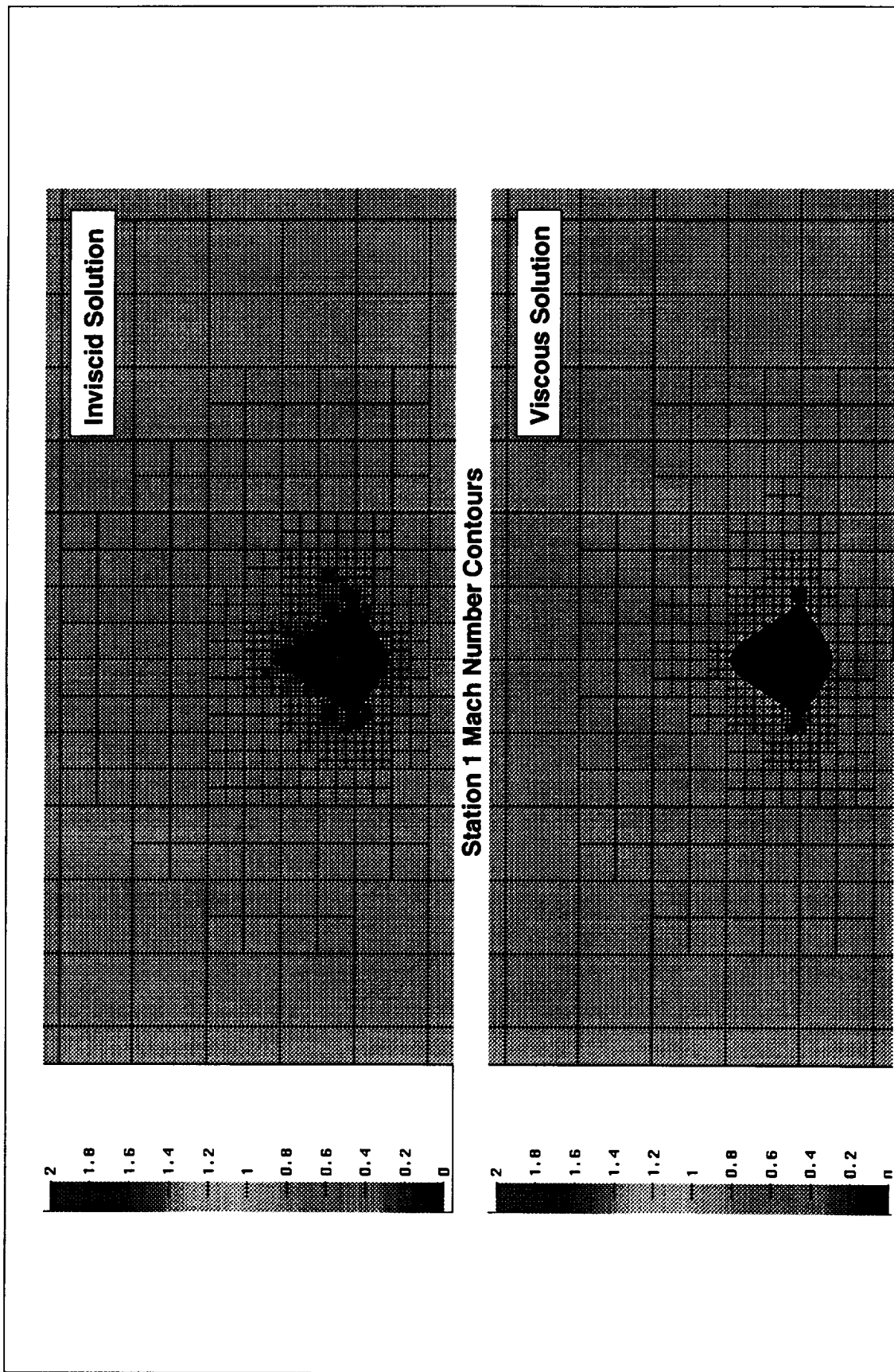**Figure 5.10 Comparison of station 6 pressure coefficient contours between inviscid and viscous solutions.**

Figure 5.11 Comparison of station 1 Mach number contours between inviscid and viscous solutions.
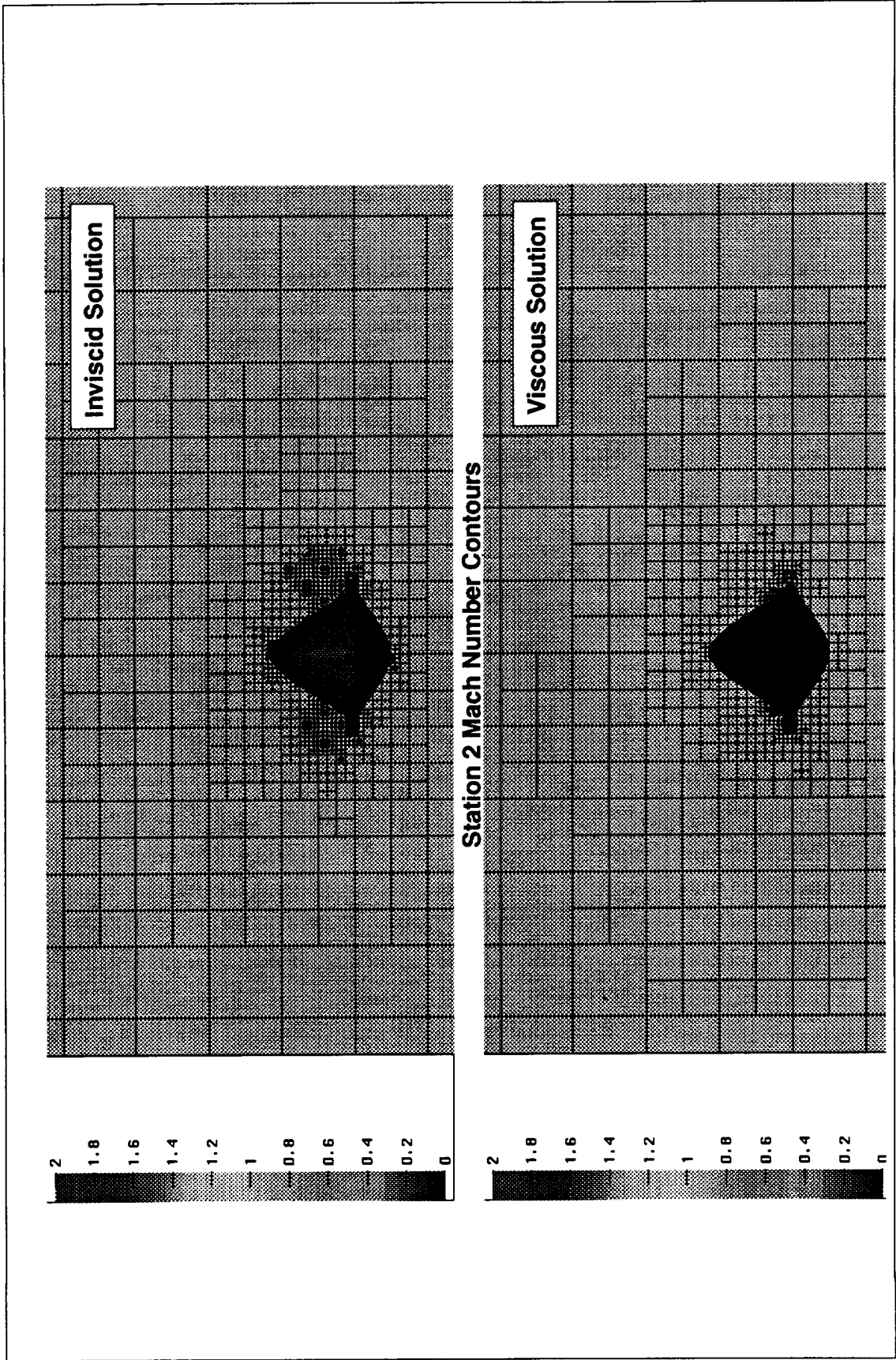
Figure 5.12 Comparison of station 2 Mach number contours between inviscid and viscous solutions.

Inviscid Solution

Viscous Solution

Station 3 Mach Number Contours

Figure 5.13 Comparison of station 3 Mach number contours between inviscid and viscous solutions.

Figure 5.14 Comparison of station 4 Mach number contours between inviscid and viscous solutions.

Figure 5.15 Comparison of station 5 Mach number contours between inviscid and viscous solutions.
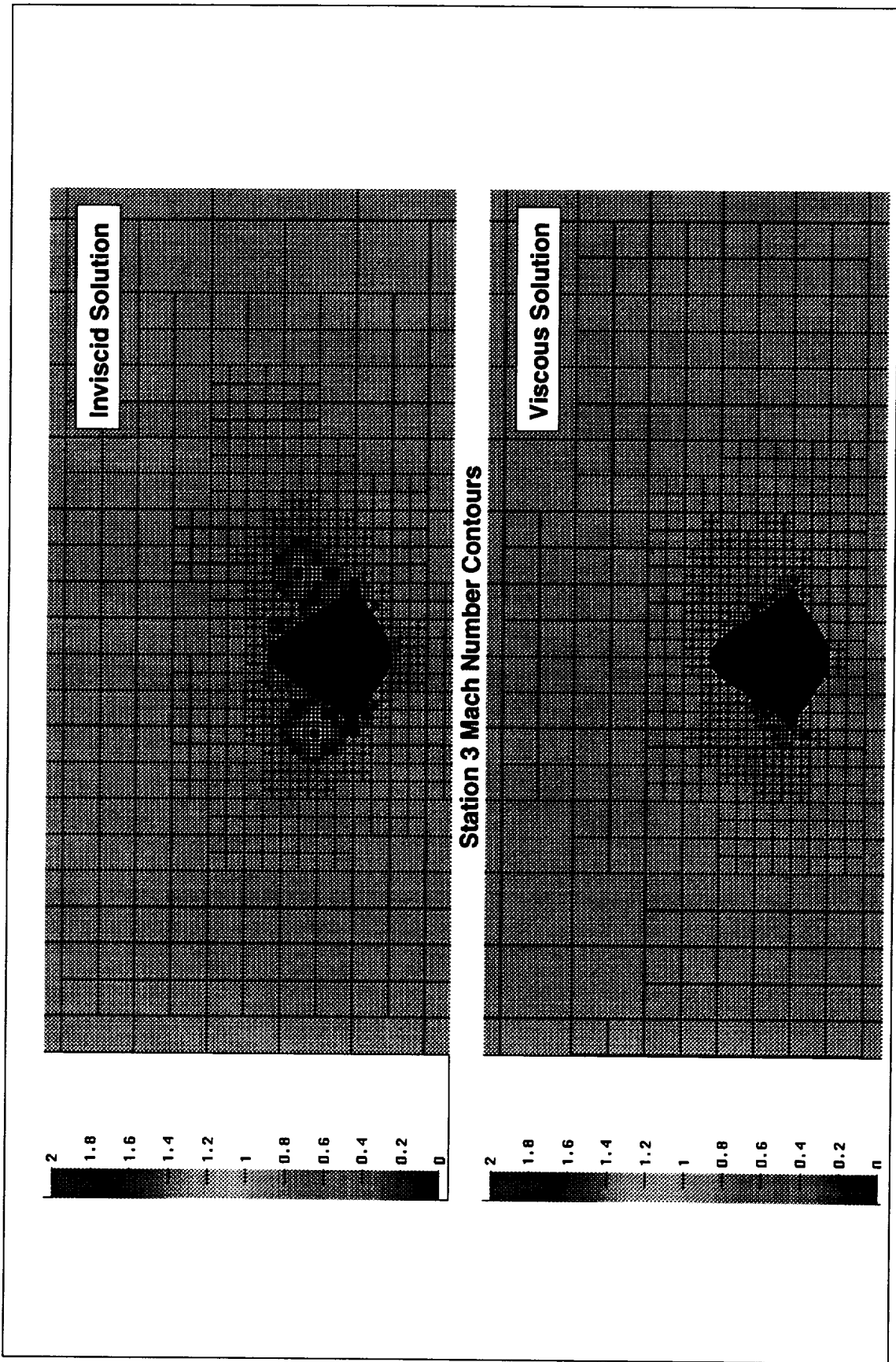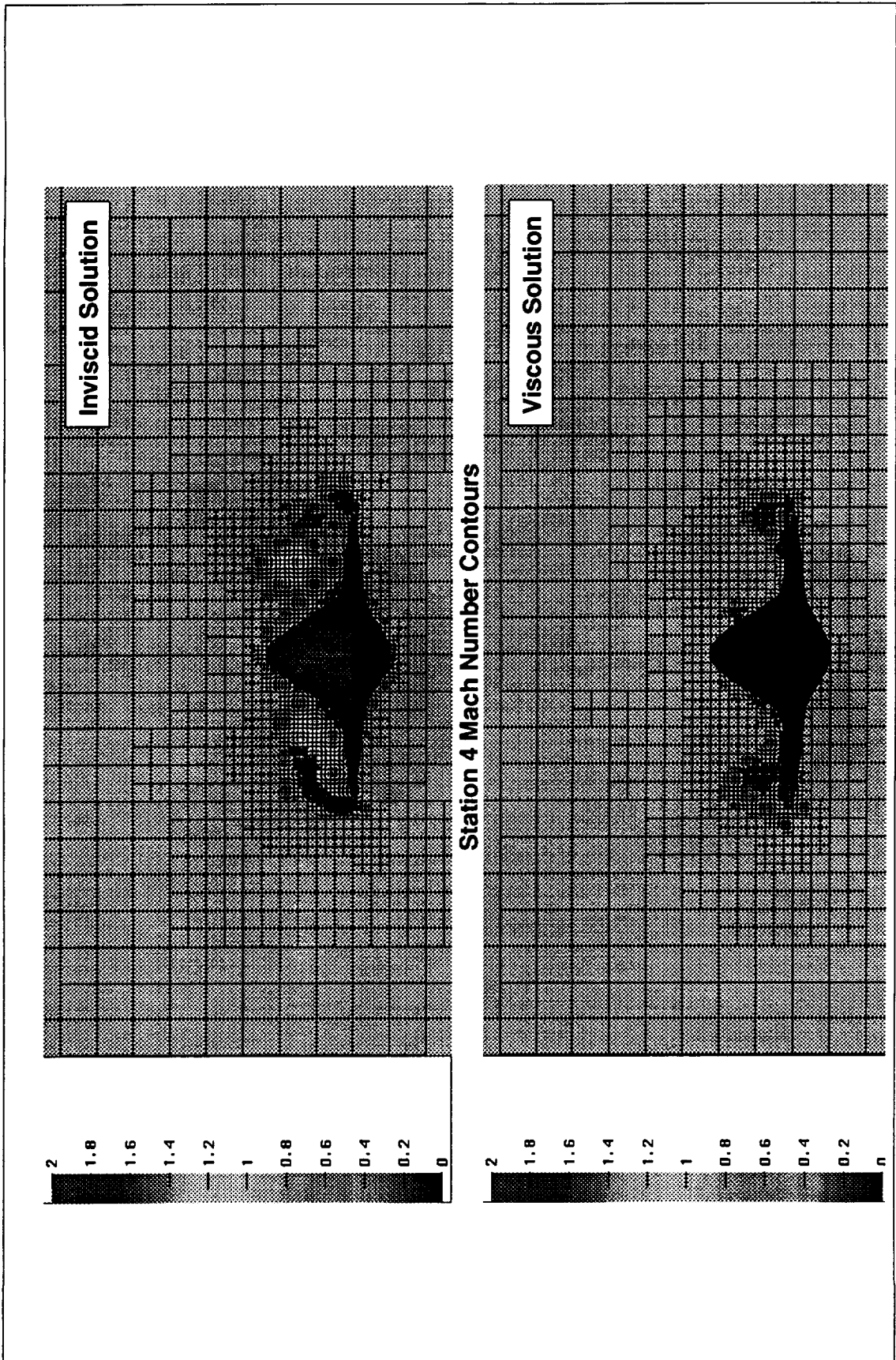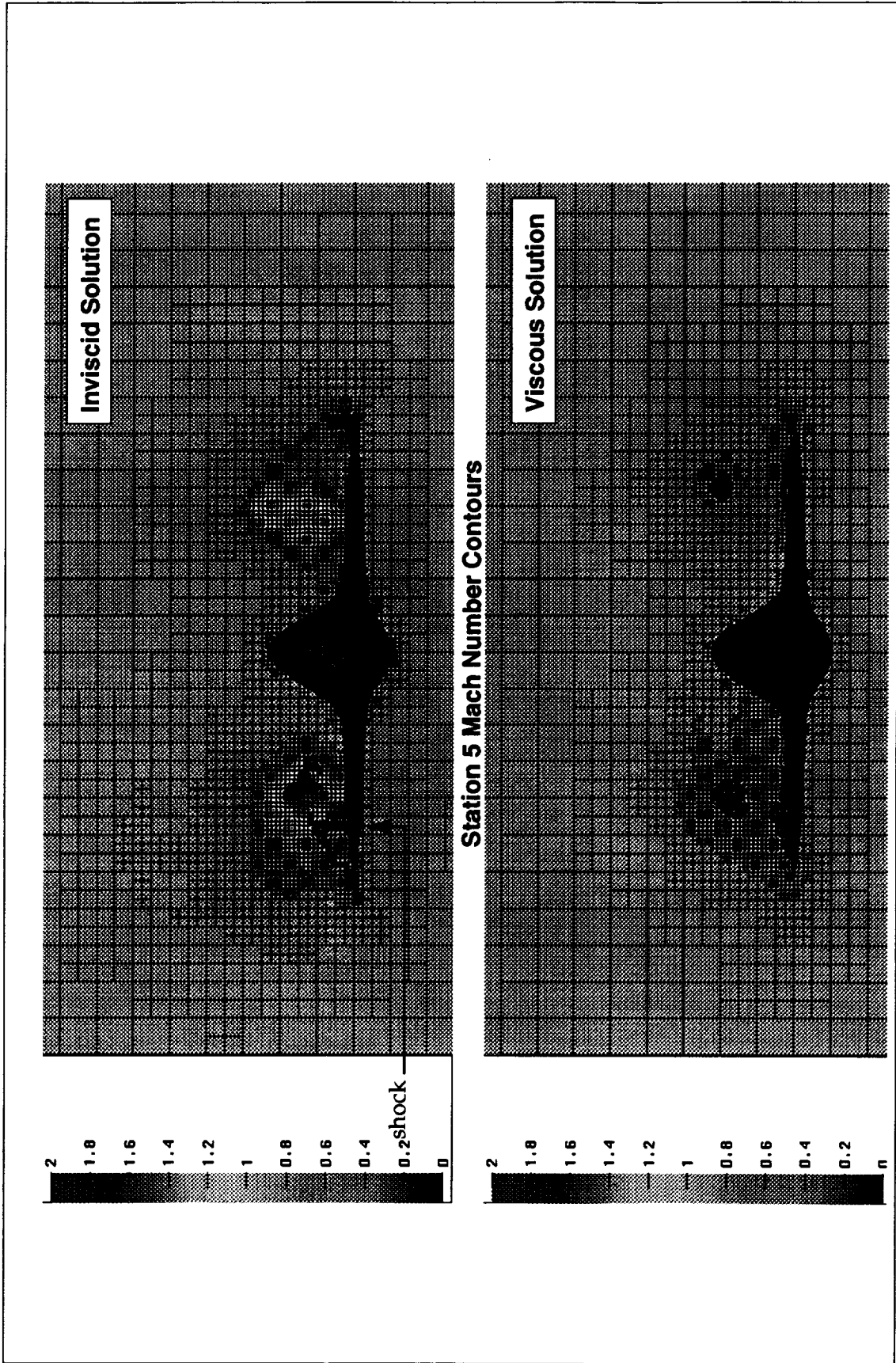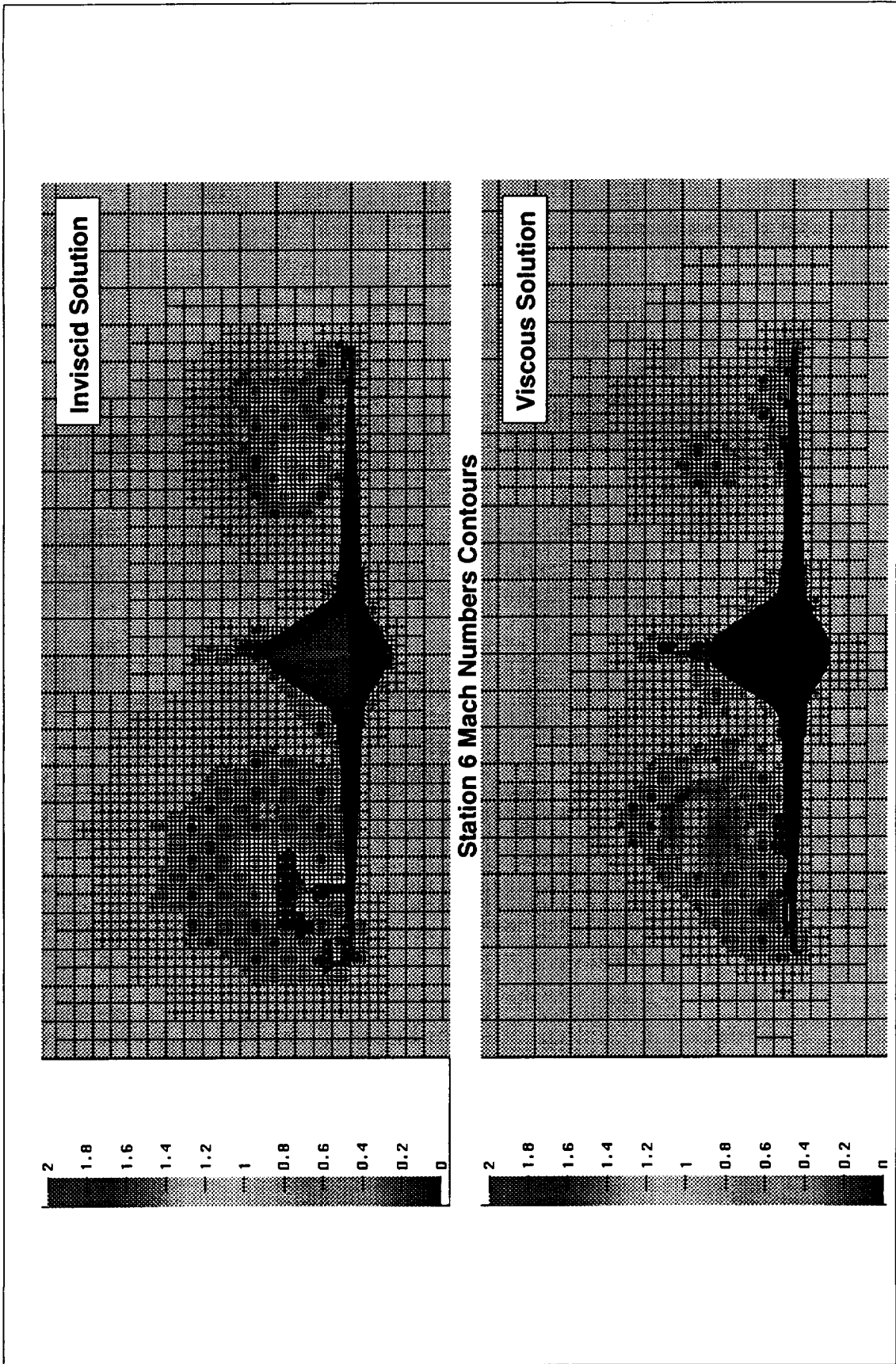
Figure 5.16 Comparison of station 6 Mach number contours between inviscid and viscous solutions.

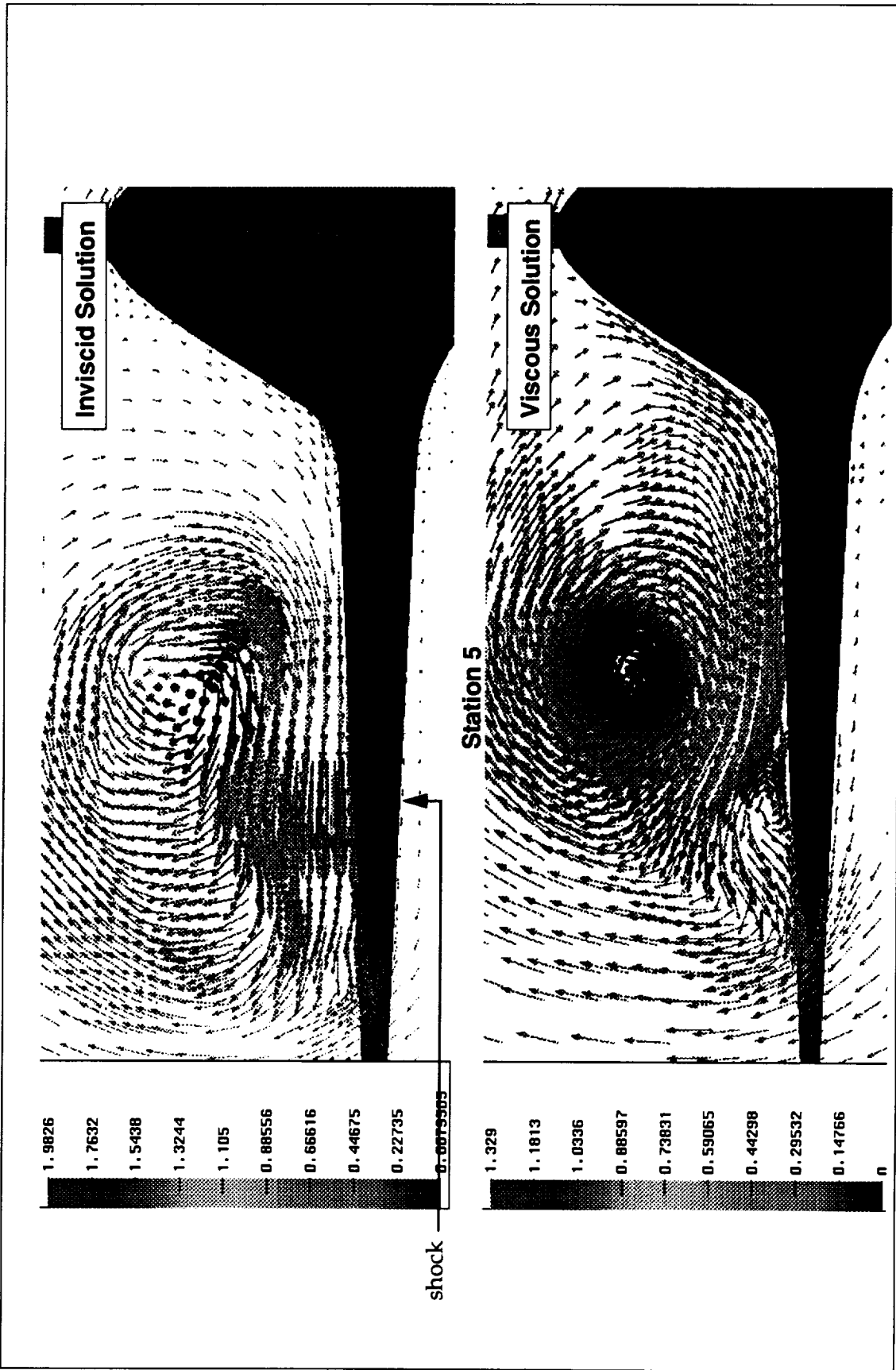Figure 5.17 Comparison of velocity vectors at station 5 for inviscid and viscous solutions.
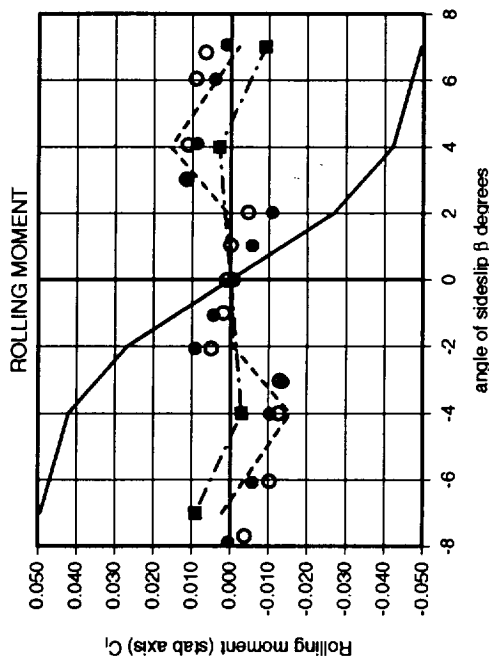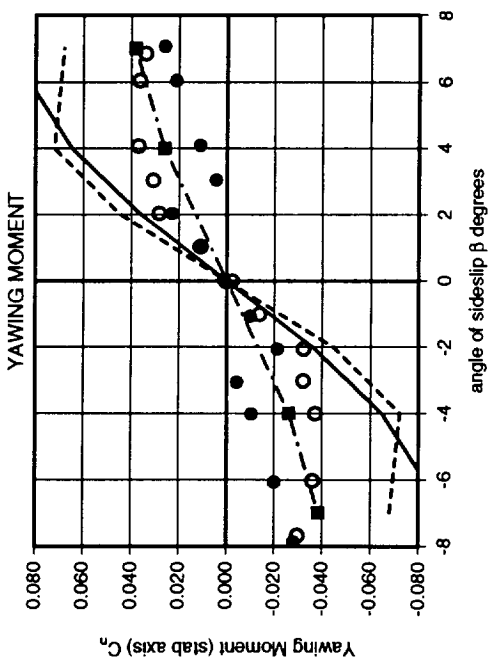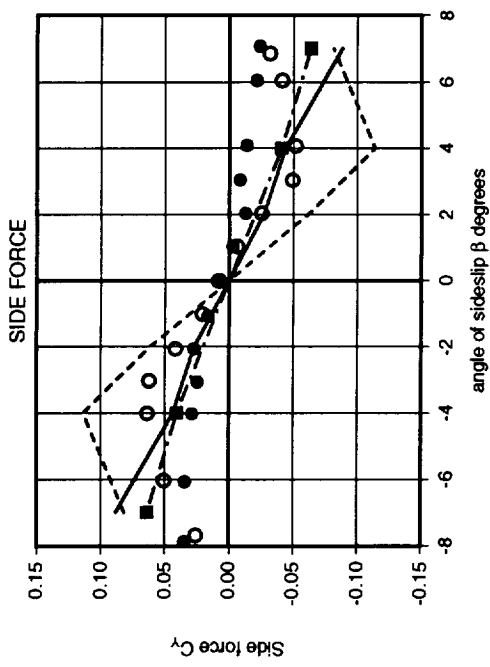
Figure 5.18 Viscous result for lateral-directional forces/moments on centerline tail, stability axes, AOA=25.
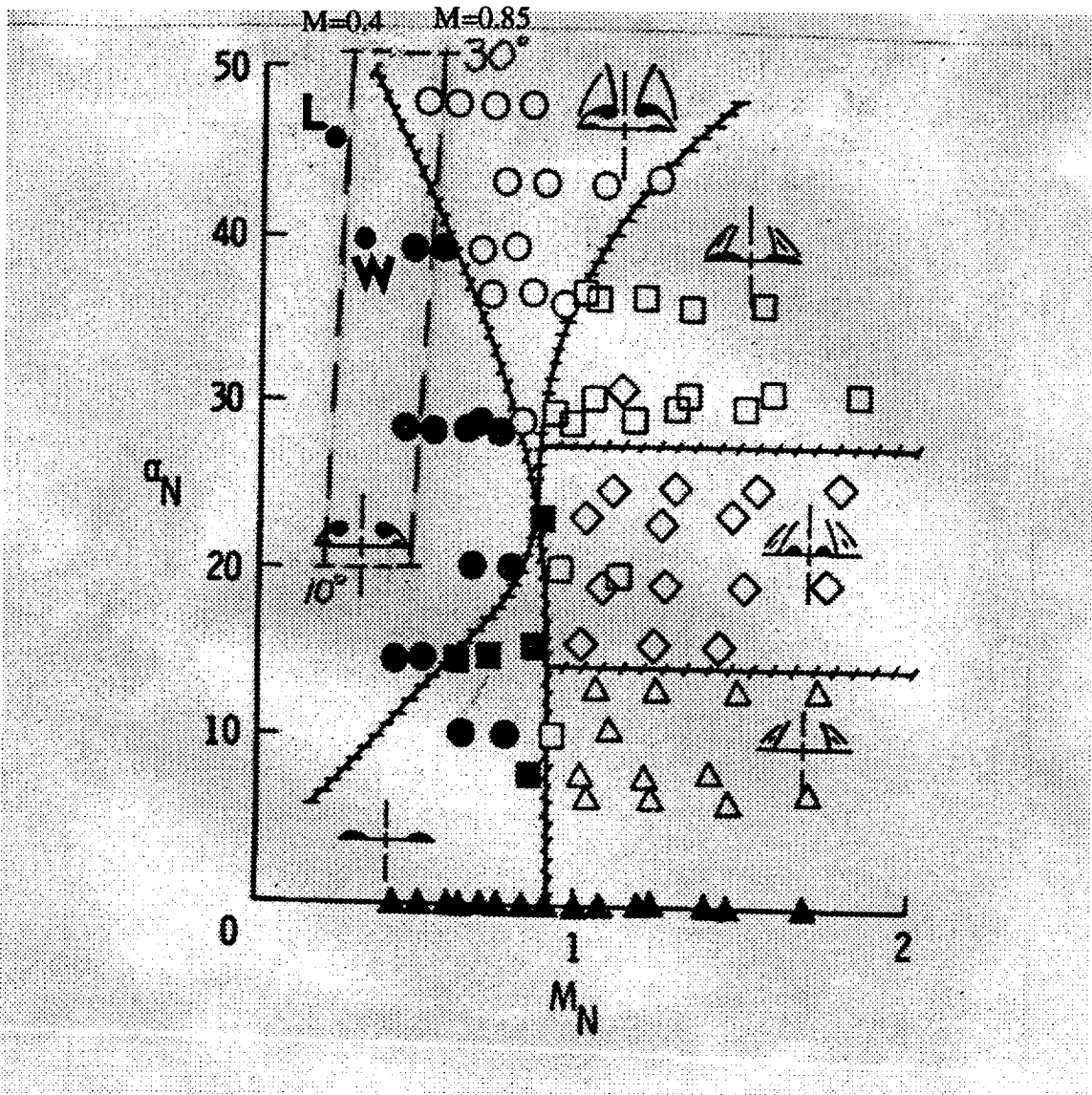
Figure 5.19 Classical vortex character of Miller and Wood.

REPORT DOCUMENTATION PAGE

Public reporting burden for this collection of information is estimated to average 1 hour per response, including the time for reviewing instructions, searching existing data sources, gathering and maintaining the data needed, and completing and reviewing the collection of information. Send comments regarding this burden estimate or any other aspect of this collection of information, including suggestions for reducing this burden, to Washington Headquarters Services, Directorate for Information Operations and Reports, 1215 Jefferson Davis Highway, Suite 1204, Arlington, VA 22202-4302, and to the Office of Management and Budget, Paperwork Reduction Project (0704-0188), Washington, DC 20503.

1. AGENCY USE ONLY(Leave blank)	2. REPORT DATE March 1996	3. REPORT TYPE AND DATES COVERED Contractor Report (2/1/95 to 9/30/95)

4. TITLE AND SUBTITLE

Euler Technology Assessment for Preliminary Aircraft Design -
Compressibility Predictions by Employing the Cartesian
Unstructured Grid SPLITFLOW Code

5. FUNDING NUMBERS

NAS1-19000, Task DA012
WU 505-68-30-03

6. AUTHOR(S)

Dennis B. Finley and Steve L. Karman, Jr.

7. PERFORMING ORGANIZATION NAME(S) AND ADDRESS(ES)

Lockheed Martin Tactical Aircraft Systems
Fort Worth, TX 76101

8. PERFORMING ORGANIZATION REPORT NUMBER

9. SPONSORING/MONITORING AGENCY NAME(S) AND ADDRESS(ES)

National Aeronautics and Space Administration
Langley Research Center
Hampton, VA 23681-0001

10. SPONSORING/MONITORING AGENCY REPORT NUMBER

NASA CR-4710

11. SUPPLEMENTARY NOTES

Technical Monitor: Mr. Farhad Ghaffari
NASA Langley Research Center
Hampton VA 23681-0001

12a. DISTRIBUTION/AVAILABILITY STATEMENT

Unclassified-Unlimited
Subject Category 02

12b. DISTRIBUTION CODE

13. ABSTRACT *(Maximum 200 words)*

This report documents results from the second phase of the Euler Technology Assessment program. The objective of this phase was to evaluate the ability of Euler computational-fluid dynamics codes to predict compressible flow effects over a generic fighter wind tunnel model. This portion of the study was conducted by Lockheed Martin Tactical Aircraft Systems, using an in-house Cartesian-grid code called SPLITFLOW (Ref. 1). The Cartesian grid technique offers several advantages for this study, including ease of volume grid generation and reduced number of cells compared to other grid schemes. SPLITFLOW also includes grid adaption of the volume grid during the solution to resolve high-gradient regions. The SPLITFLOW code predictions of configuration forces and moments are shown to be adequate for preliminary design, including predictions of sideslip effects and the effects of geometry variations at low and high angles-of-attack. The time required to generate the results from initial surface data is on the order of several hours, including grid generation, which is compatible with the needs of the design environment.

14. SUBJECT TERMS

Computational Fluid Dynamics, Euler/inviscid method, Compressibility,
Cartesian/unstructured grid, Sharp-edge flow separation, Vortex flow/burst

15. NUMBER OF PAGES
95

16. PRICE CODE
A05

17. SECURITY CLASSIFICATION OF REPORT Unclassified	18. SECURITY CLASSIFICATION OF THIS PAGE Unclassified	19. SECURITY CLASSIFICATION OF ABSTRACT Unclassified	20. LIMITATION OF ABSTRACT

NSN 7540-01-280-5500